Enhanced Condensation Heat Transfer for Water and Low Surface Tension Fluids

by

Daniel John Preston

SM, Mechanical Engineering (2014)
Massachusetts Institute of Technology

BSME, Mechanical Engineering (2012)
The University of Alabama

Submitted to the Department of Mechanical Engineering in
Partial Fulfillment of the Requirements for the
Degree of Doctor of Philosophy in Mechanical Engineering
at the
Massachusetts Institute of Technology
June 2017

Signature of Author: ……

Department of Mechanical Engineering
May 12, 2017

Certified by: ……

Evelyn N. Wang
Gail E. Kendall Associate Professor of Mechanical Engineering
Thesis Supervisor

Accepted by: ……

Rohan Abeyaratne
Professor of Mechanical Engineering
Chairman, Department Committee on Graduate Theses

Intentionally blank page

Enhanced Condensation Heat Transfer for Water and Low Surface Tension Fluids

by

Daniel John Preston

Submitted to the Department of Mechanical Engineering on May 12th, 2017,
in Partial Fulfillment of the Requirements for the Degree of Doctor of Philosophy

Abstract

Vapor condensation is routinely used as an effective means of transferring heat or separating fluids for applications ranging from personal electronic device thermal management to natural gas processing and electric power generation. Filmwise condensation, where the condensed fluid forms a liquid film, is prevalent in typical industrial-scale systems. Conversely, dropwise condensation, where the condensate forms discrete liquid droplets, results in an improvement in heat transfer performance of up to an order of magnitude compared to filmwise condensation. We explored rare earth oxides (REOs) as a potential coating to induce dropwise condensation of water; specifically, we experimentally demonstrated that the mechanism for REO hydrophobicity results from adsorption of contaminants from the atmosphere. We also used graphene, which is hydrophobic in nature, as a coating to achieve robust dropwise water condensation. With a graphene coating, we demonstrated a 4*x* improvement in water condensation heat transfer compared to filmwise condensation with robustness superior to state-of-the-art hydrophobic monolayer coatings. Meanwhile, low surface tension condensates pose a unique challenge since they often form a film, even on hydrophobic coatings. Lubricant infused surfaces (LIS) represent a potential solution, where a lubricant immiscible with the low surface tension condensate is infused into a rough structure on the condenser surface to repel the condensate. We developed a detailed surface-energy-based model to provide design guidelines for any arbitrary LIS system. We then characterized heat transfer coefficients during condensation of low surface tension fluids on LIS in a controlled environmental chamber for the first time, where a 5*x* improvement was demonstrated compared to filmwise condensation. The improved condensation heat transfer coefficients realized by LIS for low surface tension fluids and by REOs and graphene for water present opportunities for significant energy savings in device thermal management, heating and cooling, and power generation.

Thesis Committee:

Professor Evelyn N. Wang (Thesis Advisor/Chair), Department of Mechanical Engineering
Professor Borivoje Mikic, Department of Mechanical Engineering
Professor Gareth H. McKinley, Department of Mechanical Engineering

Intentionally blank page

Acknowledgements

I am thankful for funding from the Office of Naval Research (ONR) with Dr. Mark Spector as program manager, the Abu Dhabi National Oil Company (ADNOC) with Dr. Abdullah Al Mahri as program manager, the Center for Nanoscale Systems (CNS) at Harvard University, which is a member of the National Nanotechnology Infrastructure Network (NNIN), and the National Science Foundation for support through the Graduate Research Fellowship.

Evelyn Wang is an excellent advisor and, beyond that, is genuinely a good person – thank you, Evelyn.

I am grateful to have had the chance to interact with many stimulating colleagues and make great friends both within and outside of MIT – even as distance and careers pull us apart, I hope we remain close.

The undergraduate students I have worked with have all been fantastic – I likely learned more from them than vice versa, and I wish them all the best even as some of them have already found success.

Thank you, Ari, for your support.

I dedicate this thesis to my family.

Intentionally blank page

Table of Contents

Intentionally blank page

List of Figures

Intentionally blank page

Chapter 1

1. Introduction

1.1 MOTIVATION

Vapor condensation is a familiar phenomenon which routinely occurs in nature[1-4]. An everyday example of condensation is the droplets of water which form on the container of a cold beverage left out on a warm, humid day. Condensation is also an essential consideration in industry for power generation[5], thermal management[6,7], water desalination[8,9], and environmental control[10]. For example, the steam cycle is responsible for over 90% of electrical power generation worldwide, and condensation heat transfer performance directly influences the thermal efficiency of the steam cycle[11]. If the heat transfer performance of the condenser shown schematically in the steam cycle in Figure 1 were improved, the bottoming cycle temperature, T_{LOW}, could be lowered while keeping T_{HIGH} the same. The efficiency of the cycle is related to the ratio of the high to the low temperature, where a higher temperature ratio T_{HIGH}/T_{LOW} is expected to result in higher cycle efficiency. Therefore, lowering T_{LOW} increases T_{HIGH}/T_{LOW} and translates to an efficiency improvement. In addition to improved cycle efficiency, a higher condensation heat transfer rate could mean that a smaller condenser is required, potentially decreasing the capital cost associated with construction of power plants that operate with steam cycles.

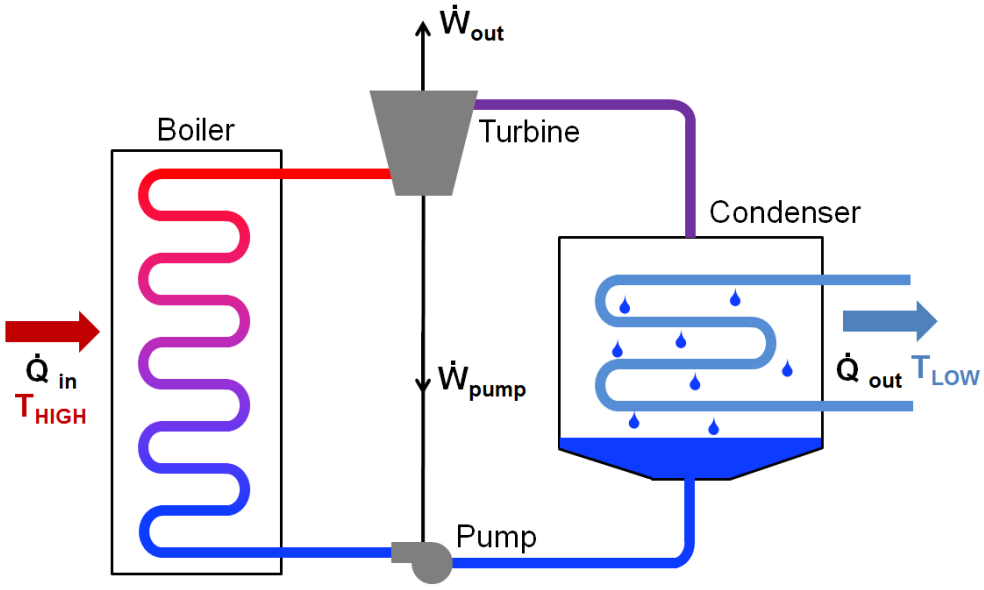

Figure 1. Schematic representation of an ideal steam cycle. Starting from the liquid phase inside of the condenser, the fluid is pumped to high pressure, converted to vapor by the addition of heat at T_{HIGH} in the boiler, expanded through the turbine back to the condenser pressure while producing work, and then condensed from vapor back to the starting liquid phase by removal of heat at T_{LOW}.

Heating, ventilation, and air conditioning (HVAC) systems, which account for ≈20% of the total energy consumption in developed countries[12], also must be designed with condensation heat transfer performance in mind to limit the buildup of condensate and improve efficiency. Yet another area where condensation is important is in the transmittance of light into greenhouses, where condensate formation on windows can result in losses of up to 40% during the winter[13].

1.2 BACKGROUND

For these applications, heterogeneous condensation occurs on condenser walls as opposed to directly in the vapor phase because of reduced energy barriers for heterogeneous nucleation relative to homogeneous nucleation[14]. In typical industrial systems, the condensed vapor forms a thin liquid film on the condenser surface due to the high surface energy associated with the majority of industrial heat exchanger materials (*i.e.*, clean metals and metal oxides). This mode, known as filmwise condensation, (Figure 2), is not desired due to the large thermal resistance to heat transfer[15]. However, on low surface energy materials, the condensed vapor forms discrete liquid droplets. During this dropwise condensation, droplets roll off at sizes approaching the capillary length (≈2 mm for water) and clear the surface for re-nucleation as shown in Figure 2[16].

Dropwise condensation can be achieved if the condensing surface is functionalized with a hydrophobic coating, for example a long-chain fatty acid, wax, or polymer coating[17-20]. Compared to filmwise condensation, dropwise condensation allows 5–7*x* higher heat transfer performance, as illustrated in Figure 3. The heat flux, *q*”, is the most commonly used metric for quantifying the amount of latent heat

Figure 2. Filmwise condensation of water on a bare copper condenser tube (left) and dropwise condensation on a copper tube functionalized with a monolayer hydrophobic coating (right).

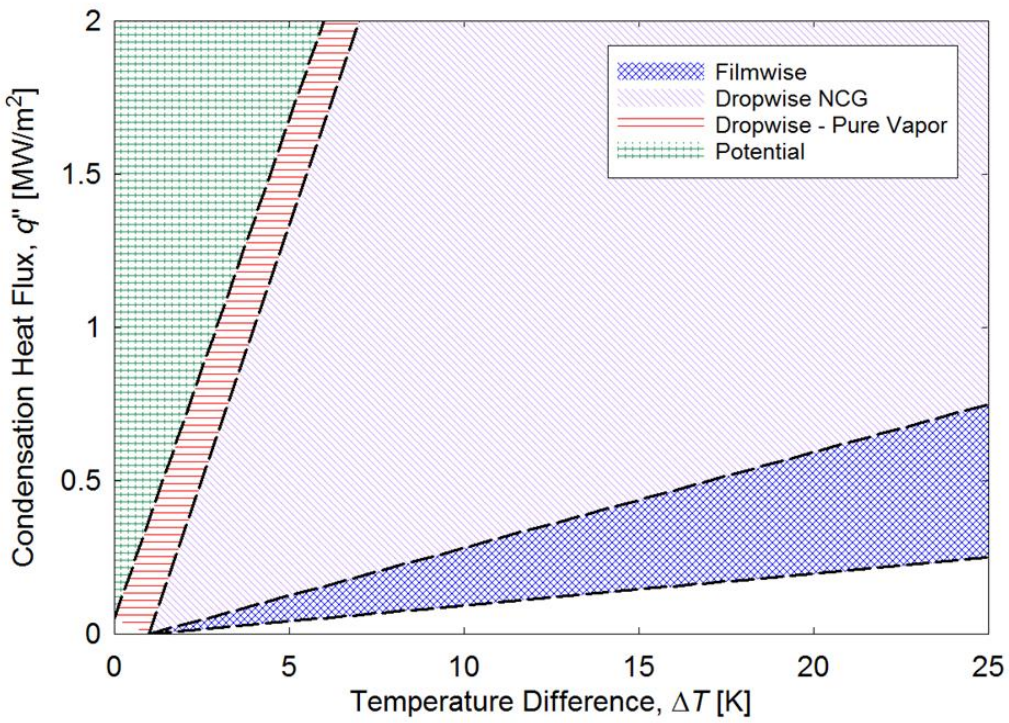

Figure 3. Condensation mode regime map shown with heat flux as a function of temperature difference between the condenser surface and surrounding vapor. The green area indicates potential improvement in heat transfer coefficient over state-of-the-art dropwise condensation.

of phase change removed by the surface during condensation at a given driving potential (temperature difference), $\Delta T = T_{sat}(P_v) - T_{wall}$, where $T_{sat}(P_v)$ is the saturation temperature of the surrounding vapor and T_{wall} is the condenser wall surface temperature. This ΔT is often referred to as the subcooling.

Achieving dropwise condensation on common industrial materials has been a topic of significant interest for the past eight decades[21,22] with an emphasis on creating non-wetting surfaces *via* application of promoter coatings for easy droplet removal. While robust coatings continue to pose a challenge and require further development,[21] recent advancements in nanofabrication have allowed for further tailoring of surface wetting properties and condensation behavior to enhance heat transfer performance above that of dropwise condensation on a flat surface. Three important properties that affect the condensation heat transfer coefficient, $h_c = q''/\Delta T$, are nucleation density, advancing contact angle, and departure radius.[23,24] Heat transfer increases with nucleation density due to the increasing number of small droplets that have low conduction thermal resistance due to their size. Conversely, high apparent contact angle can lead to an increase in conduction resistance through the droplet due to the reduced size of the droplet base,[23,25]

which hinders the overall heat transfer performance. Finally, larger droplets have increased thermal resistance and thus larger droplet departure size results in a lower overall condensation heat transfer coefficient.

1.3 OBTAINING HYDROPHOBICITY

Since most industrial metals, such as aluminum, copper, titanium, and stainless steel (and their corresponding oxides) have high surface energy, surface functionalization *via* a coating that can reduce surface energy is required on these materials to obtain dropwise condensation. This is a particularly active area of research, as no solution has yet been proposed which satisfactorily addresses durability, cost, and performance concerns. Several approaches to obtaining suitably low surface energies are presented here with their advantages and disadvantages highlighted.

Self-assembled monolayers (SAMs) result from spontaneous physi- or chemisorption of a thin molecular film (~1 nm) comprised of individual molecules on the condensing surface. These molecules have hydrophobic tails pointing away from the surface that interact with the condensate and ligand heads that bind to the surface. This functionalization method does not introduce a significant thermal resistance; however, durability is a primary concern. Two common types of SAMs are sulfur-based ligand thiols and silicon-based ligand silanes. Thiols have been found to oxidize over short time scales upon exposure to ambient conditions or UV radiation and reduce to disulfides and sulfonates which can wash away from the surface with polar solvents such as water.[26] Thiols are also less thermally stable than silanes.[27] Silanes show better stability due to covalent bonding with the surface.[28] Furthermore, self-healing strategies have recently been demonstrated based on fluorinated silane chemistries that could increase the longevity of these coatings.[29,30] However, durability is still currently a major concern with silanes.[31]

Polymer coatings such as polytetrafluoroethylene (PTFE), parylene, and silicones have been used as a functional coating to promote dropwise condensation.[18,32-34] However, the required coating thickness to realize satisfactory durability results in an added thermal resistance which offsets the heat transfer improvement due to DWC.[18] This thickness requirement may be reduced with new binder materials to form a stronger bond between the polymer and substrate. In addition, initiated CVD of fluoropolymer thin films is another potential functionalization method which offers high coating conformality and potential robustness.[31,35]

Ion implantation promotes dropwise condensation through carbon, nitrogen, and oxygen ion implantation in copper, aluminum, titanium, and steel surfaces.[36-38] Sustained dropwise condensation was achieved on

these surfaces over periods of multiple months.[39] However, this method is not commonly used because it is relatively expensive compared to SAMs and polymer coatings.

Noble metals applied as a thin functional coating are a robust approach to achieve dropwise condensation, with one paper demonstrating continuous DWC on gold for over five years.[40]. Initially, gold was thought to be intrinsically hydrophobic.[41] However, subsequent experimental results showed that the contact angle on a clean gold surface with hydrocarbons desorbed and oxide removed by heating in a hydrogen gas stream with < 1ppm hydrocarbons was 0°.[42]. This claim was initially disputed,[43] but subsequent studies demonstrated that gold, while intrinsically hydrophilic, rapidly adsorbs hydrocarbons from air resulting in increased contact angle and dropwise condensation.[44-46]

1.4 THESIS OBJECTIVES AND OUTLINE

This thesis explores methods to improve the condensation heat transfer coefficient by promoting dropwise condensation of water and low surface tension fluids in a robust manner.

In Chapter 1, the motivation for studying and improving condensation heat transfer was discussed. Previous contributions to the field and various types of hydrophobic coatings were explored.

In Chapter 2, rare earth oxides (REOs) are explored as a potential coating to induce dropwise condensation of water; specifically, the mechanism for REO hydrophobicity is experimentally demonstrated to result from stable adsorption of contaminants from the atmosphere.

In Chapter 3, graphene is used to achieve robust dropwise water condensation. A 400% improvement in water condensation heat transfer compared to filmwise condensation with robustness superior to state-of-the-art monolayer hydrophobic coatings is demonstrated with graphene.

In Chapter 4, the heat transfer coefficient for low surface tension fluids condensing on lubricant infused surfaces, where a lubricant immiscible with the low surface tension condensate is infused into a rough structure on the condenser surface to repel the condensate, is experimentally measured

In Chapter 5, a detailed surface-energy-based model which provides design guidelines for any arbitrary lubricant infused surface is described and insights from the model are presented.

In Chapter 6, perspectives on the work are presented and future directions are proposed.

Chapter 2

2. Effect of Hydrocarbon Adsorption on the Wettability of Rare Earth Oxide Ceramics

State-of-the-art techniques to promote dropwise condensation rely on functional hydrophobic coatings, which are often not robust and therefore undesirable for industrial implementation. Natural surface contamination due to hydrocarbon adsorption, particularly on noble metals, has been explored as an alternative approach to realize stable dropwise condensing surfaces. While noble metals are prohibitively expensive, the recent discovery of robust rare earth oxide (REO) hydrophobicity has generated interest for dropwise condensation applications due to material costs approaching 1% of gold; however, the underlying mechanism of REO hydrophobicity remains under debate. In this work, we show through careful experiments and modeling that REO hydrophobicity occurs due to the same hydrocarbon adsorption mechanism seen previously on noble metals. To investigate adsorption dynamics, we studied holmia and ceria REOs, along with control samples of gold and silica, *via* X-Ray photoelectron spectroscopy (XPS) and dynamic time-resolved contact angle measurements. The contact angle and surface carbon percent started at ≈ 0 on in-situ argon-plasma-cleaned samples and increased asymptotically over time after exposure to laboratory air, with the rare earth oxides displaying hydrophobic (> 90 degrees) advancing contact angle behavior at long times (> 4 days). The results indicate that REOs are in fact hydrophilic when clean, and become hydrophobic due to hydrocarbon adsorption. Furthermore, this study provides insight into how REOs can be used to promote stable dropwise condensation, which is important for the development of enhanced phase change surfaces.

2.1 INTRODUCTION

Condensation is observed frequently in our environment and routinely used in industry as an effective means of transferring heat. Water condensation on typical industrial condenser metal surfaces and their respective high-surface-energy oxides, *e.g.*, CuO, Al_2O_3, and Fe_2O_3, results in the formation of a film of condensate that spreads over the condenser surface, termed filmwise condensation.[15] This filmwise mode of condensation imposes a thermal resistance across the film, which limits heat transfer. Conversely, water condensation on a low-surface-energy material, *e.g.*, PTFE, parylene, and PFDA, results in the formation of discrete condensate droplets that, when under gravity-driven convection, shed as their size approaches the capillary length (≈2 mm for water), termed dropwise condensation.[16] The shedding of

droplets refreshes the surface for renucleation and offers an improvement in heat transfer performance of 5 – 7x compared to filmwise condensation.[21]

State-of-the-art techniques to promote dropwise condensation rely on the application of low-surface-energy hydrophobic coatings to the condenser surface.[21,47] Coatings as thin as a monolayer (≈1 nm) of long-chain fluorocarbon molecules or fatty acids can be applied to induce hydrophobicity, but these are often not robust over extended periods of time and therefore unsuitable in industrial applications.[48] Thicker polymer coatings, *e.g.*, ≈ 20 μm coating of PTFE, have shown the potential to maintain robust hydrophobicity, but have a characteristically large thermal resistance that can negate the advantage gained by achieving dropwise condensation.[21] More recently, plasma enhanced chemical vapor deposition (PECVD) and initiated chemical vapor deposition (iCVD) have been used to grow ultra-thin (< 40 nm) conformal coatings of polymer on surfaces with success in achieving dropwise condensation.[48,49] However, the longevity of these ultra-thin coatings remains a question due to the lack of extended or accelerated testing to assess mechanical durability and long-term stability.

An alternative to the direct application of low-surface-energy coatings relies on surface contamination due to energetically favorable hydrocarbon adsorption, particularly on high thermal conductivity noble metals (*i.e.*, gold and silver).[50] These metals are wetting when clean, but reduce their surface energy by adsorbing hydrocarbons from air, enabling dropwise condensation when used as condenser surfaces. The robustness of this approach is well-documented, with one paper demonstrating continuous dropwise condensation on gold for over five years in a closed system.[40] Unfortunately, the high price of noble metals prohibits this approach in practice.

Researchers have recently demonstrated rare earth oxides (REOs) as potential candidates for condenser surface coatings due the their apparent intrinsic hydrophobicity[51] and costs approaching 1% of gold.[52] However, reported contact angles on REOs are inconsistent. Advancing contact angles ranging from 17 – 134° have been observed, with a study reporting 94 - 134° on rough electroplated ceria coatings[53]. Meanwhile another study reports 120° on a rough ceria membrane, but 17° on ceria after oxidation by heating cerium foil in air and 31° on a rough ceria membrane which has been sonicated in ethanol to destroy the nanostructure.[54]

Furthermore, the underlying mechanism of REO hydrophobicity does not seem to be well-understood. The initially reported intrinsic hydrophobicity of REOs asks for a comparison with the debate in scientific literature regarding the intrinsic wettability of gold in the 1960s.[51] Erb and Fowkes asserted that gold was

intrinsically hydrophobic in 1964,[40,41] which Zisman contradicted the following year with experiments demonstrating that the contact angle on a gold surface with hydrocarbons desorbed and oxide removed (by heating in a hydrogen gas stream with < 1ppm hydrocarbons) was ≈ 0°.[42] Though Erb initially disputed the claim,[55] subsequent studies determined that gold is intrinsically hydrophilic but rapidly adsorbs hydrocarbons from the ambient environment, resulting in an increased contact angle.[44-46,56-58] The idea of achieving hydrophobicity *via* hydrocarbon adsorption has been extended for a wide class of materials, including ceramic metal oxides[59,60] as well as pristine monolayer graphene.[61] However, in the case of REOs such as ceria, while previous work has shown that methane adsorbs to the surface[62] and hydrocarbon adsorption increases on roughened surfaces with more available surface area,[63] adsorption of hydrocarbons besides methane and the subsequent effect on contact angle have not been investigated. In this work, we show through experiments and modeling that REO hydrophobicity occurs due to a similar hydrocarbon adsorption mechanism observed previously on noble metals. To investigate adsorption dynamics under ambient conditions, we studied two REOs with different oxidation states, holmia (Ho_2O_3) and ceria (CeO_2), along with control samples of silica on a silicon wafer substrate and gold; both chosen because literature values on the effect of hydrocarbon adsorption were readily available.

2.2 SAMPLE PREPARATION

REO samples were fabricated by pressing and sintering powders (Sigma-Aldrich: holmia, 99.9% pure, 100 nm; ceria, 99.9% pure, 5 μm) in accordance with the procedure described in the study which first reported REO hydrophobicity.[51] First, the powders were dry-pressed into ≈ 2 mm thick chips at 270 MPa and then at 350 MPa in a 13-mm-diameter steel pellet die (REFLEX evacuable pellet die). The chips were then sintered for 4 hr at 1600 °C and 1560 °C for holmia and ceria, respectively, in a box furnace (Blue-M, Thermo Scientific). Field emission scanning electron microscopy images of the grains formed during sintering are shown in Figure 4 along with atomic force microscopy (AFM) scans of the surface. The surface roughness, defined as the ratio of actual surface area to projected surface area, was determined from AFM to be less than 1.05 for both samples, which indicates that surface roughness did not significantly impact wettability.

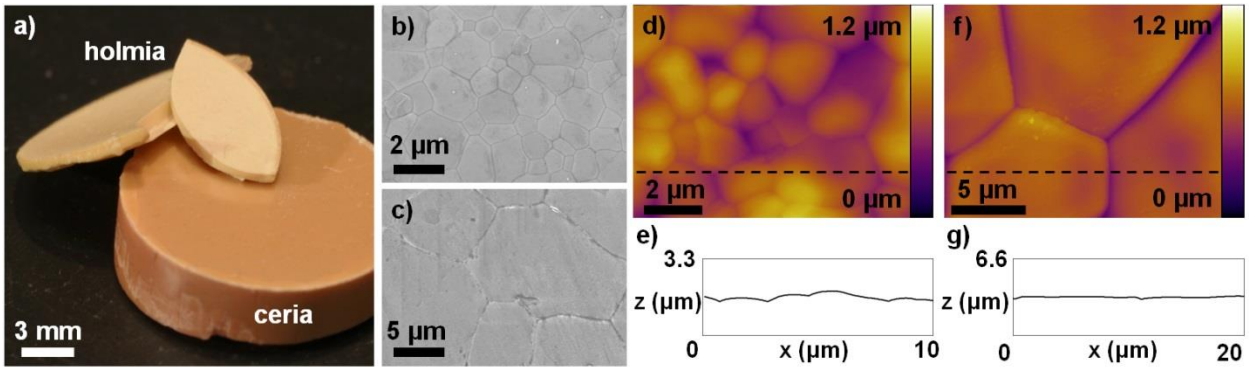

Figure 4. (a) Holmia (Ho_2O_3) and ceria (CeO_2) samples after dry-pressing and sintering. The holmia fracture shows the brittle nature of the REOs. Field emission scanning electron microscopy images are shown for the (b) holmia and (c) ceria surfaces. The average grain sizes are ≈1 µm and ≈10 µm, respectively. AFM scans of the surfaces are presented with height profiles along the dashed lines on these scans shown below for (d and e) holmia and (f and g) ceria. The ratio of actual surface area to projected surface area was less than 1.05 for both REO samples.

To ensure a pristine surface, the samples were cleaned with argon plasma (Harrick PDC-001) until no contaminants were present as evidenced by X-ray photoelectron spectroscopy (XPS) (Thermo Scientific K-Alpha), and the samples were further bombarded by argon ions inside of the XPS chamber before the first (pristine) measurement of surface composition. Argon plasma was used because it is inert and removes contamination by physical bombardment as compared to oxygen-containing plasma, which reacts chemically with the surface.[64] Furthermore, argon plasma has been shown to remove adsorbed hydrocarbons and does not significantly increase surface roughness.[65-67] The pristine surfaces after argon ion bombardment showed that the surfaces exhibited the expected stoichiometric ratios for their respective oxidation states, with gold in its elemental state (Table 1).

2.3 RESULTS AND DISCUSSION

After cleaning, the samples were exposed to laboratory air (MIT Rohsenow-Kendall Heat Transfer Laboratory, ambient temperature = 25 ± 2 °C, relative humidity = 35 ± 10%) and the advancing and receding contact angles and XPS spectra were measured at multiple time points. Contact angles were obtained by microgoniometric measurement (Kyowa MCA-3, see supplementary). Droplet vibrations induced by the piezoelectric dispenser head[68-70] did not affect the measurements.[71] The advancing and receding contact angles are presented as opposed to the equilibrium contact angle to thoroughly describe

the surface wettability[72,73] and to characterize the force needed to hold the droplet stationary on an inclined condensing surface against the force of gravity, which directly affects condensation heat transfer[21,74,75] (see supplementary information). To determine the amount of adsorbed hydrocarbon, the surface carbon percent was measured from the relative peak magnitudes of the surface components observed from XPS spectra taken at each time point. Representative XPS spectra for holmia and ceria are presented in Figure 5. Comparison between the XPS spectra for pristine holmia and ceria and at 96 hours after cleaning reveals that a sharp carbon peak develops, often referred to as the "adventitious carbon" peak, which is indicative of adsorption of hydrocarbons onto the surface.[76] Note that hydrogen cannot be explicitly detected by XPS because it only has valence electrons, which are indistinguishable from other elements upon excitation and for which the binding energy is influenced by environment; therefore, determination of the average hydrocarbon chain length was not possible.[77]

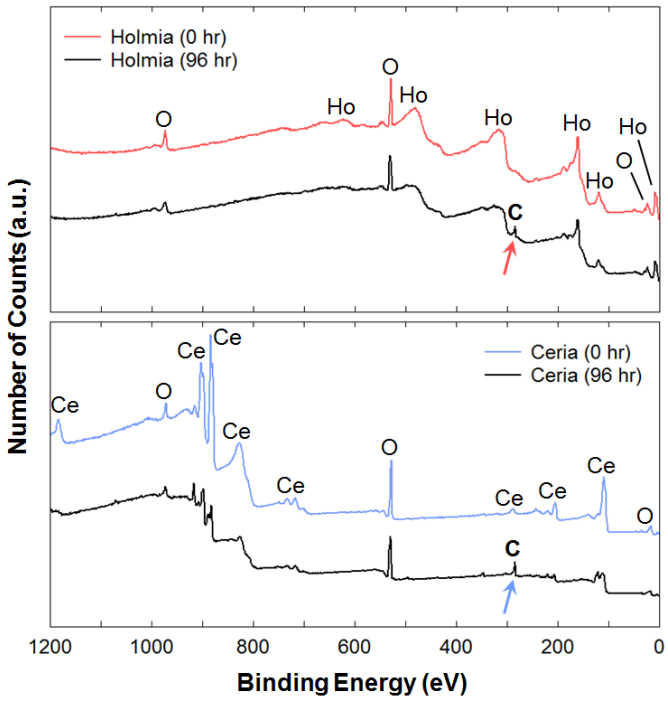

Figure 5. Survey XPS spectra of (a) holmia and (b) ceria immediately after argon ion bombardment (0 hr) and after 4 days exposed to laboratory air (96 hr). For both REOs, sharp carbon peaks developed by 96 hr which were not present at 0 hr, indicated here with arrows, which confirm the adsorption of hydrocarbons on the surface. The 0 hr spectra were shifted upwards by a constant value for comparison between spectra.

Table 1. Elements present on pristine REO (ceria and holmia) and control (silica and gold) surfaces in stoichiometric ratios after cleaning by bombardment with argon ions; atomic percent determined by XPS.

Sample	Element	Atomic %	Element	Atomic %
Holmia (Ho_2O_3)	Ho	41	O	59
Ceria (CeO_2)	Ce	33	O	67
Silica (SiO_2)	Si	34	O	66
Gold (Au)	Au	100	-	-

The average advancing contact angle measurements for each sample as a function of time after argon plasma cleaning started at ≈ 0° and increased asymptotically over time for every sample (Figure 6), with the REO's displaying hydrophobic (θ_a > 90°) behavior after 4 days. Note that both the advancing and receding angles for all of the surfaces except gold were less than 10° immediately after cleaning, and, as a result, the contact angle hysteresis was also initially less than 10° (the advancing/receding contact angles on gold were 46°/10° at the time of the first measurement). At 2448 hours (102 days) after cleaning, the average advancing angle reached 103° for holmia and 95° for ceria, which are within 10% of the previously reported values.[51] The advancing angles on gold and silicon reached 66° and 44°, respectively, which are in good agreement with the literature values for hydrocarbon contamination of these surfaces after cleaning to their pristine state and exposing to laboratory air.[40,55,78] Representative images of the advancing contact angle increase over time on the REOs are shown in Figure 6(b, c).

The increase in advancing contact angle over time suggests that the surface energy decreases over time, which can be attributed to the lower surface energy of the adsorbed hydrocarbons.[79] This trend has been previously shown for a variety of non-noble metal oxide materials including zirconium dioxide (ZrO_2) and titanium dioxide (TiO_2), among others, and occurs due to physisorption of hydrocarbons to OH^- groups and other energetically favorable sites present on the surface,[59,80] where van-der-Waals and hydrogen bonding are typical[81] but covalent bonding is also possible.[82-84] The results of the XPS analysis conducted here show that the amount of carbon present on the surface is indeed increasing over time, indicating that hydrocarbons adsorb to the cleaned surface after exposure to air. As shown in Figure 7a, the surface atomic percent of carbon increased from ≈ 0% immediately after cleaning to an asymptotic value of between 12 – 34% depending on sample type.

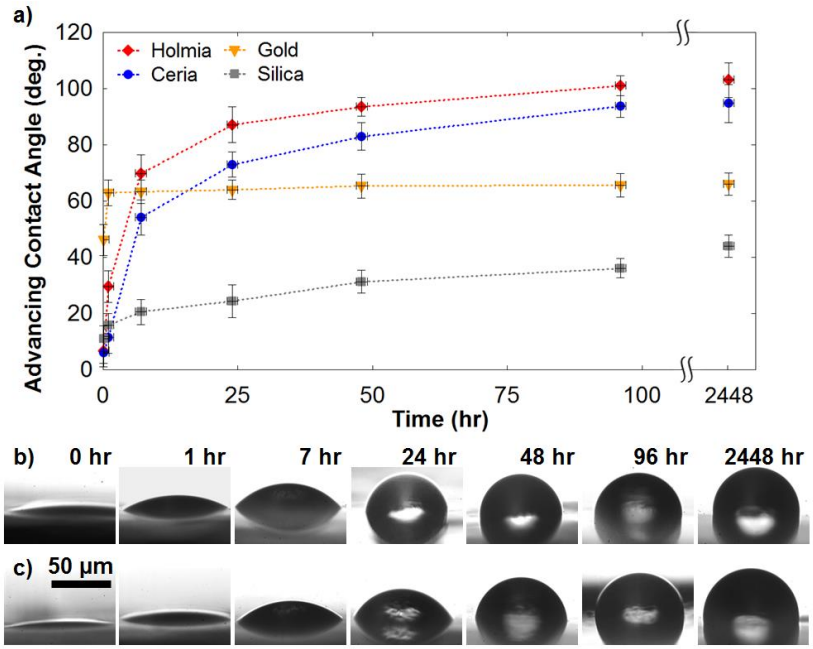

Figure 6. (a) Average advancing contact angle as a function of time for the REO (holmia and ceria) and control (gold and silica) samples exposed to laboratory air (temperature ≈ 25 °C, relative humidity ≈ 35%) with t=0 at the instant of argon ion bombardment surface cleaning. The average contact angle, defined as the mean of the contact angles measured on at least 5 spots on each sample, increased asymptotically with time for each sample. The error bars for the average contact angle range from 3-7° due to error in the measurement and variance between data points. Representative time-lapse images of advancing contact angles observed via microgoniometer are shown for (b) holmia and (c) ceria samples.

To explore the relationship between advancing contact angle and hydrocarbon adsorption, the measured advancing and receding angles are shown as a function of the surface atomic percent carbon for holmia and ceria in Figure 7(b, c). The advancing and receding contact angles increased with surface atomic percent carbon, where the advancing and receding contact angles are positively correlated with surface atomic percent carbon with a Pearson product-moment of at least 0.93 for all of the samples studied here. This correlation is in agreement with previous work for metals and metal oxides (see supplementary information). The mechanism for this relationship can be explained by considering the adsorbed hydrocarbons to be hydrophobic defects on an initially hydrophilic surface.[85] If the hydrocarbons are approximated as circular hydrophobic defects, then the advancing angle is predicted by:

$$\cos(\theta_A) = f_{max}\cos(\theta_{1,A}) + (1 - f_{max})\cos(\theta_{2,A}), \quad (1)$$

where θ_A is the advancing contact angle as a function of the surface coverage of hydrocarbons, f_{max}, which is determined from the surface atomic percent carbon and the relative sizes of the adsorbed hydrocarbons and the surface atoms, $\theta_{1,A}$ is the advancing contact angle of the hydrophilic surface with no adsorbed hydrocarbons ($\approx 0°$), and $\theta_{2,A}$ is the advancing contact angle on the surface once it has become saturated with hydrocarbons (approximated as the advancing angle at 2448 hours) (See expanded explanation in supplementary information). The curve obtained from this model is shown to fit well with the experimental data, indicating that hydrocarbon adsorption results in the observed increase contact angle. Modeling the receding angle in this case yields less useful information due to adhesion hysteresis of the adsorbed hydrocarbons and the variability in receding behavior as a function of time that the droplet remains on the surface.[86]

This work demonstrates that the hydrophobicity of REOs is due to hydrocarbon adsorption, as shown by the relationship between the increasing contact angle and surface carbon percent over time upon exposing a pristine surface to atmosphere. Similar to the noble metals and more typical metal oxides, pristine REOs have high surface energy, making them intrinsically hydrophilic. This study on the evolution in wetting behavior suggests that REOs can serve as coatings to induce dropwise condensation for improved heat transfer performance through the spontaneous adsorption of hydrocarbon material and subsequent effect on wetting behavior.

2.4 SUMMARY

This study provides insight on the wetting mechanism of the REO material group that suggests potential for implementation in other fields which make use of hydrophobic materials, including self-cleaning surfaces,[87] anti-icing surfaces,[88,89] water desalination,[8,9] and enhanced heat transfer surfaces.[47,90] Furthermore, our work highlights the importance of controlling hydrocarbon adsorption for material wetting characterization.

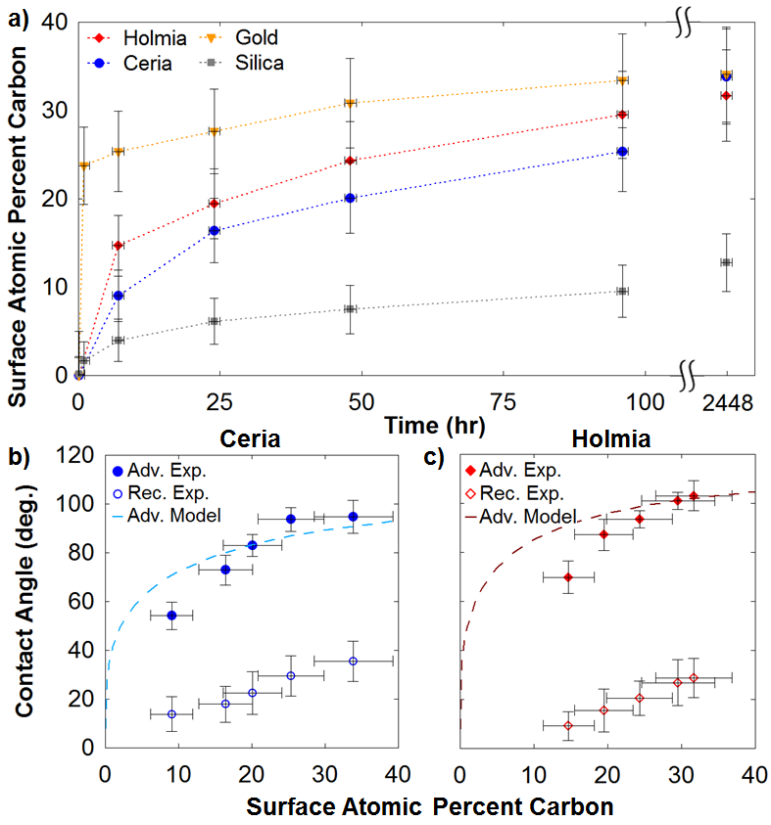

Figure 7. (a) Surface atomic percent carbon as a function of time for the REO and control samples exposed to laboratory air (temperature ≈ 25 °C, relative humidity ≈ 35%) with *t* = 0 at the instant of argon ion bombardment surface cleaning. Surface atomic percent carbon was calculated based on the relative peak sizes from XPS spectra taken at each data point and increased asymptotically with time. The error bars for surface atomic percent carbon range from 15-30% of the values shown due to error in the XPS measurement and the calculation of atomic percent from the spectra. The contact angle is shown as a function of surface carbon percent for (b) ceria and (c) holmia, and the advancing angle agrees well with a theoretical curve calculated from a model prediction accounting for hydrocarbons on a hydrophilic surface.

Chapter 3

3. Scalable Graphene Coatings for Enhanced Condensation Heat Transfer

In this chapter, we show the effectiveness of ultra-thin scalable chemical vapor deposited (CVD) graphene coatings to promote dropwise condensation while offering robust chemical stability and maintaining low thermal resistance. Heat transfer enhancements of 4*x* were demonstrated compared to filmwise condensation, and the robustness of these CVD coatings was superior to typical hydrophobic monolayer coatings. Our results indicate that graphene is a promising surface coating to promote dropwise condensation of water in industrial conditions, with the potential for scalable application *via* CVD.

3.1 INTRODUCTION

Graphene is a two-dimensional material composed of carbon atoms arranged in a hexagonal lattice which has received significant attention since 2004 due to its unique and remarkable physical properties.[91,92] Prominent examples of the applicability of graphene include electronic device interconnects due to high charge carrier mobility,[93] transparent electrodes for solar cell devices,[94,95] and membranes for water desalination.[8,96] Graphene has also been used in thermal management applications due to its ability to improve device thermal conductivity and spread heat.[97-99] However, with graphene being a relatively new material, many applications have not yet been thoroughly explored.

One such application is the promotion of dropwise condensation. Graphene displays hydrophobic behavior[100,101], and its inert chemical nature and demonstrated mechanical strength suggest that it will resist degradation under typical condenser conditions.[94,95,102,103] Furthermore, the thermal resistance of a graphene coating is well-characterized[104-106] and is negligible in condensation applications (see supplementary information), and it can be applied relatively scalably *via* CVD.[107,108] Although graphene was initially suggested to have complete wetting transparency[109], its hydrophobic nature has since been elucidated through careful experimental, numerical, and theoretical analysis.[100,101,110,111] Past work[109] also proposed graphene coatings to promote dropwise condensation, but the results of the experimental analysis did not show the expected improvement in heat transfer compared to filmwise condensation. The presence of non-condensible gases in the experimental setup not only reduced the improvement gained by

promoting dropwise condensation to 30–40% as opposed to 500–700%, but also resulted in reported condensation heat transfer coefficients three orders of magnitude lower than typical values without noncondensible gases.[21] Furthermore, the mechanism for the dropwise condensation behavior was attributed to the "transparent" graphene layer protecting the copper from oxidation and preserving the intrinsic hydrophobic behavior of copper, while it has been demonstrated that copper is actually intrinsically hydrophilic[112,113] like other high-surface-energy materials.[42,44,58,114,115]

In this work, we demonstrate the uniform coating of high-purity (> 99.99%) copper with graphene by both low and atmospheric pressure CVD. Both the low-pressure CVD (LPCVD) and the atmospheric pressure CVD (APCVD) graphene were single-layer. Subsequently, we experimentally demonstrated a 4x higher heat transfer coefficient for dropwise condensation of water on copper coated by graphene (both LPCVD and APCVD) compared to filmwise condensation on bare copper, in good agreement with theoretical models used for each case. The robustness of these graphene coatings was compared to a long-chain fluorocarbon monolayer commonly used to promote dropwise condensation, where 100°C steam was condensed on both samples continuously. The fluorocarbon monolayer coating degraded completely in under 12 hours, while for the graphene coatings, dropwise condensation was observed over a two-week span without showing signs of degradation. These results suggest that graphene is a robust and nonreactive coating material which enhances condensation heat transfer by promoting dropwise condensation.

3.2 SAMPLE PREPARATION

The copper samples used as substrates for graphene CVD were high purity tubes (>99.99%, OD = 1/4 inch, McMaster-Carr) and sections of sheet metal (>99.99%, thickness = 0.032 inch, McMaster-Carr). Prior to the CVD process, the copper samples were sonicated in acetone, triple-rinsed with deionized water, submersed in 2.0 M hydrochloric acid, again triple-rinsed with deionized water, and finally treated for 10 minutes with argon plasma (Harrick PDC-001), which removes hydrocarbons *via* physical bombardment.[64,66,67] This process was also used to clean the bare copper samples for characterization of filmwise condensation under ideal conditions since past work has shown that bare copper exhibits filmwise condensation during continuous condensation.[40,116,117]

The CVD process was then performed on the copper samples at both low and atmospheric pressure in a 1-inch quartz tube furnace. For both processes, the furnace was heated to 1000 °C, and hydrogen gas (with a flow rate of 10sccm) for the LPCVD process and argon gas (with a flow rate of 500 sccm) for APCVD process flowed over the samples for 30 min prior to graphene growth. Methane gas was then introduced,

and the synthesis of graphene was performed over 30 min at 1.9 Torr and atmospheric pressure for the LPCVD (with a flow rate of H_2/CH_4 = 70/4 sccm) and APCVD (with a flow rate of Ar/CH_4 = 500/3 sccm) coatings, respectively.[118-120] Finally, the samples were cooled to room temperature under hydrogen (10 sccm)/argon gas (500 sccm) for LPCVD/APCVD and then exposed to laboratory air (*i.e.*, non-filtered). While exposure to air leaves the possibility for contamination, the difference in wettability is expected to be negligible across different laboratory environments as indicated in past work[114] (Further characterization specifically for graphene contamination under several different environments is an important topic and should be investigated in future research).

We characterized the samples using field-emission scanning electron microscopy (Zeiss Ultra-Plus) to determine the surface morphology, shown in Figure 8. Copper grains are visible on both the LPCVD and APCVD surfaces, and it was observed that the graphene covered the entire surface of the copper. (The absence of visible copper grains on the bare copper surface is attributed to not heating the bare copper to

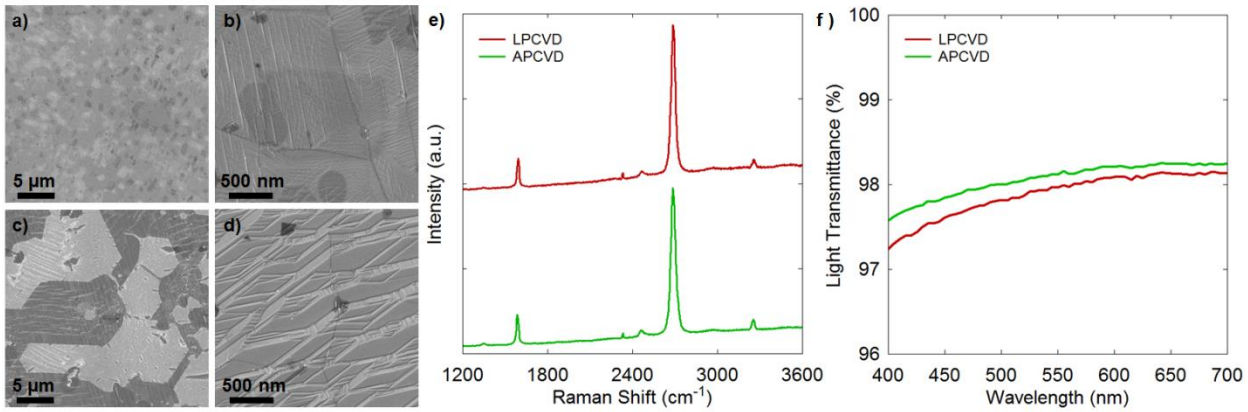

Figure 8. Field emission scanning electron microscopy images for (a, b) the low-pressure CVD graphene coating and (c, d) the atmospheric pressure CVD graphene coating on high-purity (> 99.99%) copper substrates. During growth, the native copper oxide layer is reduced by H_2 gas at high temperature, and the underlying copper forms pronounced grains. Upon exposure to a CH_4 at 1000 °C, graphene islands nucleate and grow over the surface until colliding with other islands. The copper grains remain visible. (e) Representative Raman spectra for the CVD graphene layers after transfer to a silicon substrate, obtained with a confocal Raman microscope using a 532 nm laser, demonstrate the presence of single-layer graphene for both CVD methods. (f) Optical characterization of the graphene transferred onto a transparent substrate indicated that both the LPCVD and APCVD graphene were predominately single-layer.[121]

1000 °C as is required during graphene CVD.) Further characterization of the samples was conducted with Raman spectroscopy using a confocal Raman microscope with a 532 nm laser. Representative Raman spectra for the CVD graphene coatings after transfer onto a silicon substrate are shown in Figure 1(e), where the ratio of 2D:G peaks (4–5x) and the full width at half maximum of the 2D peak (25–30 cm^{-1}) demonstrate the presence of single-layer graphene for both CVD methods. Optical characterization of the CVD graphene after transfer onto a transparent substrate (see Supporting Information) was also performed to study the graphene thickness over a larger area than the Raman laser spot size (Raman spot size is ~1 μm while the transmittance measurement spot size is ~5 mm). The optical characterization indicated that both the LPCVD and APCVD graphene were predominately single-layer.[121]

We determined the surface wetting properties for water by goniometric characterization, where the advancing and receding contact angles in Figure 9 describe the surface wettability.[72,73] Both the advancing and receding contact angles need to be considered to determine the force which holds a droplet stationary on an inclined condensing surface against the force of gravity, which directly affects droplet departure size and condensation heat transfer.[25,122-124] The average advancing/receding contact angles were 87±5°/64±5° for the LPCVD graphene and 93±5°/56±5° for the APCVD graphene, determined from six points on each sample using a piezoelectric picoliter-scale droplet dispenser microgoniometer (Kyowa MCA-3) with the receding contact angle obtained during droplet evaporation and observed to exhibit constant receding contact angle behavior.[125] The contact angle hysteresis was attributed to sporadic defects on the surface, possibly at graphene grain boundaries. The droplet departure size during water vapor condensation, defined as the diameter at which droplets begin to slide down the condenser wall, is shown in Figure 9(c, f). The average droplet departure diameters were 2.4 ± 0.1 mm on LPCVD graphene compared to 2.8 ± 0.1 mm on APCVD graphene, suggesting that the condensation heat transfer coefficient on LPCVD graphene will be slightly higher than on APCVD graphene as droplets shed at smaller sizes and refresh the surface for re-nucleation. The contact angle on the clean bare copper surface was ≈0°, with no distinction between advancing and receding.

3.3 HEAT TRANSFER CHARACTERIZATION

We experimentally obtained the overall heat transfer performance of the graphene-coated copper tubes in a controlled vacuum chamber. Prior to condensation experiments, the vacuum chamber was evacuated to a pressure of $P < 1.0$ Pa to eliminate the presence of noncondensable gases, which have been shown to severely degrade condensation heat transfer performance.[126,127] Water vapor was then introduced from a canister of degassed, deionized water attached to the vacuum chamber. The copper tube temperature was

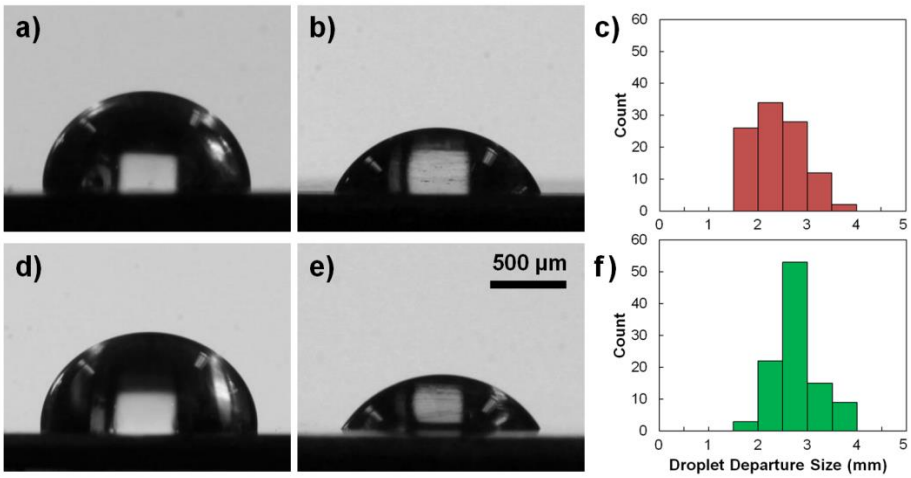

Figure 9. Representative images of (a) advancing and (b) receding contact angles of water on LPCVD graphene grown on a high-purity copper substrate, obtained by goniometric measurement. A histogram of droplet departure size during water condensation on LPCVD graphene is shown in (c). The advancing and receding contact angle for water on APCVD graphene are shown in (d) and (e), respectively, and a histogram of droplet departure size during water condensation on APCVD graphene is shown in (f). The average droplet departure diameter during water condensation on APCVD graphene is 2.8 ± 0.1 mm compared to 2.4 ± 0.1 mm on LPCVD graphene, suggesting a slightly higher expected condensation heat transfer coefficient on LPCVD graphene than on APCVD graphene.

regulated by an internal chiller water flow loop which was isolated from the interior of the vacuum chamber, and the heat transfer through the tube wall was determined as a function of the chiller water flow rate and chiller water temperature at the tube inlet and outlet. As the copper tube was chilled internally, water vapor within the chamber condensed on the outer tube surface. The water vapor pressure within the chamber was maintained at values ranging from 2 to 5 kPa (corresponding to saturated water temperatures of 17 to 33℃), which are typical for industrial condenser applications.[128,129]

Photographs of condensation on the exterior tube surfaces are shown in Figure 10. The bare copper tube underwent filmwise condensation of water vapor regardless of the temperature difference between the tube and the surrounding water vapor due to the spreading nature of water on clean copper (Figure 10(a,b)). The LPCVD (Figure 10(c,d)) and APCVD (Figure 10(e,f)) graphene coated tubes have visible graphene layers when dry (Figure 10(c,e)), and these coated tubes exhibited dropwise condensation over the full range of experimental conditions.

The overall heat flux, determined by the change in sensible heat of the chiller water, was obtained along with the log mean temperature difference (LMTD) between the chiller water and the temperature corresponding to the pressure of the surrounding water vapor for the bare copper (diamonds), LPCVD graphene (squares), and APCVD graphene (circles) (Figure 11(a)). The overall heat flux increased monotonically with the LMTD, where the local slope of this curve represents the overall heat transfer coefficient. Figure 11(b) shows the condensation heat transfer coefficient extracted from the overall heat transfer coefficient (see Supporting Information) as a function of vapor pressure while holding the supersaturation $S = P_{vapor}/P_{sat}(T_{wall})$ constant (S = 1.2). The theoretical predictions (dashed curves) were obtained from the droplet growth and distribution model for the graphene-coated condenser and from the Nusselt model for filmwise condensation on the bare copper condenser, and were in good agreement with the experimental data (for model derivation and parameters, see Supporting Information). The assumption of uniform wall temperature for the models was justified because the temperature variation in the chiller water from the inlet to outlet of the sample was over an order of magnitude less than the temperature difference from the sample to the surrounding vapor. The condensation heat transfer

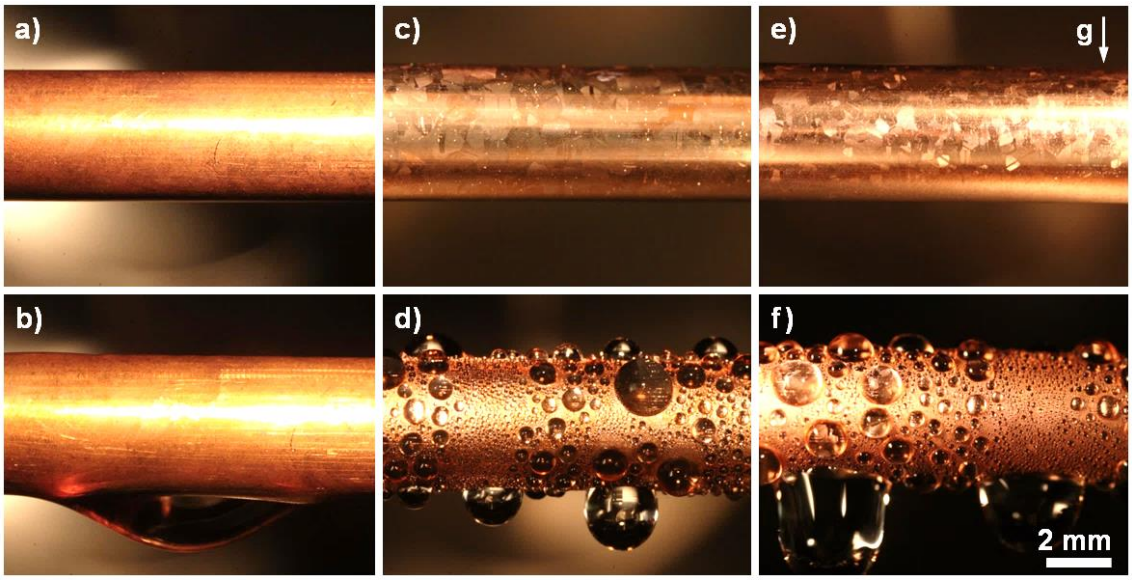

Figure 10. Photographs of a clean high-purity copper condenser tube (a) under vacuum and (b) undergoing filmwise condensation of deionized and degassed water vapor in the experimental vacuum chamber. Similarly, photographs of the graphene-coated high-purity copper condenser tubes are shown under vacuum and undergoing dropwise condensation of water, with the LPCVD graphene coating in (c) and (d) and the APCVD graphene coating in (e) and (f).

coefficient for the LPCVD and APCVD graphene coated copper tubes (≈60 ± 20 kW/m^{2}K) was 4x greater than that measured for filmwise condensation on bare copper (≈15 ± 9 kW/m^{2}K). Note that the dropwise condensation heat transfer coefficient decreases at low subcooling because the interfacial heat transfer coefficient becomes a major resistance to heat transfer,[21,47,130] while the filmwise condensation heat transfer coefficient increases at low subcooling as the film becomes thinner;[15] consequently, while a 4x enhancement was expected for the subcooling range used to characterize the heat transfer coefficient in the present work (3.5-5 K), the typically reported 5-7x heat transfer coefficient enhancement[21] would be realized at higher subcooling (over ≈10 K, see supplementary information).

The error for the condensation heat transfer coefficient was determined by propagating uncertainties associated with the chiller water thermocouples and mass flow meter, the pressure sensor inside the chamber, the sample surface area, and the Gnielinski correlation for heat transfer from the chiller water

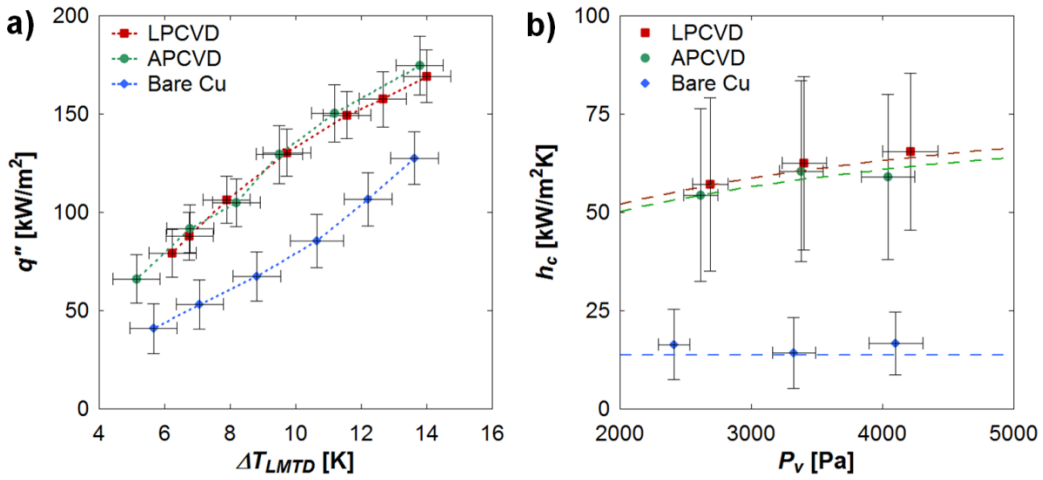

Figure 11. Water condensation heat transfer performance for the copper tubes with and without graphene coatings. The graphene-coated condensers exhibit dropwise condensation, while the bare copper undergoes filmwise condensation. Overall surface heat flux (q") is shown as a function of the steady state experimental chiller-water-to-vapor log mean temperature difference (ΔT_{LMTD}) in (a), where the slope of the data trend represents the overall heat transfer coefficient, that is, the combination of the chiller water flow, copper tube, graphene coating (for coated tubes), and condensation heat transfer coefficients. (b) Experimental (points) and theoretical (dashed curves) steady-state condensation heat transfer coefficient (hc), which includes graphene coatings where applicable, as a function of surrounding saturated vapor pressure (P_v). Error bars indicate the propagation of error associated with the fluid inlet and outlet temperature differential (±0.2 K) and pressure measurement (±2.5%). Theoretical predictions were obtained from the droplet growth and distribution model for the graphene-coated condensers with droplet departure size as an input parameter (for model derivation and parameters, see Supporting Information) and from the Nusselt model for filmwise condensation on the bare copper condenser.

bulk to the internal surface of the sample. Since the condensation heat transfer coefficient, h_c, is not simply a function of a product of powers, the error must be determined from the first partial derivatives of h_c with respect to its components along with the uncertainties of its components (described in detail in the supplementary information).

3.4 ROBUSTNESS CHARACTERIZATION

In addition to improved condensation heat transfer by promoting dropwise condensation, graphene coatings also exhibit inert chemical behavior and excellent mechanical strength, which are expected to result in improved resistance to routine wear during condensation and provide a robust alternative to current state-of-the-art dropwise functionalization coatings. For direct comparison, a monolayer coating of trichloro(1H,1H,2H,2H-perfluorooctyl)silane (TFTS) was applied to a clean copper sample and, along with the graphene-coated samples, underwent an accelerated endurance test which consisted of continuous condensation of 100 °C steam. The TFTS coating was applied *via* vapor-phase deposition, where the copper substrate was cleaned as described for the graphene CVD, but oxygen plasma was substituted for argon plasma. The copper substrate was then placed in a dessicator immediately following the oxygen plasma treatment along with a vial containing 2 mL of TFTS. The dessicator was evacuated with a vacuum pump for 90 seconds, after which the sample was left in the TFTS vapor for 10 minutes. The sample was then removed from the dessicator, solvent rinsed, and dried with a clean nitrogen stream. The advancing/receding contact angles were 120±5/82±5° on the TFTS-coated copper sample as fabricated.

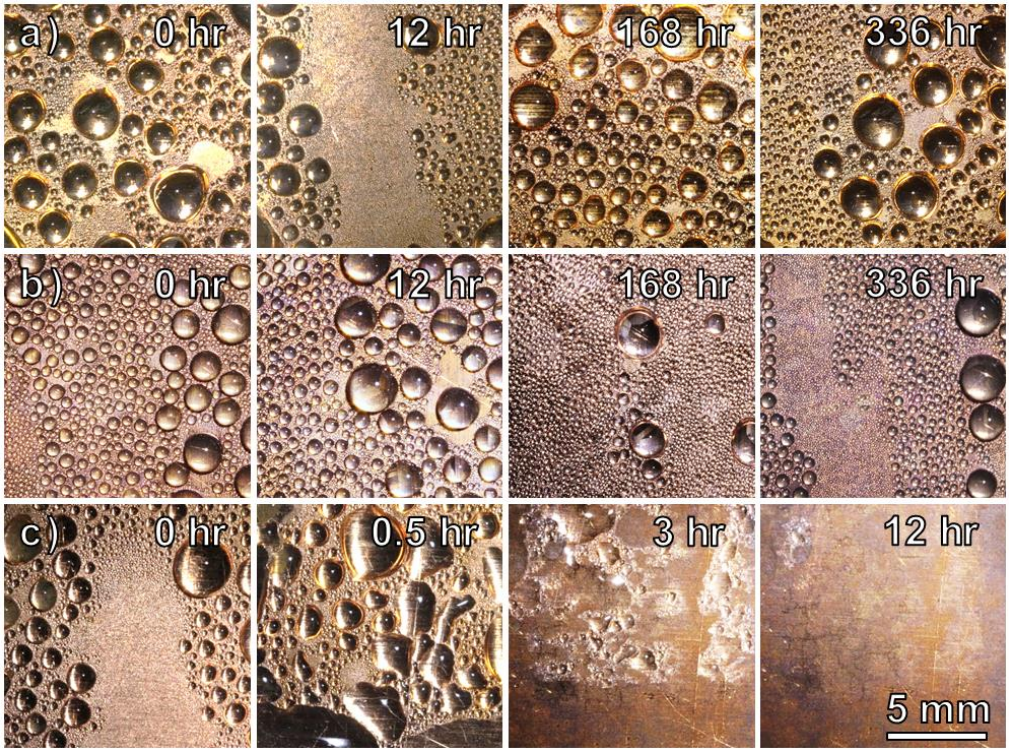

Figure 12. Time-lapse images of continuous condensation of 100 °C steam on (a) LPCVD, (b) APCVD, and (c) TFTS coatings on high-purity copper samples. The robust promotion of dropwise condensation by the graphene coatings is investigated over two weeks without showing signs of degradation, in contrast with the TFTS coating, which degraded and transitioned to filmwise condensation in less than 12 hours.

The endurance test was performed in a controlled positive-pressure continuous condensation chamber (see supplementary information). The samples were cooled to a surface temperature of 95±1 °C and exposed to a continuous supply of 100 °C steam provided from a reservoir of degassed, deionized water. Initially, dropwise condensation was observed on both the LPCVD and APCVD graphene coated samples and the TFTS coated sample (first column of Figure 12). However, the TFTS coating degraded noticeably within the first 30 min of testing, with decreased advancing and receding contact angles observed, and completely transitioned to filmwise condensation within 12 hours (Figure 12(c)), likely due to stripping of the coating by oxidation (X-ray photoelectron spectroscopy (K-Alpha) revealed that only 3% of the originally observed atomic percent of fluorine, a primary component of TFTS, remained on the surface after the continuous condensation experiment).[33,131] Conversely, the LPCVD and APCVD graphene coated samples both sustained dropwise condensation for over two weeks with no signs of

degradation when the experiments were discontinued (Figure 12(a,b)). Additionally, these graphene coatings can be altered to multi-layer graphene or even single-/multi-layer graphene composites[132] without drastic effect on the heat transfer (since the added thermal resistance is negligible, see supplementary information) and can thus potentially be tailored to better prevent oxidation if it poses a problem. Further discussion on graphene's chemical robustness is presented in the supplementary information.

3.5 SUMMARY

While graphene offers a robust coating material to promote dropwise condensation on industrial metals, it is not a likely candidate to induce superhydrophobic behavior on micro- and nanostructured materials due to its relatively low advancing and receding contact angles compared to fluoropolymer coatings typically used for this application. While this eliminates the ability of graphene-coated surfaces to promote jumping droplet condensation,[90,133-140] the improvement in heat transfer coefficient of 4x provided by dropwise-promoting graphene coatings compared to filmwise condensation outweighs the marginal additional increase of 30-40% gained by jumping droplet condensation compared to dropwise condensation. Another potential limitation of these graphene coatings is their inability to induce dropwise condensation in systems which use low-surface-tension working fluids such as pentane; these fluids are expected to exhibit low contact angles and spread on graphene-coated surfaces, resulting in filmwise condensation.

This study demonstrates that graphene CVD coatings are a viable method to promote dropwise condensation of water in industrial conditions, with a demonstrated improvement in heat transfer performance of 4x compared to clean industrial metals and superior robustness compared to state-of-the-art dropwise-promoting monolayer coatings as demonstrated under continuous condensation of 100 °C steam. This result promises significant energy savings in applications such as water harvesting, thermal management, industrial power generation, and building heating and cooling.

Chapter 4

4. Lubricant Infused Surfaces for Enhanced Condensation of Water and Low Surface Tension Fluids

Low surface tension fluid condensates such as hydrocarbons pose a unique challenge since typical hydrophobic condenser coatings used to promote dropwise condensation of water often do not repel fluids with lower surface tensions. Recent work has shown that lubricant infused surfaces (LIS) can promote droplet formation of hydrocarbons; we confirm the effectiveness of LIS in promoting dropwise condensation here by providing the first experimental measurement of heat transfer performance during hydrocarbon condensation on a LIS, which enhances heat transfer by ≈ 500% compared to an uncoated surface. We also explore improvement through removal of noncondensable gases and address a failure mechanism whereby shedding droplets deplete the lubricant over time. Improved condensation heat transfer for low surface tension fluids on LIS presents the opportunity for significant energy savings in natural gas processing as well as improved device thermal management, heating and cooling, and power generation.

4.1 INTRODUCTION

During water condensation, the dropwise mode is promoted with thin hydrophobic coatings.[141] However, low surface tension fluid condensates such as hydrocarbons pose a unique challenge since the typical hydrophobic condenser coatings used to shed water (surface tension $\gamma \approx 73$ mN/m) often do not repel fluids with lower surface tensions ($\gamma < 30$ mN/m). Reentrant and doubly-reentrant surface designs have been proposed for repellency of low surface tension impinging droplets,[142,143] but these schemes are not useful during condensation when the impinging fluid can nucleate within the structures and subsequently render the surface hydrophilic.[144,145]

Meanwhile, lubricant infused surfaces (LIS) have found use in nanoscale research,[146] fluid dynamics,[147] heat transfer,[148,149] and the even the biological[150] and lab-on-a-chip[151] fields, among others,[152-156] due to their impressive ability to shed impinging droplets. A LIS is comprised of a rough structured solid surface into which a lubricant is "infused," or spontaneously wicked,[157] and on which an impinging fluid ideally forms discrete droplets which easily shed from the surface. Crudely conceived in 1959[158] and explored briefly in subsequent work,[159,160] LIS were brought to prominence through developments

reported independently by LaFuma and Quere[161] and Wong et al.[162] in 2011 and have subsequently been described in more detail in applications including condensation enhancement,[24] anti-icing,[154] and paper-based microfluidics.[153]

LIS have also been shown repel low surface tension fluids,[162,163] which is critical for applications in thermal management and hydrocarbon processing; for example, LIS can promote formation of highly mobile droplets of low surface tension fluids, including hydrocarbons with surface tensions as low as pentane ($\gamma \approx 16$ mN/m).[162] LIS have also been shown to improve condensation heat transfer of water in the dropwise mode.[24] The natural combination of these two research directions is the use of LIS to promote dropwise condensation of low surface tension fluids. The behavior during condensation of hydrocarbons and other low surface tension fluids on LIS has been reported qualitatively and suggests that LIS are a promising solution to promote dropwise condensation of hydrocarbons, but no experimentally-measured improvement in heat transfer has been reported.[163]

In the present work, we quantitatively confirm the effectiveness of LIS in promoting dropwise condensation. First, we report the experimentally-measured condensation heat transfer coefficients during water condensation in a controlled environmental chamber in the filmwise mode and during dropwise condensation on a flat hydrophobic surface and a LIS. Then, the heat transfer performance was determined during condensation of the hydrocarbon toluene ($\gamma \approx 28$ mN/m) on bare surfaces in the filmwise mode and on LIS-coated tubes in the dropwise mode at a range of supersaturations typical for natural gas processing applications. From these results, the heat transfer coefficient for hydrocarbon condensation on LIS was obtained experimentally. The ≈ 500% experimentally observed improvement in heat transfer for low surface tension fluids condensing on LIS presents the opportunity for significant energy savings not only in natural gas processing but also applications such as thermal management, heating and cooling, and power generation.

4.2 RESULTS

In order to perform condensation experiments, we first fabricated tube samples. The tube sample used to promote filmwise condensation of both water and toluene was bare copper which was first solvent cleaned and then plasma cleaned (see Methods). The tube sample used to promote dropwise condensation of water was functionalized with a monolayer of the hydrophobic coating octadecyltrichlorosilane (OTS), but this sample was unable to promote dropwise condensation of toluene as discussed later. The tube sample used to test condensation of both water and toluene on a LIS was a copper tube which was first

coated with copper oxide (CuO) nanoblades etched following a well-known procedure.[49,164-168] The CuO nanoblades were then functionalized with a monolayer coating of (TFTS) to reduce the surface energy.[169,170] Finally, the lubricant, Krytox GPL 101 fluorinated oil, was added to the surface (see Methods for details).

Experiments were conducted in an environmental chamber (Figure 13(a)). The chamber allowed the level of noncondensable gases to be controlled via a vacuum pump, including complete removal of NCGs from the system (< 1 Pa). Following removal of noncondensable gases, pure, degassed vapor of the condensing fluid (either water or toluene) was introduced into the chamber from a heated, temperature-controlled canister and allowed to condense on the sample. The sample temperature was maintained with an internal flow of coolant water, where the sensible heating of the coolant fluid from the inlet to the outlet of the sample was characterized with thermocouples and used to determine the overall heat flux (Figure 13(b)). The condensation heat transfer coefficient, h_c, was then calculated from the thermal resistance network shown in Figure 13(c), where the thermal resistances of the internal flow and conduction through the tube wall are known. We first characterized filmwise condensation of both water and toluene on the bare copper tubes and compared the results to Nusselt's falling-film theory in order to validate the experimental results.[171] The experimental results were in good agreement with Nusselt's model for both water and toluene (Figure 14(a, b)). The slight overprediction by the model is due to the assumption that fluid reaching the bottom of the tube is immediately removed, while in reality the fluid accumulates at the bottom of the tube and eventually sheds as droplets, resulting in a higher average conduction resistance through the condensing fluid than in Nusselt's model.

We went on to characterize the condensation of water and toluene on the flat hydrophobic coated tube, where we observed that water underwent dropwise condensation (Figure 15(a)) but toluene exhibited filmwise behaviour (Figure 15(c)). While we initially observed the nucleation and growth of small, discrete droplets of toluene on the flat hydrophobic surface, at any appreciable heat flux the toluene transitioned to filmwise condensation as can be expected for a low condensate contact angle combined with non-negligible contact angle hysteresis.[21,141,172] This illustrates the difficulty of condensing low surface tension fluids on typical hydrophobic coatings. Due to the failure of toluene to achieve dropwise condensation on the hydrophobic surface, we do not report any data for dropwise condensation of toluene on the flat hydrophobic surface. Meanwhile, the heat transfer performance for dropwise condensation of water outperformed filmwise condensation and was also in good agreement with a model based on

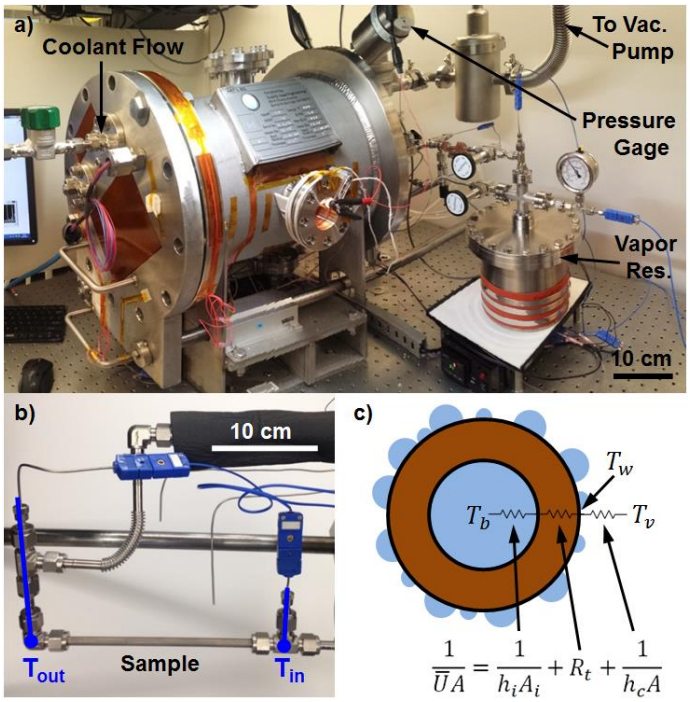

Figure 13. Environmental chamber with tube condenser sample to experimentally measure condensation heat transfer performance. The environmental chamber (a) can be evacuated to < 1 Pa to remove noncondensable gases. Pure, degassed vapor is introduced into the chamber from a reservoir and condensed on the exterior surface of the tube sample (b), while the sample temperature is maintained by a flow of coolant through the interior of the tube. The condensation heat transfer coefficient h_c is determined from a thermal resistance network (c) for the tube sample.

individual droplet heat transfer integrated over a known droplet size distribution as shown in Figure 14(a) (see supplementary information for model description).[173]

Finally, we condensed water and toluene on the LIS. In a previous experiment in which water was condensed on a LIS performed by Xiao et al., the condensation heat transfer coefficient was measured experimentally and reported to be 100% greater than that of dropwise condensation on a flat surface; however, the heat transfer coefficients reported in this work for dropwise condensation on both the flat hydrophobic and LIS were worse than the expected value for filmwise condensation calculated from Nusselt's model (see supplementary information).[24] This study had included NCGs (30 Pa) in the chamber during the condensation heat transfer measurements, which are known to degrade heat transfer performance due to buildup at the condenser surface and an accompanying resistance due to vapor

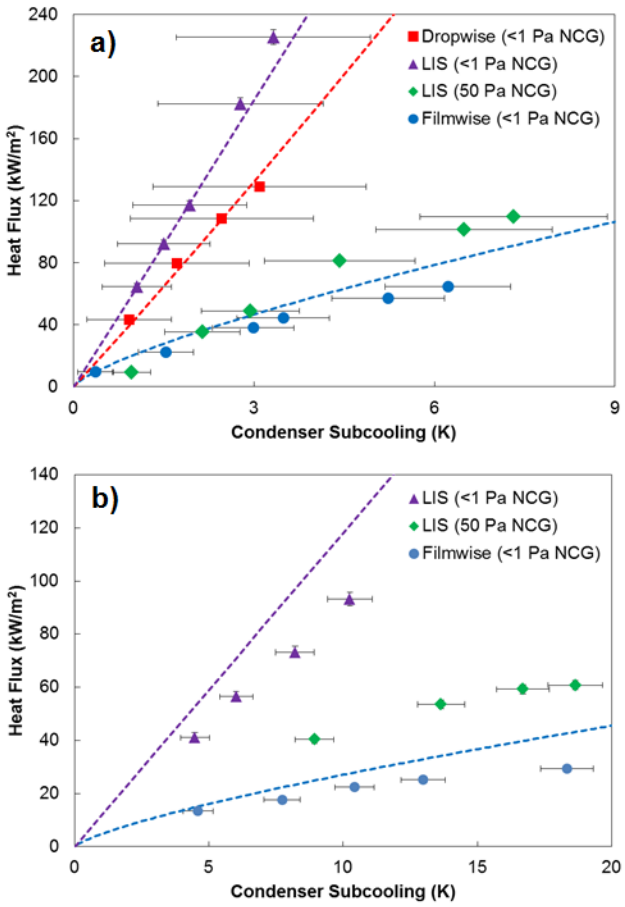

Figure 14. Heat flux as a function of condenser subcooling ($T_v - T_w$) for water and toluene. (a) Water is condensed onto a bare copper tube in the filmwise mode, a flat hydrophobic copper tube in the dropwise mode, and a LIS-coated copper tube in the dropwise mode in pure vapor and with 50 Pa of noncondensable gas (NCG) present in the chamber. (b) Toluene is condensed onto a bare copper tube in the filmwise mode and a LIS-coated copper tube in the dropwise mode in pure vapor and with 50 Pa of noncondensable gas (NCG) present in the chamber. Toluene condensation on the flat hydrophobic copper tube resulted in the filmwise mode.

diffusion through the NCG layer.[141,174,175] While the NCGs were reported to serve the purpose of preventing evaporation of the lubricant,[24] we found that the vapor pressure of Krytox GPL 101 is much less than 1 Pa, and therefore we were able to run experiments with virtually no NCG while still maintaining the presence of the Krytox lubricant on the surface. However, experiments were performed both without (i.e., < 1 Pa) NCG and with 50 Pa NCG present to explore the effect of NCG on heat transfer performance and determine whether this could be the mechanism whereby Xiao et al. reported condensation heat transfer coefficients much lower than expected from modelling.

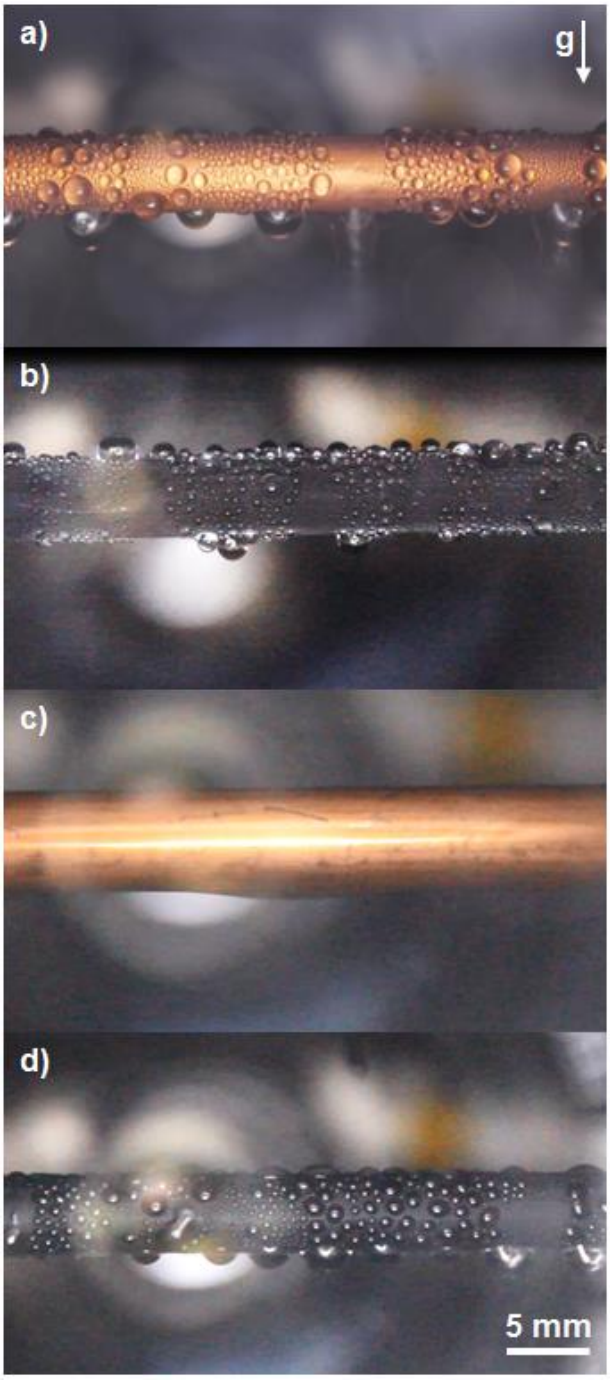

Figure 15. Photos of condensation of water (a, b) and toluene (c, d). Water is condensed on the flat hydrophobic surface in (a) and on the LIS in (b). Toluene is condensed on the flat hydrophobic surface in (c) and on the LIS in (d). Droplet departure diameters were calculated from videos of condensation and used in the model to predict the expected dropwise heat transfer coefficients on the flat hydrophobic surface and the LIS, see supplementary information.

Condensation of both water and toluene on the LIS exhibited clear dropwise behaviour (Figure 15(b, d)). In the presence of NCG, the heat transfer performance was only marginally better than filmwise condensation, rationalizing the result obtained by Xiao et al.[24] When NCG were removed from the chamber, the heat transfer performance during water condensation exceeded that of dropwise condensation by ≈ 30% and filmwise condensation by ≈ 400%. Toluene condensation on the LIS outperformed filmwise condensation by ≈ 500%, in good agreement with the model prediction by Rykaczewski et al. of a ≈ 600% enhancement for toluene condensing on a LIS.[163] Furthermore, experimental results for both water and toluene condensation on the LIS were in good agreement with the condensation heat transfer model, where the droplet size distribution used in the model for LIS was adjusted according to recent work (see supplementary information).[176]

The long-term performance of surface coatings is often a consideration when they are proposed for industrial applications. LIS are particularly concerning in this regard, as the lubricant may be depleted from the surface over time due to several mechanisms. If the droplets of condensate are "cloaked," or covered in a thin layer of lubricant, they will carry lubricant with them during shedding and deplete the lubricant over time.[177-179] Another depletion mechanism is shearing of the lubricant, which may also occur due to droplet shedding as droplets slide over the LIS, causing accumulation of lubricant at the bottom of the condenser.[147,180] In order to test the failure mechanism of the LIS during hydrocarbon condensation, we continuously condensed toluene on the LIS over the course of 6 hours. We found that the surface failed on the order of 1 hour, in agreement with another recent study on LIS which reported that low viscosity lubricants failed in less than 1 hour but did not explore the failure in further detail.[176] The condensation transitioned from dropwise to filmwise, with a corresponding decrease in heat transfer coefficient of ≈ 80% (= 1 – 1/500%) shown in Figure 16. We also observed that the degradation began at the top of the condenser surface and slowly moved downwards. Since toluene is not cloaked by Krytox,[163] the droplet shearing effect[147,180] is primarily responsible for the LIS failure in this case as evidenced by the accumulation of lubricant at the base of the condenser over time.

4.3 DISCUSSION

Applying LIS to a condenser is shown here to be a viable approach to promote dropwise hydrocarbon condensation and improve the heat transfer coefficient. This is not the only solution to improve heat transfer during condensation of low surface tension fluids; in some cases, it is also possible to modify the functionalizations on flat condenser surfaces to lower the surface energy until droplet formation is energetically favorable,[163] particularly with fluorinated carbon chains.[181] However, geometric and

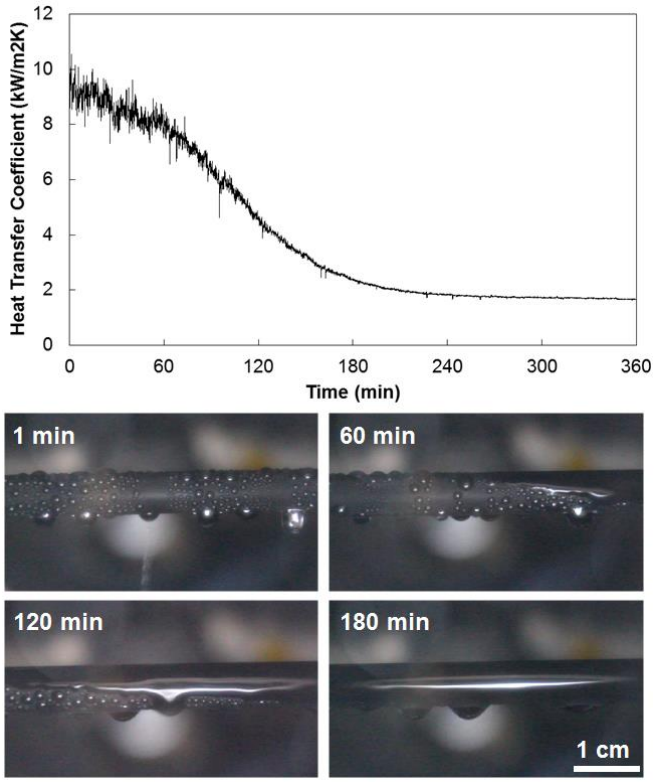

Figure 16. Toluene condensation on the LIS over time. Toluene initially exhibits dropwise condensation on the LIS, but within 1 hour the surface begins to transition to filmwise condensation. The lubricant is forced the bottom of the condenser by shear force imparted by shedding droplets rendering the top of the condenser surface wettable by toluene. Correspondingly, the heat transfer coefficient is degraded by approximately 80%. Upon rewetting the surface with lubricant, the surface could again shed discrete droplets of toluene, indicating that the failure was due to lubricant depletion and not structural damage.

chemical defects on solid surfaces result in contact angle hysteresis,[85] and a high level of contact angle hysteresis can cause a transition to filmwise condensation as heat flux increases.[141] The low contact angle hysteresis found on LIS therefore provides an advantage compared to flat surfaces as it may allow continued shedding of droplets of low surface tension fluids at higher heat fluxes.[141,159,162]

4.4 SUMMARY

Even in light of the challenges highlighted above that must be addressed before LIS will find practical use as a condenser coating, the enhancements in heat transfer coefficient versus filmwise condensation of 400% and 500% for water and toluene, respectively, suggest that LIS merit further exploration.

Specifically, promotion of dropwise condensation of low surface tension fluids on LIS where flat coatings may not suffice due to contact angle hysteresis is a promising future direction. The demonstrated condensation heat transfer enhancement indicates that a large impact in natural gas processing as well as improved device thermal management, heating and cooling, and power generation is possible.

4.5 METHODS

Flat Hydrophilic Tube Samples – To create bare copper (Cu) hydrophilic tube samples, commercially available oxygen-free Cu tubes (99.9% purity) with outer diameters, D_{OD} = 6.35 mm, inner diameters, D_{ID} = 3.56 mm, and lengths, L = 131 mm were obtained. Each Cu tube was cleaned in an ultrasonic bath with acetone for 10 minutes and rinsed with ethanol, isopropanol, and deionized (DI) water. The tubes were then dipped into a 2.0 M hydrochloric acid solution for 10 minutes to remove the native oxide film on the surface, then triple-rinsed with DI water and dried with clean nitrogen gas (99.9%, Airgas). Finally, within 30 minutes before any experiment using the bare Cu tubes, the samples were cleaned with argon plasma to remove adsorbed hydrocarbons which are known to render metal and metal oxide surfaces hydrophobic.[114,182-184]

Flat Hydrophobic Tube Samples – The hydrophobic tube samples were fabricated by functionalization of the flat copper surface with octadecyltrichlorosilane (OTS). A bare copper tube cleaned as described for the hydrophilic samples in the previous section was immersed in a 0.1% by volume solution of OTS (> 90%, Sigma) in n-hexane (99%, Sigma) for 5 minutes as described in prior work.[185,186] The coating had typical advancing/receding contact angles of $\theta_a/\theta_r \approx 104/93 \pm 3^\circ$ when measured on a flat reference surface.

LIS Samples – To create the CuO nanostructures, commercially available oxygen-free Cu tubes were used (99.9% purity) with outer diameters, D_{OD} = 6.35 mm, inner diameters, D_{ID} = 3.56 mm, and lengths, L = 131 mm, as the test samples for the condensation experiments. Each Cu tube was cleaned following the same procedure as the bare copper tubes. Nanostructured CuO films were formed by immersing the cleaned tubes (with ends capped) into a hot (96 ± 3 °C) alkaline solution composed of $NaClO_2$, NaOH, $Na_3PO_4 \cdot 12H_2O$, and DI water (3.75 : 5 : 10 : 100 wt.%).[164,169] During the oxidation process, a thin (≈ 300 nm) Cu_2O layer was formed that then re-oxidized to form sharp, knife-like CuO oxide structures with heights of $h \approx 1$ μm, solid fraction $\varphi \approx 0.038$ and roughness factor $r \approx 4$.

The CuO structures were then functionalized with trichloro(1H,1H,2H,2H-perfluorooctyl)silane (TFTS) (Sigma), which was deposited from the vapor phase. Prior to silane deposition, each tube was oxygen plasma cleaned for 2 hours to remove organic contaminants on the surface. Once clean, the tube samples were immediately placed in a vacuum desiccator (06514-10, Cole Parmer) with a small amount of liquid TFTS. The desiccator was evacuated by a roughing pump for 2 minutes to a minimum pressure of ≈ 2 kPa. A valve was then closed to isolate the pump from the desiccator and the sample was held in vacuum (≈ 2 kPa) for another 10 minutes. The functionalized tubes were then rinsed in ethanol and DI water and dried in a clean nitrogen stream (99.9%, Airgas). The coating had a typical advancing contact angle of θ_a ≈ 119˚ when measured on a flat reference surface and typical advancing/receding angles of θ_a/θ_r ≈ 171/167 ± 3˚ when measured on the functionalized nanostructured CuO surface.

The surface was infused with lubricant by first placing a few droplets of Krytox GPL 101 lubricant onto the surface and allowing them to spread completely, then using a clean nitrogen stream (99.9%, Airgas) to remove excess lubricant.

Chapter 5

5. Design of Lubricant Infused Surfaces

The design of LIS has been explored in terms of surface energies which must be determined empirically. We developed a model which uses a prediction of these surface energies to determine whether an arbitrary combination of solid and lubricant will repel a given impinging fluid. This model was validated against experiments performed in the present work as well as the literature and subsequently used to develop a new framework for LIS design, where we demonstrated that commonly cited guidelines in the literature are often misleading or incorrect. We went on to design LIS on uncoated high-surface-energy solids, thereby eliminating the need for unreliable low-surface-energy coatings, and experimentally demonstrated repulsion of the lowest surface tension impinging fluid (butane, $\gamma \approx 13$ mN/m) reported to date on a LIS.

5.1 INTRODUCTION

The design of these surfaces, specifically the choice of a rough solid and a lubricant for a given impinging fluid, is well-understood from an energetic standpoint.[161,162,178] The LIS must meet the following criteria: the impinging fluid must be immiscible with the lubricant, the lubricant must wet the solid structures both with and without the impinging fluid present, and the impinging fluid must form discrete droplets on the LIS as opposed to a continuous film. All of the work on LIS design has presented models which require either contact angles or spreading coefficients of the impinging fluid and lubricant on the solid surface, as well as the interfacial tension between the lubricant and the impinging fluid; unfortunately, these properties have been measured empirically in past work and used to justify LIS behaviour after experiments with the LIS were already conducted. Predictive capability is not possible for combinations of fluids and solids where empirical results for these quantities are not readily available.

In the present work, we have developed a semi-empirical model which predicts these unknown quantities based on the method proposed by van Oss, Chaudhury, and Good (vOCG) in order to determine whether an arbitrary combination of solid and lubricant will repel a given impinging fluid. This model was validated against experiments performed in the present work as well as the literature, where an excellent predictive capability was demonstrated. From this validated model, a new framework for LIS design was

proposed, where we demonstrated that recently proposed guidelines in the literature exhibit a fundamental misunderstanding of LIS design. We used our newly proposed framework to design LIS on uncoated high-surface-energy solids, thereby eliminating the need for unreliable[175] low-surface-energy coatings. We went on to experimentally demonstrate repulsion of the lowest surface tension impinging fluid (butane, $\gamma \approx 13$ mN/m) ever reported using a LIS, which in this case was comprised of an uncoated high-surface-energy solid (silicon dioxide) with a fluorinated but highly polar lubricant (hexafluoroisopropanol).

5.2 SEMI-EMPIRICAL PREDICTIVE MODEL

LIS behaviour is governed by the interfacial interactions between the three condensed phases (solid, lubricant, and impinging fluid, with each other and with the surrounding environment) and by the geometry of the solid surface. These interfacial interactions and surface geometry can be used to predict whether a LIS will successfully repel the impinging fluid as discrete droplets. The geometry of the solid surface is described by the roughness, r, which represents the actual solid surface area divided by the projected area, and the solid fraction, φ, which represents the fraction of the solid which contacts the base of the droplet. Meanwhile, the interfacial interactions can be described at a high level by the surface energies of the three phases with the surrounding vapor and the either the contact angles or the spreading parameters of the three phases with each other.

The criteria which must be met for a functional LIS are shown schematically in Figure 17. In the ideal case, the impinging fluid forms a discrete droplet on the LIS and the lubricant remains trapped within the rough solid structured surface beneath the droplet. If criterion (I) is not met and the spreading parameter for the lubricant on the droplet is positive, the lubricant spontaneously spreads over and "cloaks" the droplet. The cloaked droplet retains most of the functionality of a non-cloaked droplet on the LIS (high mobility, etc.), but the cloaked state is still generally undesirable due to the removal of lubricant when droplets depart from the surface, depleting the lubricant over time. If criterion (II) is not met, the impinging fluid spreads indefinitely over the lubricant, resulting in formation of a film instead of discrete droplets and subsequent failure of the LIS. If criteria (III) and (IV) are not met, the lubricant does not spread within the rough structured solid surface during operation; in the absence of criterion (III), the lubricant does not infuse in the solid structures in the presence of the surrounding vapor, and in the absence of criterion (IV), the lubricant does not infuse in the solid structures in the presence of the impinging fluid, either of which result in failure of the LIS. If the left hand sides of the inequalities in

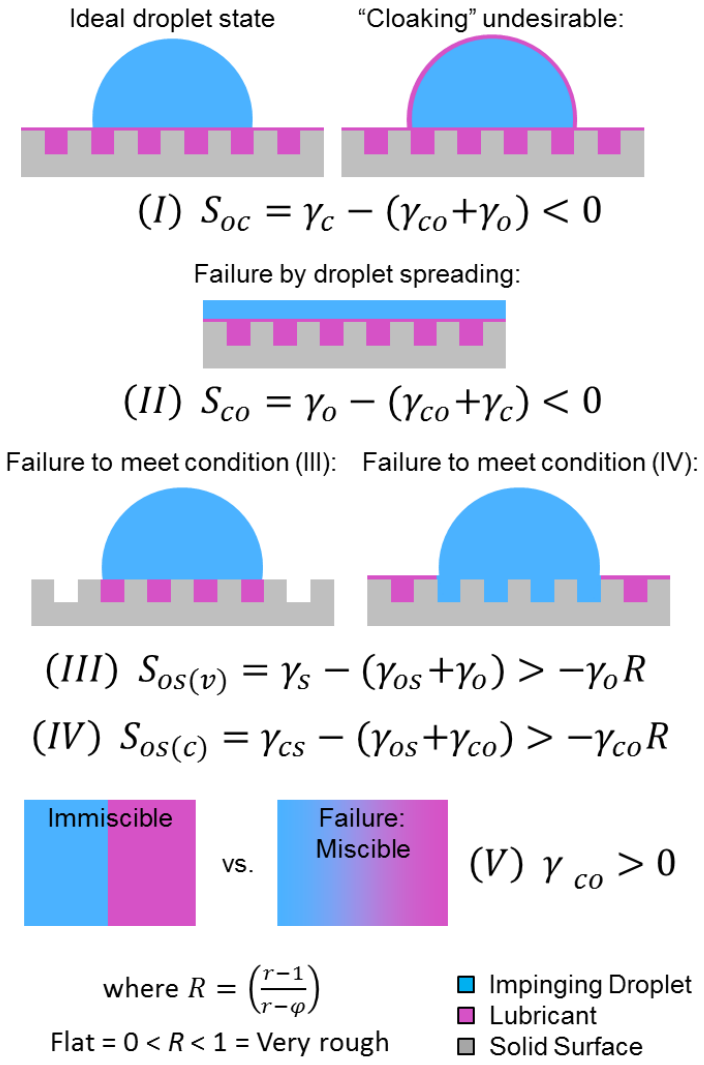

Figure 17. Surface-energy-based criteria for LIS design. The ideal droplet of impinging fluid on a LIS rests atop a combined lubricant-solid layer. If criterion (I) is not satisfied, the droplet will be "cloaked," or covered with a thin layer of lubricant, which may eventually deplete the surface of lubricant as droplets depart. The impinging fluid will spread over the LIS as a film if criterion (II) is not met. Criteria (III) and (IV) must be met to ensure that the lubricant remains infused in the rough solid. If $S_{os(v)}$ or $S_{os(c)}$ are greater than zero, the lubricant will cover the entire surface in the presence of the vapor or condensate, respectively; otherwise, if (III) or (IV) are still satisfied but $S_{os(v)}$ or $S_{os(c)}$ are less than zero, a fraction φ of the solid will contact the impinging fluid in the presence of the vapor or condensate, respectively. Miscibility of the impinging fluid and the lubricant is characterized by the interfacial tension between these two fluids, where if criterion (V) is not met it is energetically favorable for the two fluids to form an infinitely large interface (i.e., fully mutually dissolve). The geometric factor R combines the roughness r and the solid fraction φ.

criteria (III) or (IV) exceed zero, the lubricant fully covers the solid surface in the presence of the vapor or the impinging fluid, respectively, as opposed to leaving the tops of the rough solid structures exposed. The case where the structures are completely covered by lubricant results in significantly reduced contact angle hysteresis but is not necessary for a stable LIS.[178] Finally, if condition (V) is not met, the interface between the lubricant and the impinging fluid increases its surface area indefinitely to minimize energy, ultimately resulting in the miscibility of the two fluids – criterion (V) has not been expressed explicitly in the previous literature.

The interfacial energies between any two condensed phases in these criteria, namely γ_{co}, γ_{os}, and γ_{cs}, are not typically tabulated for the majority of interfacial interactions of interest and therefore have only been obtained experimentally for the phases of interest in prior work on LIS. Here, we unify the above energy-based criteria with a method to predict the unknown interfacial energies in order to gain new insight into LIS surface design and additionally reduce the time required to characterize a given combination of N materials from $O(N^3)$ to O(N) through a semi-empirical model (see supplementary information). We start with Fowkes' assumption that an interfacial energy can be divided into contributions from various intermolecular forces, e.g., dispersive, polar, metallic, etc., and then predict these components independently from properties of the interacting phases.[41,187] The dispersive (or London) forces are combined with induced dipole and permanent dipole forces and termed the Lifshitz-van Der Waals (LW) component of interfacial energy, which can be determined based on physical understanding with reasonable confidence from a geometric combining rule.[41,187] The polar component was initially treated in the same manner by Owens and Wendt (OW),[188] but this method is now considered obsolete and has been largely replaced by the superior method proposed by van Oss, Chaudhury, and Good (vOCG)[189-192] in which Lewis acid-base contributions to interfacial energy are considered (acid represented by superscript +, base represented by superscript –). The vOCG method outperforms the OW method most notably in cases were hydrogen bonding is involved, and is also considered more versatile than the commonly-used Neumann method; as such, the vOCG method is used here to predict the polar contribution to interfacial energy between condensed phases.[192-194] Metallic interactions are not considered here, but would need to be considered to account for interactions between phases such as mercury and metallic solids.

For any given phase, the total interfacial energy is found from the LW and acid-base components as shown in Equation (2), where the geometric combination of the vOCG acid-base terms yields the polar interaction. The interfacial tension between two phases is found from Equation (3), where each fluid's

LW and acid-base terms are considered. Note that when phases 1 and 2 have identical LW and acid-base terms (i.e., they are the same fluid) the interfacial energy recovered from Equation (3) is zero as expected.

$$\gamma_1^{total} = \gamma_1^{LW} + 2\sqrt{\gamma_1^+\gamma_1^-} \tag{2}$$

$$\gamma_{12}^{total} = \gamma_1^{LW} + \gamma_2^{LW} - 2\sqrt{\gamma_1^{LW}\gamma_2^{LW}} + 2\sqrt{\gamma_1^+\gamma_1^-} + 2\sqrt{\gamma_2^+\gamma_2^-} - 2\sqrt{\gamma_1^+\gamma_2^-} - 2\sqrt{\gamma_2^+\gamma_1^-} \tag{3}$$

Equation 2 is used to predict the three interfacial energies between condensed phases, γ_{co}, γ_{os}, and γ_{cs}, used in criteria (I) to (V) shown in Figure 17. The expanded forms of the inequalities of criteria (I) to (V) are presented in Equations (4) through (8):

$$\gamma_c^{LW} + 2\sqrt{\gamma_c^+\gamma_c^-} - \gamma_o^{LW} - 2\sqrt{\gamma_o^+\gamma_o^-} - \gamma_c^{LW} - \gamma_o^{LW} + 2\sqrt{\gamma_c^{LW}\gamma_o^{LW}} - 2\sqrt{\gamma_c^+\gamma_c^-} - 2\sqrt{\gamma_o^+\gamma_o^-} + 2\sqrt{\gamma_c^+\gamma_o^-} + 2\sqrt{\gamma_o^+\gamma_c^-} < 0 \tag{4}$$

$$\gamma_o^{LW} + 2\sqrt{\gamma_o^+\gamma_o^-} - \gamma_c^{LW} - 2\sqrt{\gamma_c^+\gamma_c^-} - \gamma_c^{LW} - \gamma_o^{LW} + 2\sqrt{\gamma_c^{LW}\gamma_o^{LW}} - 2\sqrt{\gamma_c^+\gamma_c^-} - 2\sqrt{\gamma_o^+\gamma_o^-} + 2\sqrt{\gamma_c^+\gamma_o^-} + 2\sqrt{\gamma_o^+\gamma_c^-} < 0 \tag{5}$$

$$\gamma_s^{LW} + 2\sqrt{\gamma_s^+\gamma_s^-} - \gamma_o^{LW} - \gamma_s^{LW} + 2\sqrt{\gamma_o^{LW}\gamma_s^{LW}} - 2\sqrt{\gamma_o^+\gamma_o^-} - 2\sqrt{\gamma_s^+\gamma_s^-} + 2\sqrt{\gamma_o^+\gamma_s^-} + 2\sqrt{\gamma_s^+\gamma_o^-} + (R-1)\left(\gamma_o^{LW} + 2\sqrt{\gamma_o^+\gamma_o^-}\right) > 0 \tag{6}$$

$$\gamma_c^{LW} + \gamma_s^{LW} - 2\sqrt{\gamma_c^{LW}\gamma_s^{LW}} + 2\sqrt{\gamma_c^+\gamma_c^-} + 2\sqrt{\gamma_s^+\gamma_s^-} - 2\sqrt{\gamma_c^+\gamma_s^-} - 2\sqrt{\gamma_s^+\gamma_c^-} - \gamma_o^{LW} - \gamma_s^{LW} + 2\sqrt{\gamma_o^{LW}\gamma_s^{LW}} - 2\sqrt{\gamma_o^+\gamma_o^-} - 2\sqrt{\gamma_s^+\gamma_s^-} + 2\sqrt{\gamma_o^+\gamma_s^-} + 2\sqrt{\gamma_s^+\gamma_o^-} + (R-1)\left(\gamma_c^{LW} + \gamma_o^{LW} - 2\sqrt{\gamma_c^{LW}\gamma_o^{LW}} + 2\sqrt{\gamma_c^+\gamma_c^-} + 2\sqrt{\gamma_o^+\gamma_o^-} - 2\sqrt{\gamma_c^+\gamma_o^-} - 2\sqrt{\gamma_o^+\gamma_c^-}\right) > 0 \tag{7}$$

$$\gamma_c^{LW} + \gamma_o^{LW} - 2\sqrt{\gamma_c^{LW}\gamma_o^{LW}} + 2\sqrt{\gamma_c^+\gamma_c^-} + 2\sqrt{\gamma_o^+\gamma_o^-} - 2\sqrt{\gamma_c^+\gamma_o^-} - 2\sqrt{\gamma_o^+\gamma_c^-} > 0 \tag{8}$$

These inequalities provide a great deal of insight into the design and functionality of LIS. An interesting example is the design of LIS to repel low surface tension fluids such as refrigerants or hydrocarbons, which are often nonpolar. In the case of a nonpolar impinging fluid ($\gamma_c^+ = \gamma_c^- = 0$), in order to avoid both cloaking (criterion I, Equation (4)) and spreading of the impinging fluid on the LIS (criterion II, Equation (5)), we find that the combined inequality in Equation (9) must be satisfied. Therefore, it is impossible to

meet both criteria I and II if the lubricant is also nonpolar; the lubricant must have some polar component of surface energy in order to avoid both cloaking and spreading of the impinging fluid.

$$\sqrt{\gamma_o^{LW}} + \frac{\sqrt{\gamma_o^+ \gamma_o^-}}{\sqrt{\gamma_o^{LW}}} > \sqrt{\gamma_c^{LW}} > \sqrt{\gamma_o^{LW}} \tag{9}$$

There are limitations to the vOCG method when used for the prediction of interfacial energies. Several specific concerns raised are that the base components are systematically greater than the acid components,[195] that experimentally determined surface energy components may depend on the set of fluids chosen for experiments,[195] and that the values of the components may sometimes take negative values.[190,195] In response to the first concern, the relative magnitudes of the acid and base terms are set by the choice of the components of water, which are typically equal to each other but may be chosen to make typical acid and base values for other fluids comparable as shown by Della Volpe and Siboni.[195,196] The second concern may be addressed by choosing appropriate test fluids when characterizing the surface energy components,[197] or by choosing many fluids.[198,199] The final concern is assuaged by noting that negative surface energy component values reported are often of a lesser magnitude than the error of the measurement.[195,200] Even with the concerns addressed, there may still be significant error in prediction of interfacial energy over a broad range of fluids as pointed out by Kwok[201] and Lee.[202-204] In addition, in the specific case of LIS, a subset of prior work has used ionic liquids as lubricants; unfortunately, not only is there a dearth of data on the acid-base components of these liquids,[205-207] but the vOCG method would have trouble even with suitable data for pure ionic liquids due to the extent to which ionic liquids and water are mutually soluble, with water changing surface tension by nearly 50% in the presence of certain ionic liquids; therefore, ionic liquids are not considered in this analysis.[179,194] With those criticisms in mind, there is a wealth of literature on prediction of interfacial energy prediction,[208-212] including data for the vOCG LW, acid, and base components for over 150 fluids and solids compiled in the supplementary information, and the consensus is that the vOCG method is the most versatile choice for a broad range of fluids.[193,194,196,200,213,214] Indeed, as demonstrated below, its predictive power is not only suitable for LIS, it also offers insights that commonly cited design guidelines have failed to capture.

5.3 RESULTS AND DISCUSSION

In order to test the validity of the proposed model, we performed experiments with several different combinations of impinging fluids and lubricants on a rough surface comprised of copper oxide (CuO) nanoblades fabricated on a copper tube substrate and subsequently functionalized with a low-surface-

energy perfluorinated monolayer coating of trichloro(1H,1H,2H,2H-perfluorooctyl)silane (TFTS). The geometric factor for the CuO surface was $R = 0.80$, indicating that the surface is very rough. Water was used as the impinging fluid on LIS with lubricants of Krytox GPL 101fluorinated oil, silicone oil (Shin Etsu 5 cSt), and ethanol on the functionalized CuO solid surface. With the Krytox GPL 101 fluorinated oil as a lubricant on the functionalized CuO surface, impinging fluids of toluene and pentane were also tested. The tests were performed in a sealed environmental chamber. The LIS was first prepared by adding lubricant to the surface and removing excess lubricant with a nitrogen gun, and then the chamber was sealed and impinging fluid was condensed onto the LIS, which was chilled by a flow of controlled-temperature chiller fluid within the tube and observed with a video camera (see Methods: Condensation Experiments). If discrete and mobile droplets were observed on the LIS exterior of the tube where the impinging fluid was condensing, the LIS configuration was deemed successful (see supplementary information). The experimental results were compared with the model prediction in Table 1, where all of the experiments performed in the present work were in agreement with the model prediction. Interestingly, the model predicted not only the failure in the case with water impinging on the LIS of ethanol on CuO, but also the failure mechanism: criterion (V) was not satisfied, indicating that water and ethanol are miscible, which was the reason for the failure.

We also validated the model against experimental results in the literature. Rykaczewski condensed water and low surface tension fluids on a LIS of Krytox 1506 oil infused in TFTS-coated silicon posts ($R = 0.76$) in a procedure similar to the present work.[163] This work found that most of the configurations showed successful LIS promotion of droplet formation, with the exception of three cases. In two of these cases, the condensate (ethanol, isopropanol) displaced the lubricant; the model predicted failure in these cases due to criterion (IV), where the strong polar interactions between the condensate and the TFTS coating on the solid surface resulted in displacement of the Krytox oil. In the third case, perfluorohexane spread over the LIS, which was also accurately captured as the failure mode by the model when criterion (II) was not met. Wong placed droplets onto a PTFE membrane (estimated $R = 0.82$) infused with Krytox GPL 100 oil;[162] in this study, all of the experiments were successful. Finally, Anand condensed water onto a LIS of silicone oil (viscosities of 10 and 1,000 cSt) infused in silicon pillars ($R = 0.57$) coated with octadecyltrichlorosilane (OTS),[177] where again all of the experiments were successful.

Table 2. LIS experiments in the present work and other literature compared to the model prediction. The model predicted the experimental results with excellent accuracy, and also predicted the correct failure mode in the failed experimental cases.

Droplet	Lubricant	Coating/Solid	Experiment	Prediction	Ref.
Water	Krytox 1506	TFTS on Si Pillars	✔	✔	[163]
Toluene	Krytox 1506	TFTS on Si Pillars	✔	✔	"
Ethanol	Krytox 1506	TFTS on Si Pillars	*X*	*X*	"
Octane	Krytox 1506	TFTS on Si Pillars	✔	✔	"
Hexane	Krytox 1506	TFTS on Si Pillars	✔	✔	"
Pentane	Krytox 1506	TFTS on Si Pillars	✔	✔	"
Perfluoro-hexane	Krytox 1506	TFTS on Si Pillars	*X*	*X*	"
Water	Krytox GPL 100	PTFE Membrane	✔	✔	[162]
Hexane	Krytox GPL 100	PTFE Membrane	✔	✔	"
Pentane	Krytox GPL 100	PTFE Membrane	✔	✔	"
Water	10 cSt Si Oil	OTS on Si Pillars	✔	✔	[177]
Water	1000 cSt Si Oil	OTS on Si Pillars	✔	✔	"
Water	Krytox GPL 101	TFTS on CuO Nanoblades	✔	✔	*
Water	5 cSt Si Oil	TFTS on CuO Nanoblades	✔	✔	*
Water	Ethanol	TFTS on CuO Nanoblades	*X*	*X*	*
Toluene	Krytox GPL 101	TFTS on CuO Nanoblades	✔	✔	*
Pentane	Krytox GPL 101	TFTS on CuO Nanoblades	✔	✔	*

*present work

Through comparison of the model with 18 total experimental cases, 5 from the present study and 13 from 3 studies in the literature, we found that the model had predicted success or failure of the LIS with 100% accuracy. Of equal importance, in each of the failure cases considered, the model revealed why the failure occurred. With this in mind, we proceeded to use the model to explore the validity of some common guidelines proposed by seminal works in the LIS field. First, we address the concept that the solid must have a low surface energy.[177] Contrary to this statement, our model indicates that the solid need not have a low surface energy; in fact, the opposite case appears to be more desirable. Figure 18

shows a parametric sweep of the three surface energy components (LW, acid, and base) of the lubricant for two different solids: a low surface energy PTFE-coated solid in Figure 18(a) and a high surface energy SiO_2-coated solid in Figure 18(b), with the goal of repelling a nonpolar impinging fluid with surface tension 17 mN/m. The range of feasible lubricants for the SiO_2 solid surface is clearly much more expansive, including (1) providing possible solutions for γ_o^{LW} = 8 mN/m when the PTFE surface provides none and (2) providing a much larger margin of error to avoid droplet cloaking in all cases by introducing acid-base components to the lubricant and entering the large non-cloaking regions (in black). (Note that the model indicates that a nonpolar fluid with surface tension 16 mN/m is indicated as a suitable lubricant for an impinging nonpolar fluid with surface tension 17 mN/m, which raises concerns about the accuracy of the miscibility criterion (V); the effect of a more conservative miscibility criterion is discussed in the supplementary information.)

We experimentally tested a LIS with a high surface energy solid by using plasma-cleaned SiO_2-coated silicon pillars. As shown in Table 3, the model predicted that methanol could be a suitable lubricant for the impinging fluids diiodomethane and heptane. This is primarily due to the strong Lewis acid-base polar interaction between methanol and SiO_2 which helps to satisfy criteria (III) and (IV). Figure 19(a and c) shows the experimental results in these two cases for a droplet impinging on an inclined surface of SiO_2 pillars infused with methanol (see Methods, Droplet Impingement Experiments). Highly-mobile discrete droplets of both diiodomethane and heptane form on the LIS of methanol in SiO_2 pillars, indicating a successful LIS in agreement with the model prediction and demonstrating a LIS which employs a high surface energy solid material for the first time. This is particularly useful for future LIS design because thin, low-surface-energy coatings often lack durability;[175] we demonstrate here that these coatings are not necessary for LIS.

Even more intriguing is the consideration of whether LIS can be used to promote droplet formation with finite contact angles of impinging fluids with surface tensions below the critical surface energy of the solid contrary to common knowledge.[163] Certainly droplets will not form for a fluid impinging directly onto a solid if the fluid has a surface tension lower than the solid's relevant critical surface energy by definition. However, our model predicts that a suitably-designed LIS can promote formation of droplets with finite wetting angle even when the impinging fluid has a surface energy lower than that of the solid surface. Specifically, we have chosen the example of SiO_2 pillars with methanol as the lubricating fluid and heptane as the impinging fluid, where the lowest reported critical surface tension of SiO_2 in literature is 27.7 mN/m and the surface tension of heptane is 20.1 mN/m. In this case, the model predicts that all of

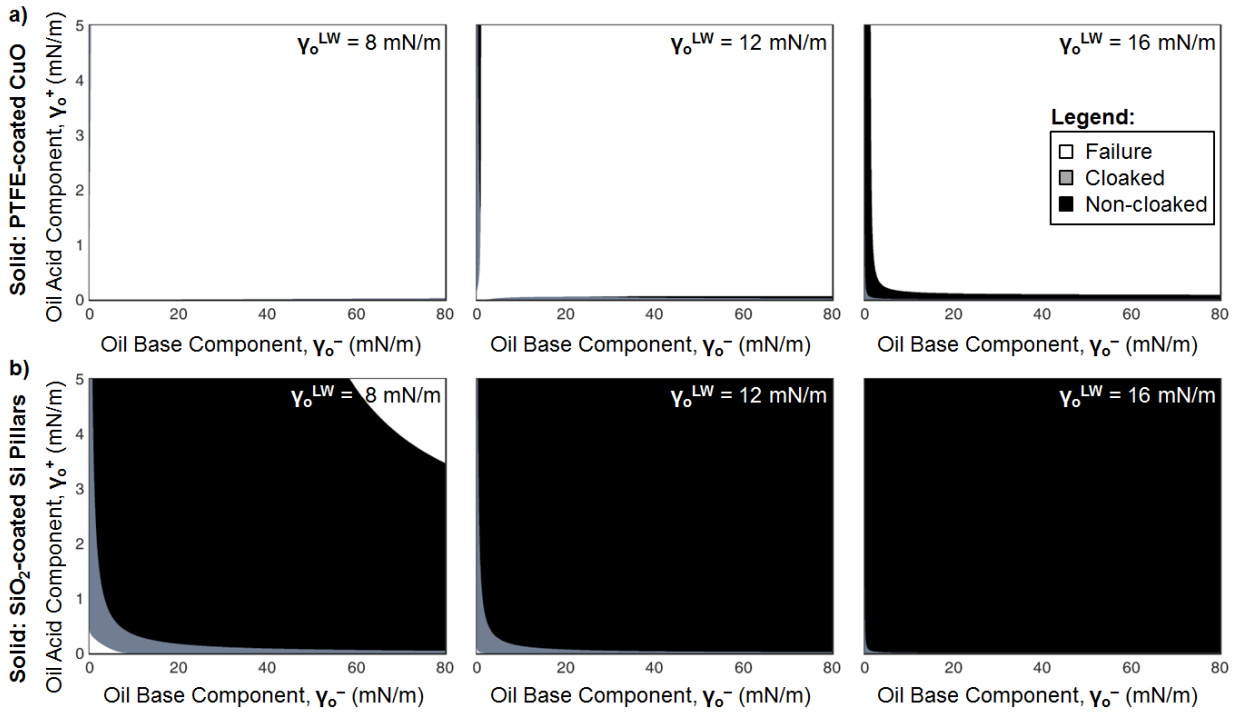

Figure 18. Parametric sweep of γ_o^{LW}, γ_o^+, and γ_o^- for two different solid surfaces. (a)A low-surface-energy surface of PTFE coated onto CuO nanoblades (R = 0.80) has no solution when γ_o^{LW} = 8, and the solution domain is limited to nonpolar fluids for higher values of γ_o^{LW}. (b) A high-surface-energy structured surface of SiO_2 pillars (R = 0.78) allows a much larger range of potential lubricants, including a wide range of potential fluids which would allow non-cloaked droplet formation (black region).

the criteria (I) through (V) will be satisfied. Criteria (III) and (IV) are once again satisfied due to the strong polar affinity between methanol and SiO2. Perhaps more interestingly, we see that the model predicts that Equation 8 will be satisfied to avoid both droplet cloaking and spreading of the nonpolar impinging fluid – this is possible due to methanol having a lower LW component of surface energy than heptane while also having a sufficiently large polar component of surface energy. The results of the experiment with this LIS configuration are shown in Figure 19(c), where discrete and mobile droplets of heptane form on the methanol/SiO_2 LIS in agreement with the model prediction. This demonstration indicates that LIS enables formation of discrete droplets on a solid surface with a critical surface energy higher than that of the impinging droplets, so long as an appropriate lubricating fluid is chosen.

Table 3. LIS combinations counterintuitive to conventional design guidelines. The impinging droplet, lubricant, and solid/coating are described along with their relevant surface energy components. The model prediction for criteria (I) through (V) are shown to the right, and the experiment success or failure is indicated.

Droplet	Lubricant	Solid/Coating	I	II	III	IV	V	Exp.	Fig.
Diiodomethane (γ = 50.8 mN/m) (γ^{LW} = 50.8 mN/m) (γ^{+} = 0.0 mN/m) (γ^{-} = 0.0 mN/m)	Methanol (γ = 22.5 mN/m) (γ^{LW} = 18.2 mN/m) (γ^{+} = 0.1 mN/m) (γ^{-} = 77.0 mN/m)	Bare SiO_2Pillars (γ = 59.8 mN/m) (γ^{LW} = 42.0 mN/m) (γ^{+} = 2.0 mN/m) (γ^{-} = 40.2 mN/m)	*X*	✔	✔	✔	✔	✔	19(a)
Methanol (γ = 22.5 mN/m) (γ^{LW} = 18.2 mN/m) (γ^{+} = 0.1 mN/m) (γ^{-} = 77.0 mN/m)	Diiodomethane (γ = 50.8 mN/n) (γ^{LW} = 50.8 mN/m) (γ^{+} = 0.0 mN/m) (γ^{-} = 0.0 mN/m)	Bare SiO_2Pillars (γ = 59.8 mN/m) (γ^{LW} = 42.0 mN/m) (γ^{+} = 2.0 mN/m) (γ^{-} = 40.2 mN/m)	✔	*X*	✔	*X*	✔	*X*	19(b)
Heptane (γ = 20.1 mN/m) (γ^{LW} = 20.1 mN/m) (γ^{+} = 0.0 mN/m) (γ^{-} = 0.0 mN/m)	Methanol (γ = 22.5 mN/n) (γ^{LW} = 18.2 mN/m) (γ^{+} = 0.1 mN/m) (γ^{-} = 77.0 mN/m)	Bare SiO_2Pillars (γ = 59.8 mN/m) (γ^{LW} = 42.0 mN/m) (γ^{+} = 2.0 mN/m) (γ^{-} = 40.2 mN/m)	✔	✔	✔	✔	✔	✔	19(c)
Butane (γ = 12.5 mN/m) (γ^{LW} = 12.5 mN/m) (γ^{+} = 0.0 mN/m) (γ^{-} = 0.0 mN/m)	Hexafluoro-IPA (γ = 14.7 mN/m) (γ^{LW} = 12.5 mN/m) (γ^{+} = 0.0 mN/m) (γ^{-} = 0.0 mN/m)	Bare SiO_2Pillars (γ = 59.8 mN/m) (γ^{LW} = 42.0 mN/m) (γ^{+} = 2.0 mN/m) (γ^{-} = 40.2 mN/m)	✔	✔	✔	✔	✔	✔	20

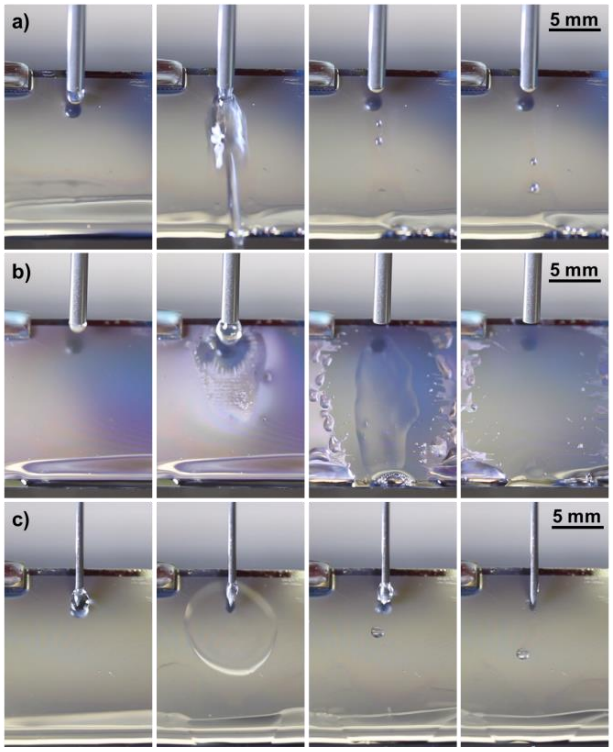

Figure 19. Experimental results from droplet impingement tests for counterintuitive LIS designs. (a) Diiodomethane is dropped onto a LIS of methanol infused in SiO_2 pillars. Discrete, mobile droplets of diiodomethane form on the LIS. (b) Methanol is dropped onto a LIS of diiodomethane infused in SiO_2 pillars. The methanol forces the diiodomethane lubricant out of the SiO_2 pillars as predicted by the model. (c) Heptane is dropped onto a LIS of methanol infused in SiO_2 pillars. Discrete droplets of heptane form and slide down the LIS even though the surface tension of heptane is lower than the critical surface energy of SiO_2, indicating that LIS allows droplet formation on a solid with a critical surface energy higher than the impinging fluid so long as an appropriate lubricant is chosen.

We also considered whether the lubricating fluid should have a surface tension similar to that of the solid surface.[215] We already know from the experiment shown in Figure 19(a) that methanol is a suitable lubricant for the SiO_2 solid surface despite having an overall surface energy of less than 40% that of SiO_2. We considered the reverse case, where methanol was taken as the impinging fluid and diiodomethane, with a better "matching" surface energy 85% that of SiO_2, was taken as the lubricant. In this case, the model predicted that the strong polar affinity between the methanol and the SiO_2 would not allow criterion (IV) to be satisfied and would consequently result in forced dewetting of the diiodomethane from the SiO_2 pillars even though the diiodomethane has a surface energy much more closely matched to that of the SiO_2. The experimental result from the droplet impingement test is shown in Figure 19(b), and the diiodomethane is indeed forced out of the SiO_2 pillars by the methanol, demonstrating that the overall surface energies of the lubricant and the solid surface need not necessarily match.

Finally, we took advantage of the potential for a strong polar interaction between the lubricant and a high-surface-energy solid to design a LIS to repel extremely low surface tension impinging fluids. Previously, multiple reports have indicated that LIS are able to repel pentane ($\gamma \approx 17$ mN/m),[162,163] but lower surface tension fluids such as perfluorohexane could not be repelled. We used the same SiO_2 pillared solid surface as in the experiments shown in Figure 19, but we chose hexafluoroisopropanol (6F-IPA) as the lubricant in order to maintain the strong polar interaction through the presence of its –OH group while simultaneously exhibiting a significantly lower LW component of surface energy compared to methanol due to the fluorination. The model predicted that this surface would be able to repel nonpolar impinging fluids with surface tensions as low as ≈ 11 mN/m; we performed an experiment with butane ($\gamma \approx 13$ mN/m) as the impinging fluid. We modified the experimental setup by placing it inside of a glass vial to accommodate the above-atmospheric vapor pressure (≈ 2.5 atm) at standard temperature, which resulted in a limited field of view. We first performed a control experiment during which we sprayed droplets of butane onto a flat plasma-cleaned SiO_2 surface and found that butane droplets impinging onto the flat SiO_2 surface spread completely, as expected due to the surface tension of butane being lower than the critical surface energy of SiO_2. We then sprayed butane droplets onto the proposed LIS of 6F-IPA infused into the SiO_2 pillars, with the results shown in Figure 20. Discrete droplets form on the surface, and the droplets exhibit a high degree of mobility as well as typical droplet behaviour such as multiple sweeping and coalescence events.

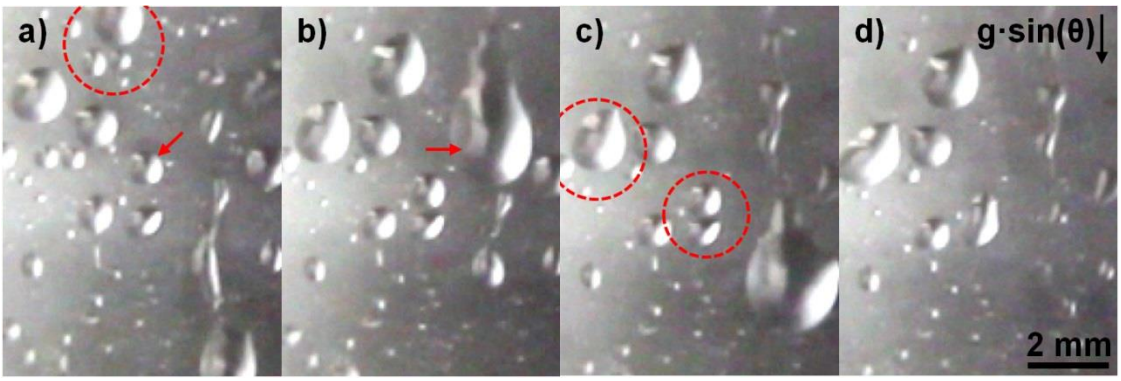

Figure 20. Behaviour of liquid butane impinging on a LIS of 6F-IPA infused in silicon micropillars. The experiment was performed inside of a glass vial at elevated pressure. Photos (a) through (d) are time lapse images of droplets moving on the LIS after being sprayed on the surface. The dashed red circles indicate when droplet coalescence events are about to occur, and the red arrows indicate droplets sliding on the surface, which occur at approximately the capillary length (1.4 mm) in this case. Droplets of butane deposited onto a flat SiO_2 surface in the same experimental setup immediately spread over the surface.

5.4 SUMMARY

While the design of LIS has been explored in terms of surface energies which must be determined empirically, we developed a model which uses a prediction of these surface energies to determine whether an arbitrary combination of solid and lubricant will repel a given impinging fluid. This model was validated against experiments performed in the present work as well as the literature and subsequently used to develop a new framework for LIS design, where we demonstrated that commonly cited guidelines in the literature are often misleading or incorrect. We went on to design LIS on uncoated high-surface-energy solids, eliminating the need for unreliable low-surface-energy coatings. The vOCG-based approach to LIS design using high-surface-energy solids and polar lubricants resulted in repulsion of discrete droplets of the lowest surface tension fluid recorded to date (butane, $\gamma \approx 13$ mN/m). This demonstration of LIS repelling extremely low-surface-tension fluids is promising for applications in thermal management and hydrocarbon processing. More broadly, the insights gained from the vOCG framework will promote new developments in LIS design, paving the way for new technology in biological science, lab-on-a-chip, thermofluidics, and beyond.

5.5 METHODS

Surface Fabrication – To create the CuO nanostructures, commercially available oxygen-free Cu tubes were used (99.9 % purity) with outer diameters, D_{OD} = 6.35 mm, inner diameters, D_{ID} = 3.56 mm, and lengths, L = 131 mm, as the test samples for the condensation experiments. Each Cu tube was cleaned in an ultrasonic bath with acetone for 10 minutes and rinsed with ethanol, isopropanol, and de-ionized (DI) water. The tubes were then dipped into a 2.0 M hydrochloric acid solution for 10 minutes to remove the native oxide film on the surface, then triple-rinsed with DI water and dried with clean nitrogen gas. Nanostructured CuO films were formed by immersing the cleaned tubes (with ends capped) into a hot (96 ± 3 °C) alkaline solution composed of $NaClO_2$, NaOH, $Na_3PO_4 \bullet 12H_2O$, and DI water (3.75 : 5 : 10 : 100 wt.%).[164,169,170] During the oxidation process, a thin (≈300 nm) Cu_2O layer was formed that then re-oxidized to form sharp, knife-like CuO oxide structures with heights of $h \approx 1$ μm, solid fraction $\varphi \approx 0.038$ and roughness factor $r \approx 4$ (see supplementary information).

Silicon micropillar surfaces (Fig. 4d) with diameters of d = 7 μm, heights of h = 20 μm, and center-to-center spacings of l = 2 μm (solid fraction $\varphi = \pi d^2/4l^2 = 0.38$ and roughness factor $r = 1 + \pi dh/l^2 = 3.20$) were fabricated using projection lithography and deep reactive ion etching.

Surface Functionalization – trichloro(1H,1H,2H,2H-perfluorooctyl)silane (TFTS) (Sigma-Aldrich) was deposited from the vapor phase. Prior to silane deposition, each tube was oxygen plasma cleaned for 2 hours to remove organic contaminants on the surface. Once clean, the tube samples were immediately placed in a vacuum desiccator (06514-10, Cole Parmer) with a small amount of liquid silane. The desiccator was evacuated by a roughing pump for 2 minutes to a minimum pressure of ≈ 2 kPa. A valve was then closed to isolate the pump from the desiccator and the sample was held in vacuum (≈ 2 kPa) for another 10 minutes. The functionalized tubes were then rinsed in ethanol and DI water and dried in a clean nitrogen stream. The coating had a typical advancing angle of $\theta_a \approx 120^\circ$ when measured on a smooth reference surface and typical advancing/receding angles of $\theta_a/\theta_r \approx 171/167 \pm 3^\circ$ when measured on the nanostructured CuO surface.

Condensation Experiments – Condensation experiments were performed inside of a controlled environmental chamber. TFTS-functionalized CuO coatings were applied to the exterior surface of copper condenser tubes. The TFTS-coated CuO was infused with lubricant by first placing a few droplets of lubricant onto the surface and allowing them to spread completely, then using a nitrogen stream (99.9%, Airgas) to shear off excess lubricant. Following the addition of lubricant, the chamber was sealed and noncondensable gases were evacuated with a vacuum pump (except in the case of the ethanol lubricant, where the vacuum pump was not used so as not to evaporate the ethanol). Pure vapor of the impinging condensate was then introduced as the tube sample was cooled from within with a chiller loop set to 15 °C. The behaviour of the condensate was imaged from a viewport during condensation.

Droplet Impingement Experiments – Droplet impingement experiments were performed with the LIS held at ≈ 45° from horizontal inside of a fume hood. Excess lubricant was added to the base of the dry, plasma cleaned[114] SiO_2 pillar structured surface and allowed to wick into the SiO_2 pillars until they were filled with lubricant. The droplets of the impinging fluid were then dispensed from a syringe with a stainless steel needle. Images were taken at an angle of ≈ 0° from horizontal with a camera outside of the hood. For the experiment with butane as the impinging fluid, in order to prevent rapid evaporation of butane, the LIS was placed inside of a glass vial, infused with the 6F-IPA, then a small amount of butane was placed at the bottom of the vial and the vial was sealed and allowed to reach saturation conditions. Butane droplets were then introduced through a port at the top of the vial.

Pendant Drop Measurements – The surface energy components were determined for Krytox oil using the pendant drop method to characterize the interfacial tension of Krytox oil with multiple test liquids including water, ethylene glycol, glycerol, diiodomethane, 1-bromonapthalene, chloroform, and

formamide. The pendant drop measurement system consisted of a collimated light source (Thorlabs 6500 K, 440 mW Collimated LED) illuminating the droplet and aligned with a telecentric lens (Edmund 0.25X SilverTL) attached to a camera (PointGrey CM3-U3-13Y3C) capturing images. The droplets were dispensed with a Harvard Apparatus syringe pump through stainless steel needles, and when interfacial tension between two fluids was measured, the second fluid was contained inside of a glass cuvette. Glass cuvettes were cleaned thoroughly with Alconox followed by progressive solvent rinses in acetone, methanol, ethanol, isopropanol, and finally 99.99% pure DI water, and then nitrogen stream drying (99.9%, Airgas). Interfacial tensions were characterized from images using a plugin for ImageJ.[216] The surface energy components were determined from a plane fit to the data based on the vOCG equations, detailed in the supplementary information.

Chapter 6

6. Perspectives and Future Work

State-of-the-art techniques to promote dropwise condensation rely on functional hydrophobic coatings, which are often not robust and therefore undesirable for industrial implementation. Furthermore, low surface tension condensates pose a unique challenge since they often form a film, even on hydrophobic coatings. In this thesis, we addressed both of these concerns by first exploring robust rare earth oxide (REO) and graphene coatings for dropwise water condensation (Chapters 2 and 3), and then implementing lubricant infused surface (LIS) coatings to promote dropwise condensation of low surface tension fluids, including development of a model to design LIS (Chapters 5 and 6). Perspectives on the unique challenges of this work as well as future directions are presented here.

6.1 RARE EARTH OXIDE COATINGS

The recent discovery of robust rare earth oxide (REO) hydrophobicity has generated interest for dropwise condensation applications; however, prior to our work, the mechanism of REO hydrophobicity had been unclear. We demonstrated through careful experiments and modeling that REO hydrophobicity occurs due to the same hydrocarbon adsorption mechanism seen previously on noble metals, where REOs are hydrophilic when clean and become hydrophobic after extended exposure to air; this has been confirmed by subsequent work.[183,184,217] This study provided insight into how REOs can be used to promote stable dropwise condensation, which is important for the development of enhanced phase change surfaces.

The potential of REOs as functional surface coatings for condensers due to their hydrophobicity after hydrocarbon adsorption is promising, but also raises concerns. The large contact angle hysteresis of the REO surfaces studied here (~60° – 70°), and shown previously,[51] will act to increase the size of departing droplets, which negatively impacts heat transfer.[21] Another challenge is the thermal expansion coefficient mismatch between REOs (4 – 10 μm/m-K) and many industrial condenser metals (10 – 25 μm/m-K), which could result in fracturing of thin and brittle REO coatings due to temperature fluctuations.[218,219] However, the relatively low cost and moderate thermal conductivities of REOs (2.4 – 13.3 W/m-K, see supplementary information) offer a potentially unique advantage over traditional promoter coatings. Layers of hydrophobic polymers (PTFE) have been shown to give excellent dropwise condensation behavior but have only been found to be sufficiently durable when the thickness (δ) of the low-

conductivity polymer (k_p ~ 0.2 W/m·K) layer is so large (δ_p ≈ 20 μm) as to offset the advantage of dropwise condensation.[18] The larger coating thickness is typically required in order to increase adhesion to the metal substrate and enhance resistance to oxidation and moisture. Gold coatings have been shown to give excellent dropwise condensation but have only been found to be sufficiently durable (≈5.7 years of operating time) when the thickness of the gold is so large (≈50 μm) as to make the approach economically unfeasible.[220] On the other hand, REOs strike a balance between the two previous approaches in terms of cost and thermal conductivity. The moderate thermal conductivity of REOs allows for a ~25*x* thicker coating than conventional polymer layers while maintaining a comparable thermal resistance with the added benefit of potentially greater adhesion and durability.[51] Furthermore, the reduced cost of REOs compared to gold coatings makes their application to industrial materials more economically feasible.[117] In the future, more rigorous calculations of the expected condensation heat transfer are needed based on existing high fidelity models in the literature.[21,25,122,221]

6.2 GRAPHENE COATINGS

We demonstrated the effectiveness of ultra-thin scalable chemical vapor deposited (CVD) graphene coatings to promote dropwise condensation while offering robust chemical stability and maintaining low thermal resistance. Heat transfer enhancements of 4*x* compared to filmwise condensation were measured, and the robustness of these CVD coatings was superior to typical hydrophobic monolayer coatings. Our results indicated that graphene is a promising surface coating to promote dropwise condensation of water in industrial conditions, with the potential for scalable application *via* CVD.

While graphene offers a robust coating material to promote dropwise condensation on industrial metals, it is not a likely candidate to induce superhydrophobic behavior on micro- and nanostructured materials due to its relatively low advancing and receding contact angles compared to fluoropolymer coatings typically used for this application. While this eliminates the ability of graphene-coated surfaces to promote jumping droplet condensation,[90,133-135] the improvement in heat transfer coefficient of 4*x* provided by dropwise-promoting graphene coatings compared to filmwise condensation outweighs the marginal additional increase of 30-40% gained by jumping droplet condensation compared to dropwise condensation. Another potential limitation of these graphene coatings is their inability to induce dropwise condensation in systems which use low-surface-tension working fluids such as pentane; these fluids are expected to exhibit low contact angles and spread on graphene-coated surfaces, resulting in filmwise condensation. However, lubricant infused surfaces (described in Chapters 4 and 5) offer a promising alternative.

Future work should be directed towards longer-term study of the robustness of graphene coatings under typical condenser conditions (the duration of the present study was 2 weeks). A demonstration of graphene robustness on the order of years is perhaps the best method to enable adoption of these coatings in real-world applications. In addition, the scalable nature of graphene CVD should be leveraged for demonstration of the application of graphene coatings at the industrial scale.

6.3 LUBRICANT INFUSED SURFACES

Recent work has shown that lubricant infused surfaces (LIS) can promote discrete droplet formation of hydrocarbons as opposed to a fluid film; we confirmed the effectiveness of LIS in promoting dropwise condensation here by providing the first experimental measurement of heat transfer performance during hydrocarbon condensation on a LIS, which enhanced heat transfer by $\approx 5x$ compared to an uncoated surface. We also explored improvement through removal of noncondensable gases and addressed a failure mechanism whereby shedding droplets deplete the lubricant over time. We developed a model which uses a prediction of these surface energies to determine whether an arbitrary combination of solid and lubricant will repel a given impinging fluid. This model was validated against experiments performed in the present work as well as the literature and subsequently used to develop a new framework for LIS design, where we demonstrated that commonly cited guidelines in the literature are often misleading or incorrect. We went on to design LIS on uncoated high-surface-energy solids, thereby eliminating the need for unreliable low-surface-energy coatings, and experimentally demonstrated repulsion of the lowest surface tension impinging fluid (butane, $\gamma \approx 13$ mN/m) reported to date on a LIS.

LIS may prove more effective than flat coatings at enhancing low surface tension fluid condensation heat transfer, but failure by depletion of the lubricant remains a critical concern. The lubricant can be depleted by departure of cloaked droplets, or, as observed in the present work, the lubricant can be depleted even in the absence of droplet cloaking due to shearing by sliding droplets. A potential solution to lubricant shearing could be the addition of barriers for lubricant flow as proposed by Wexler et al. in the context of fluid flow past a LIS,[147,180] or alternatively a suitable design of the solid structures on the surfaces to tune the capillary pressure and permeability governing lubricant return after shearing, which could draw from concepts proposed in literature on evaporation from wicking materials.[222,223] If justifiable in a given application, the lubricant could be replenished periodically as well to overcome the problem.

The importance of NCG in condensation was also demonstrated in the present work, where less than 10% NCG was shown to eliminate the gain in performance obtained from promotion of dropwise

condensation. This confirms previous results indicating the importance of even low levels of NCG on condensation performance.[126,174] Future experiments in the field of condensation should be carefully conducted in pure vapor to allow direct comparison between studies unless the target application requires NCG, as in fog harvesting for example.[156]

With regard to the capability of the vOCG-based modelling of LIS, a subset of prior experimental work has used ionic liquids as lubricants. Unfortunately, not only is there a dearth of data on the Lewis acid-base components of these liquids,[205-207] but the vOCG method would have trouble even with suitable data for pure ionic liquids due to the extent to which ionic liquids and water are mutually soluble, with water changing surface tension by nearly 50% in the presence of certain ionic liquids; therefore, ionic liquids are not considered in this analysis.[179,194] Future work should attempt to incorporate the effects of fluid co-solubility on surface tension to improve the range of cases for which the vOCG-based model has reliable predictive power.

Even with these shortcomings in mind, this demonstration of LIS repelling extremely low-surface-tension fluids is promising for applications in thermal management and hydrocarbon processing. More broadly, the insights gained from the vOCG-based modelling framework will enable new developments in LIS design, paving the way for new technology in biological science, lab-on-a-chip, thermofluidics, and beyond.

7. Bibliography

1 Parker, A. R. & Lawrence, C. R. Water capture by a desert beetle. *Nature* **414**, 33-34, doi:Doi 10.1038/35102108 (2001).

2 Mockenhaupt, B., Ensikat, H. J., Spaeth, M. & Barthlott, W. Superhydrophobicity of Biological and Technical Surfaces under Moisture Condensation: Stability in Relation to Surface Structure. *Langmuir* **24**, 13591-13597, doi:Doi 10.1021/La802351h (2008).

3 Bhushan, B. Biomimetics: lessons from nature - an overview. *Philos T R Soc A* **367**, 1445-1486, doi:DOI 10.1098/rsta.2009.0011 (2009).

4 Zheng, Y. M. *et al.* Directional water collection on wetted spider silk. *Nature* **463**, 640-643, doi:Doi 10.1038/Nature08729 (2010).

5 Beer, J. M. High efficiency electric power generation: The environmental role. *Prog Energ Combust* **33**, 107-134, doi:DOI 10.1016/j.pecs.2006.08.002 (2007).

6 Peters, T. B. *et al.* Design of an Integrated Loop Heat Pipe Air-Cooled Heat Exchanger for High Performance Electronics. *Ieee T Comp Pack Man* **2**, 1637-1648, doi:Doi 10.1109/Tcpmt.2012.2207902 (2012).

7 Bierman, D. *Where Solar Thermal Meets Photovoltaic for High-Efficiency Power Conversion* SM thesis, Massachusetts Institute of Technology, (2014).

8 Humplik, T. *et al.* Nanostructured materials for water desalination. *Nanotechnology* **22**, doi:Artn 292001
Doi 10.1088/0957-4484/22/29/292001 (2011).

9 Khawaji, A. D., Kutubkhanah, I. K. & Wie, J. M. Advances in seawater desalination technologies. *Desalination* **221**, 47-69, doi:DOI 10.1016/j.desal.2007.01.067 (2008).

10 Perez-Lombard, L., Ortiz, J. & Pout, C. A review on buildings energy consumption information. *Energ Buildings* **40**, 394-398, doi:DOI 10.1016/j.enbuild.2007.03.007 (2008).

11 Wiser, W. H. *Energy resources: occurrence, production, conversion, use*. (Springer, 2000).

12 Li, B. Z. & Yao, R. M. Urbanisation and its impact on building energy consumption and efficiency in China. *Renew Energ* **34**, 1994-1998, doi:DOI 10.1016/j.renene.2009.02.015 (2009).

13 von Elsner, B. *et al.* Review of structural and functional characteristics of greenhouses in European Union countries: Part I, Design requirements. *J Agr Eng Res* **75**, 1-16, doi:DOI 10.1006/jaer.1999.0502 (2000).

14 Kaschiev, D. *Nucleation: Basic Theory With Applications*. (Butterworth Heinemann, 2000).

15 Nusselt, W. The surface condensation of water vapour. *Z Ver Dtsch Ing* **60**, 541-546 (1916).

16 Schmidt, E., Schurig, W. & Sellschopp, W. Condensation of water vapour in film- and drop form. *Z Ver Dtsch Ing* **74**, 544-544 (1930).

17 Das, A. K., Kilty, H. P., Marto, P. J., Andeen, G. B. & Kumar, A. The use of an organic self-assembled monolayer coating to promote dropwise condensation of steam on horizontal tubes. *J Heat Trans-T Asme* **122**, 278-286, doi:Doi 10.1115/1.521465 (2000).

18 Marto, P. J., Looney, D. J., Rose, J. W. & Wanniarachchi, A. S. Evaluation of Organic Coatings for the Promotion of Dropwise Condensation of Steam. *Int J Heat Mass Tran* **29**, 1109-1117, doi:Doi 10.1016/0017-9310(86)90142-0 (1986).

19 Vemuri, S. & Kim, K. J. An experimental and theoretical study on the concept of dropwise condensation. *Int J Heat Mass Tran* **49**, 649-657, doi:DOI 10.1016/j.ijheatmasstransfer.2005.08.016 (2006).

20 Vemuri, S., Kim, K. J., Wood, B. D., Govindaraju, S. & Bell, T. W. Long term testing for dropwise condensation using self-assembled monolayer coatings of n-octadecyl mercaptan. *Appl Therm Eng* **26**, 421-429, doi:DOI 10.1016/j.applthermaleng.2005.05.022 (2006).

21 Rose, J. W. Dropwise condensation theory and experiment: a review. *P I Mech Eng a-J Pow* **216**, 115-128 (2002).
22 Sikarwar, B. S., Khandekar, S., Agrawal, S., Kumar, S. & Muralidhar, K. Dropwise Condensation Studies on Multiple Scales. *Heat Transfer Eng* **33**, 301-341, doi:Doi 10.1080/01457632.2012.611463 (2012).
23 Miljkovic, N., Enright, R. & Wang, E. N. Effect of Droplet Morphology on Growth Dynamics and Heat Transfer during Condensation on Superhydrophobic Nanostructured Surfaces. *Acs Nano* **6**, 1776–1785 (2012).
24 Xiao, R., Miljkovic, N., Enright, R. & Wang, E. N. Immersion Condensation on Oil-Infused Heterogeneous Surfaces for Enhanced Heat Transfer. *Sci Rep-Uk* **3**, doi:Artn 1988
Doi 10.1038/Srep01988 (2013).
25 Kim, S. & Kim, K. J. Dropwise Condensation Modeling Suitable for Superhydrophobic Surfaces. *Journal of Heat Transfer* **133**, 081502-081501 - 081502-081507 (2011).
26 Love, J. C., Estroff, L. A., Kriebel, J. K., Nuzzo, R. G. & Whitesides, G. M. Self-assembled monolayers of thiolates on metals as a form of nanotechnology. *Chem Rev* **105**, 1103-1169, doi:Doi 10.1021/Cr0300789 (2005).
27 Chandekar, A., Sengupta, S. K. & Whitten, J. E. Thermal stability of thiol and silane monolayers: A comparative study. *Appl Surf Sci* **256**, 2742-2749, doi:DOI 10.1016/j.apsusc.2009.11.020 (2010).
28 Ulman, A. Formation and structure of self-assembled monolayers. *Chem Rev* **96**, 1533-1554, doi:Doi 10.1021/Cr9502357 (1996).
29 Li, Y., Li, L. & Sun, J. Q. Bioinspired Self-Healing Superhydrophobic Coatings. *Angew Chem Int Edit* **49**, 6129-6133, doi:DOI 10.1002/anie.201001258 (2010).
30 Xue, C. H. & Ma, J. Z. Long-lived superhydrophobic surfaces. *J Mater Chem A* **1**, 4146-4161, doi:Doi 10.1039/C2ta01073a (2013).
31 Paxson, A. T., Yagüe, J. L., Gleason, K. K. & Varanasi, K. K. Stable Dropwise Condensation for Enhancing Heat Transfer via the Initiated Chemical Vapor Deposition (iCVD) of Grafted Polymer Films. *Adv Mater* **26**, 418–423 (2014).
32 Haraguchi, T., Shimada, R., Kumagai, S. & Takeyama, T. The Effect of Polyvinylidene Chloride Coating Thickness on Promotion of Dropwise Steam Condensation. *Int J Heat Mass Tran* **34**, 3047-3054, doi:Doi 10.1016/0017-9310(91)90074-O (1991).
33 Holden, K. M., Wanniarachchi, A. S., Marto, P. J., Boone, D. H. & Rose, J. W. The Use of Organic Coatings to Promote Dropwise Condensation of Steam. *J Heat Trans-T Asme* **109**, 768-774 (1987).
34 Stylianou, S. A. & Rose, J. W. Dropwise Condensation on Surfaces Having Different Thermal-Conductivities. *J Heat Trans-T Asme* **102**, 477-482 (1980).
35 Gupta, M., Kapur, V., Pinkerton, N. M. & Gleason, K. K. Initiated chemical vapor deposition (iCVD) of conformal polymeric nanocoatings for the surface modification of high-aspect-ratio pores. *Chem Mater* **20**, 1646-1651, doi:Doi 10.1021/Cm702810j (2008).
36 Kananeh, A. B., Rausch, M. H., Froba, A. P. & Leipertz, A. Experimental study of dropwise condensation on plasma-ion implanted stainless steel tubes. *Int J Heat Mass Tran* **49**, 5018-5026, doi:DOI 10.1016/j.ijheatmasstransfer.2006.04.039 (2006).
37 Kananeh, A. B., Rausch, M. H., Leipertz, A. & Froba, A. P. Dropwise Condensation Heat Transfer on Plasma-Ion-Implanted Small Horizontal Tube Bundles. *Heat Transfer Eng* **31**, 821-828, doi:Doi 10.1080/01457630903547545 (2010).
38 Zhao, Q. & Burnside, B. M. Dropwise Condensation of Steam on Ion-Implanted Condenser Surfaces. *Heat Recov Syst Chp* **14**, 525-534, doi:Doi 10.1016/0890-4332(94)90055-8 (1994).
39 Leipertz, A. & Froba, A. P. Improvement of condensation heat transfer by surface modifications. *Heat Transfer Eng* **29**, 343-356, doi:Doi 10.1080/01457630701821563 (2008).
40 Erb, R. A. Wettability of Metals under Continuous Condensing Conditions. *J Phys Chem-Us* **69**, 1306-1309, doi:Doi 10.1021/J100888a035 (1965).

41 Fowkes, F. M. Attractive Forces at Interfaces. *Ind Eng Chem* **56**, 40-&, doi:Doi 10.1021/Ie50660a008 (1964).
42 Bewig, K. W. & Zisman, W. A. Wetting of Gold and Platinum by Water. *J Phys Chem-Us* **69**, 4238-4242, doi:Doi 10.1021/J100782a029 (1965).
43 Erb, R. A. Wettability of Gold. *J Phys Chem-Us* **72**, 2412-&, doi:Doi 10.1021/J100853a023 (1968).
44 Bernett, M. K. & Zisman, W. A. Confirmation of Spontaneous Spreading by Water on Pure Gold. *J Phys Chem-Us* **74**, 2309-2312, doi:Doi 10.1021/J100705a012 (1970).
45 Schrader, M. E. Ultrahigh-Vacuum Techniques in the Measurement of Contact Angles .5. Leed Study of the Effect of Structure on the Wettability of Graphite. *J Phys Chem-Us* **84**, 2774-2779, doi:Doi 10.1021/J100458a021 (1980).
46 Smith, T. The Hydrophilic Nature of a Clean Gold Surface. *J Colloid Interf Sci* **75**, 51-55, doi:Doi 10.1016/0021-9797(80)90348-3 (1980).
47 Enright, R., Miljkovic, N., Alvarado, J. L., Kim, K. J. & Rose, J. W. Dropwise Condensation on Micro- and Nanostructured Surfaces. *Nanoscale and Microscale Thermophysical Engineering* **18**, 223-250, doi:10.1080/15567265.2013.862889 (2014).
48 Paxson, A. T., Yague, J. L., Gleason, K. K. & Varanasi, K. K. Stable Dropwise Condensation for Enhancing Heat Transfer via the Initiated Chemical Vapor Deposition (iCVD) of Grafted Polymer Films. *Adv Mater* **26**, 418-423, doi:10.1002/adma.201303065 (2013).
49 Miljkovic, N., Preston, D. J., Enright, R. & Wang, E. N. Electrostatic charging of jumping droplets. *Nat Commun* **4**, doi:Artn 2517
Doi 10.1038/Ncomms3517 (2013).
50 Bartell, F. E. & Cardwell, P. H. Reproducible contact angles on reproducible metal surfaces I Contact angles of water against silver and gold. *J Am Chem Soc* **64**, 494-497, doi:Doi 10.1021/Ja01255a007 (1942).
51 Azimi, G., Dhiman, R., Kwon, H. M., Paxson, A. T. & Varanasi, K. K. Hydrophobicity of rare-earth oxide ceramics. *Nat Mater* **12**, 315-320, doi:Doi 10.1038/Nmat3545 (2013).
52 2014, C. d. f. g. o. f. m. c. c. a. f. h. a. c. f. s. c. r. F.
53 Martinez, L. *et al.* Surface study of cerium oxide based coatings obtained by cathodic electrodeposition on zinc. *Appl Surf Sci* **257**, 6202-6207, doi:DOI 10.1016/j.apsusc.2011.02.033 (2011).
54 Lawrence, N. J., Jiang, K. & Cheung, C. L. Formation of a porous cerium oxide membrane by anodization. *Chemical Communications* **47**, 2703-2705, doi:Doi 10.1039/C0cc04806b (2011).
55 Erb, R. A. Wettability of Gold. *Journal of Physical Chemistry* **72**, 2412-2417, doi:Doi 10.1021/J100853a023 (1968).
56 Schneegans, M. & Menzel, E. Gold Crystals Solidified in Air Are Hydrophilic. *J Colloid Interf Sci* **88**, 97-99, doi:Doi 10.1016/0021-9797(82)90158-8 (1982).
57 Gaines, G. L. On the Water Wettability of Gold. *J Colloid Interf Sci* **79**, 295-295, doi:Doi 10.1016/0021-9797(81)90076-X (1981).
58 Schrader, M. E. Wettability of Clean Metal-Surfaces. *J Colloid Interf Sci* **100**, 372-380, doi:Doi 10.1016/0021-9797(84)90442-9 (1984).
59 Takeda, S., Fukawa, M., Hayashi, Y. & Matsumoto, K. Surface OH group governing adsorption properties of metal oxide films. *Thin Solid Films* **339**, 220-224, doi:Doi 10.1016/S0040-6090(98)01152-3 (1999).
60 Strohmeier, B. R. The Effects of O-2 Plasma Treatments on the Surface-Composition and Wettability of Cold-Rolled Aluminum Foil. *J Vac Sci Technol A* **7**, 3238-3245, doi:Doi 10.1116/1.576342 (1989).
61 Li, Z. T. *et al.* Effect of airborne contaminants on the wettability of supported graphene and graphite. *Nat Mater* **12**, 925-931, doi:Doi 10.1038/Nmat3709 (2013).
62 Can, L. & Qin, X. Ft-Ir Spectroscopic Investigation of Methane Adsorption on Cerium Oxide. *J Phys Chem-Us* **96**, 7714-7718 (1992).

63 Kwon, H.-M. *Tailoring Hydrodynamics of Non-wetting Droplets with Nano-engineered Surfaces* Doctor of Philosophy in Mechanical Engineering thesis, Massachusetts Institute of Technology, (2013).
64 Nickerson, R. Plasma surface modification for cleaning and adhesion. *Polymers, Laminations & Coatings Conference, Books 1 and 2*, 1101-1108 (1998).
65 Sumner, A. L. *et al.* The nature of water on surfaces of laboratory systems and implications for heterogeneous chemistry in the troposphere. *Phys Chem Chem Phys* **6**, 604-613, doi:Doi 10.1039/B308125g (2004).
66 Wasy, A. *et al.* Argon plasma treatment on metal substrates and effects on diamond-like carbon (DLC) coating properties. *Crystal Research and Technology* **49**, 55-62, doi:10.1002/crat.201300171 (2014).
67 Umezu, I. *et al.* Effects of argon and hydrogen plasmas on the surface of silicon. *Vacuum* **66**, 453-456, doi:Pii S0042-207x(02)00170-7
Doi 10.1016/S0042-207x(02)00170-7 (2002).
68 Bormashenko, E., Pogreb, R., Whyman, G. & Erlich, M. Resonance Cassie-Wenzel wetting transition for horizontally vibrated drops deposited on a rough surface. *Langmuir* **23**, 12217-12221, doi:Doi 10.1021/La7016374 (2007).
69 Bormashenko, E., Pogreb, R., Whyman, G., Bormashenko, Y. & Erlich, M. Vibration-induced Cassie-Wenzel wetting transition on rough surfaces. *Appl Phys Lett* **90** (2007).
70 Noblin, X., Buguin, A. & Brochard-Wyart, F. Vibrated sessile drops: Transition between pinned and mobile contact line oscillations. *Eur Phys J E* **14**, 395-404, doi:DOI 10.1140/epje/i2004-10021-5 (2004).
71 figures., S. s. m. a. w. a. f. a. i. o. c. m. d. d. o. t. c. a. m. t. R. t. c. a. s.
72 Gao, L. C. & McCarthy, T. J. Wetting 101 degrees. *Langmuir* **25**, 14105-14115, doi:Doi 10.1021/La902206c (2009).
73 Gao, L. C. & McCarthy, T. J. Contact angle hysteresis explained. *Langmuir* **22**, 6234-6237, doi:Doi 10.1021/La060254j (2006).
74 Tanasawa, I. Recent Advances in Condensation Heat Transfer. *Inst Chem E*, 297-312 (1994).
75 Lefevre, E. J. & Rose, J. W. A Theory of Heat Transfer by Dropwise Condensation. *Chem Eng Prog* **62**, 86-& (1966).
76 Barr, T. L. & Seal, S. Nature of the Use of Adventitious Carbon as a Binding-Energy Standard. *J Vac Sci Technol A* **13**, 1239-1246, doi:Doi 10.1116/1.579868 (1995).
77 Stojilovic, N. Why Can't We See Hydrogen in X-ray Photoelectron Spectroscopy? *J Chem Educ* **89**, 1331-1332, doi:Doi 10.1021/Ed300057j (2012).
78 Thomas, R. R., Kaufman, F. B., Kirleis, J. T. & Belsky, R. A. Wettability of polished silicon oxide surfaces. *J Electrochem Soc* **143**, 643-648, doi:Doi 10.1149/1.1836494 (1996).
79 Katz, D. L. & Saltman, W. Surface tension of hydrocarbons. *Ind Eng Chem* **31**, 91-94, doi:Doi 10.1021/Ie50349a019 (1939).
80 Birch, W., Carre, A. & Mittal, K. L. Wettability Techniques to Monitor the Cleanliness of Surfaces. *Dev Surf Contam Cl* **1**, 693-723 (2008).
81 Lanin, S. N. *et al.* Hydrocarbon adsorption on gold clusters: Experiment and quantum chemical modeling. *Russ J Phys Chem a+* **84**, 2133-2142, doi:Doi 10.1134/S0036024410120228 (2010).
82 Kim, J. H. *et al.* Direct observation of adsorption geometry for the van der Waals adsorption of a single pi-conjugated hydrocarbon molecule on Au(111). *J Chem Phys* **140**, doi:Artn 074709
Doi 10.1063/1.4864458 (2014).
83 Jones, G., Studt, F., Abild-Pedersen, F., Norskov, J. K. & Bligaard, T. Scaling relationships for adsorption energies of C-2 hydrocarbons on transition metal surfaces. *Chem Eng Sci* **66**, 6318-6323, doi:DOI 10.1016/j.ces.2011.02.050 (2011).
84 Rigo, V. A., Metin, C. O., Nguyen, Q. P. & Miranda, C. R. Hydrocarbon Adsorption on Carbonate Mineral Surfaces: A First-Principles Study with van der Waals Interactions. *J Phys Chem C* **116**, 24538-24548, doi:Doi 10.1021/Jp306040n (2012).

85 Raj, R., Enright, R., Zhu, Y. Y., Adera, S. & Wang, E. N. Unified Model for Contact Angle Hysteresis on Heterogeneous and Superhydrophobic Surfaces. *Langmuir* **28**, 15777-15788, doi:Doi 10.1021/La303070s (2012).
86 Chen, Y. L., Helm, C. A. & Israelachvili, J. N. Molecular Mechanisms Associated with Adhesion and Contact-Angle Hysteresis of Monolayer Surfaces. *J Phys Chem-Us* **95**, 10736-10747, doi:Doi 10.1021/J100179a041 (1991).
87 Wisdom, K. M. *et al.* Self-cleaning of superhydrophobic surfaces by self-propelled jumping condensate. *P Natl Acad Sci USA* **110**, 7992-7997, doi:DOI 10.1073/pnas.1210770110 (2013).
88 Cao, L. L., Jones, A. K., Sikka, V. K., Wu, J. Z. & Gao, D. Anti-Icing Superhydrophobic Coatings. *Langmuir* **25**, 12444-12448, doi:Doi 10.1021/La902882b (2009).
89 Mishchenko, L. *et al.* Design of Ice-free Nanostructured Surfaces Based on Repulsion of Impacting Water Droplets. *Acs Nano* **4**, 7699-7707, doi:Doi 10.1021/Nn102557p (2010).
90 Miljkovic, N. & Wang, E. N. Condensation heat transfer on superhydrophobic surfaces. *Mrs Bull* **38**, 397-406, doi:Doi 10.1557/Mrs.2013.103 (2013).
91 Novoselov, K. S. *et al.* Two-dimensional atomic crystals. *P Natl Acad Sci USA* **102**, 10451-10453, doi:DOI 10.1073/pnas.0502848102 (2005).
92 Novoselov, K. S. *et al.* Electric field effect in atomically thin carbon films. *Science* **306**, 666-669, doi:DOI 10.1126/science.1102896 (2004).
93 Chen, X. Y. *et al.* Fully Integrated Graphene and Carbon Nanotube Interconnects for Gigahertz High-Speed CMOS Electronics. *Ieee T Electron Dev* **57**, 3137-3143, doi:Doi 10.1109/Ted.2010.2069562 (2010).
94 Li, X. S. *et al.* Transfer of Large-Area Graphene Films for High-Performance Transparent Conductive Electrodes. *Nano Lett* **9**, 4359-4363, doi:Doi 10.1021/Nl902623y (2009).
95 Wang, X., Zhi, L. J. & Mullen, K. Transparent, conductive graphene electrodes for dye-sensitized solar cells. *Nano Lett* **8**, 323-327, doi:Doi 10.1021/Nl072838r (2008).
96 O'Hern, S. C. *et al.* Selective Molecular Transport through Intrinsic Defects in a Single Layer of CVD Graphene. *Acs Nano* **6**, 10130-10138, doi:Doi 10.1021/Nn303869m (2012).
97 Goli, P. *et al.* Thermal Properties of Graphene-Copper-Graphene Heterogeneous Films. *Nano Lett* **14**, 1497-1503, doi:Doi 10.1021/Nl404719n (2014).
98 Malekpour, H. *et al.* Thermal Conductivity of Graphene Laminate. *Nano Lett* **14**, 5155-5161, doi:Doi 10.1021/Nl501996v (2014).
99 Yan, Z., Liu, G. X., Khan, J. M. & Balandin, A. A. Graphene quilts for thermal management of high-power GaN transistors. *Nat Commun* **3**, doi:Artn 827
Doi 10.1038/Ncomms1828 (2012).
100 Raj, R., Maroo, S. C. & Wang, E. N. Wettability of Graphene. *Nano Lett* **13**, 1509-1515, doi:Doi 10.1021/Nl304647t (2013).
101 Shin, Y. J. *et al.* Surface-Energy Engineering of Graphene. *Langmuir* **26**, 3798-3802, doi:Doi 10.1021/La100231u (2010).
102 Li, X. L. *et al.* Highly conducting graphene sheets and Langmuir-Blodgett films. *Nat Nanotechnol* **3**, 538-542, doi:DOI 10.1038/nnano.2008.210 (2008).
103 Blake, P. *et al.* Graphene-based liquid crystal device. *Nano Lett* **8**, 1704-1708, doi:Doi 10.1021/Nl080649i (2008).
104 Balandin, A. A. Thermal properties of graphene and nanostructured carbon materials. *Nat Mater* **10**, 569-581, doi:Doi 10.1038/Nmat3064 (2011).
105 Seol, J. H. *et al.* Two-Dimensional Phonon Transport in Supported Graphene. *Science* **328**, 213-216, doi:DOI 10.1126/science.1184014 (2010).
106 Renteria, J. D., Nika, D. L. & Balandin, A. A. Graphene Thermal Properties: Applications in Thermal Management and Energy Storage. *Appl Sci-Basel* **4**, 525-547, doi:Doi 10.3390/App4040525 (2014).
107 Hesjedal, T. Continuous roll-to-roll growth of graphene films by chemical vapor deposition. *Appl Phys Lett* **98**, doi:Artn 133106

Doi 10.1063/1.3573866 (2011).
108 Bae, S. *et al.* Roll-to-roll production of 30-inch graphene films for transparent electrodes. *Nat Nanotechnol* **5**, 574-578, doi:Doi 10.1038/Nnano.2010.132 (2010).
109 Rafiee, J. *et al.* Wetting transparency of graphene. *Nat Mater* **11**, 217-222, doi:Doi 10.1038/Nmat3228 (2012).
110 Shih, C. J. *et al.* Breakdown in the Wetting Transparency of Graphene. *Phys Rev Lett* **109**, doi:Artn 176101
Doi 10.1103/Physrevlett.109.176101 (2012).
111 Shih, C. J., Strano, M. S. & Blankschtein, D. Wetting translucency of graphene. *Nat Mater* **12**, 866-869, doi:Doi 10.1038/Nmat3760 (2013).
112 Schrader, M. E. Ultrahigh-Vacuum Techniques in Measurement of Contact Angles .3. Water on Copper and Silver. *J Phys Chem-Us* **78**, 87-89, doi:Doi 10.1021/J100594a017 (1974).
113 Trevoy, D. J. & Johnson, H. The Water Wettability of Metal Surfaces. *J Phys Chem-Us* **62**, 833-837, doi:Doi 10.1021/J150565a016 (1958).
114 Preston, D. J. *et al.* Effect of hydrocarbon adsorption on the wettability of rare earth oxide ceramics. *Appl Phys Lett* **105**, doi:Artn 011601
Doi 10.1063/1.4886410 (2014).
115 Schrader, M. E. Ultrahigh-Vacuum Techniques in Measurement of Contact Angles .2. Water on Gold. *J Phys Chem-Us* **74**, 2313-2317, doi:Doi 10.1021/J100705a013 (1970).
116 Wilkins, D. G., Bromley, L. A. & Read, S. M. Dropwise and Filmwise Condensation of Water Vapor on Gold. *Aiche J* **19**, 119-123, doi:DOI 10.1002/aic.690190117 (1973).
117 Woodruff, D. W. & Westwater, J. W. Steam Condensation on Electroplated Gold - Effect of Plating Thickness. *Int J Heat Mass Tran* **22**, 629-632, doi:Doi 10.1016/0017-9310(79)90066-8 (1979).
118 Bhaviripudi, S., Jia, X. T., Dresselhaus, M. S. & Kong, J. Role of Kinetic Factors in Chemical Vapor Deposition Synthesis of Uniform Large Area Graphene Using Copper Catalyst. *Nano Lett* **10**, 4128-4133, doi:Doi 10.1021/Nl102355e (2010).
119 Li, X. S. *et al.* Large-Area Synthesis of High-Quality and Uniform Graphene Films on Copper Foils. *Science* **324**, 1312-1314, doi:DOI 10.1126/science.1171245 (2009).
120 Reina, A. *et al.* Large Area, Few-Layer Graphene Films on Arbitrary Substrates by Chemical Vapor Deposition. *Nano Lett* **9**, 30-35, doi:Doi 10.1021/Nl801827v (2009).
121 Nair, R. R. *et al.* Fine structure constant defines visual transparency of graphene. *Science* **320**, 1308-1308, doi:DOI 10.1126/science.1156965 (2008).
122 Miljkovic, N., Enright, R. & Wang, E. N. Modeling and Optimization of Superhydrophobic Condensation. *Journal of Heat Transfer* **135**, 111004-111004, doi:10.1115/1.4024597 (2013).
123 Rose, J. W. & Glicksman, L. R. Dropwise condensation - the distribution of drop sizes. *Int J Heat Mass Tran* **16**, 411-425 (1973).
124 Rumaa, J. Drop Size Distribution and Heat-Flux of Dropwise Condensation. *Chem Eng J Bioch Eng* **16**, 171-176 (1978).
125 Lam, C. N. C., Wu, R., Li, D., Hair, M. L. & Neumann, A. W. Study of the advancing and receding contact angles: liquid sorption as a cause of contact angle hysteresis. *Adv Colloid Interfac* **96**, 169-191, doi:Pii S0001-8686(01)00080-X
Doi 10.1016/S0001-8686(01)00080-X (2002).
126 Tanner, D. W., Pope, D., Potter, C. J. & West, D. Heat Transfer in Dropwise Condensation at Low Steam Pressures in Absence and Presence of Non-Condensable Gas. *Int J Heat Mass Tran* **11**, 181-182, doi:Doi 10.1016/0017-9310(68)90148-8 (1968).
127 Sundararaman, T. G. & Venkatram, T. Heat-Transfer during Dropwise Condensation of Steam in Presence of Non-Condensable Gases - Effects of Geometrical Shape of Surface Reversal of Cooling Water-Flow and Orientation. *Indian J Technol* **14**, 313-321 (1976).
128 Vosough, A. *et al.* Improvement Power Plant Efficiency with Condenser Pressure. *INTERNATIONAL JOURNAL OF MULTIDISCIPLINARY SCIENCES AND ENGINEERING* **2**, 38-43 (2011).

129 Bejan, A. Fundamentals of exergy analysis, entropy generation minimization, and the generation of flow architecture. *Int J Energ Res* **26**, 545-565, doi:Doi 10.1002/Er.804 (2002).
130 Wilmshurst, R. & Rose, J. W. in *Fourth International Heat Transfer Conference* Vol. 6 (Elsevier, Paris-Versailles, France, 1970).
131 Leidheiser, H. Corrosion of Painted Metals - a Review. *Corrosion* **38**, 374-383 (1982).
132 Shahil, K. M. F. & Balandin, A. A. Graphene-Multilayer Graphene Nanocomposites as Highly Efficient Thermal Interface Materials. *Nano Lett* **12**, 861-867, doi:Doi 10.1021/Nl203906r (2012).
133 Boreyko, J. B. & Chen, C. H. Vapor chambers with jumping-drop liquid return from superhydrophobic condensers. *Int J Heat Mass Tran* **61**, 409-418, doi:DOI 10.1016/j.ijheatmasstransfer.2013.01.077 (2013).
134 Boreyko, J. B. & Chen, C. H. Self-Propelled Dropwise Condensate on Superhydrophobic Surfaces. *Phys Rev Lett* **103**, 184501-184501 - 184501-184504, doi:Artn 184501
Doi 10.1103/Physrevlett.103.184501 (2009).
135 Miljkovic, N. *et al.* Jumping-Droplet-Enhanced Condensation on Scalable Superhydrophobic Nanostructured Surfaces. *Nano Lett* **13**, 179-187, doi:Doi 10.1021/Nl303835d (2013).
136 Cavalli, A. *et al.* Electrically induced drop detachment and ejection. *Phys Fluids* **28**, doi:Artn 022101
10.1063/1.4940213 (2016).
137 Miljkovic, N., Preston, D. J. & Wang, E. N. in *Encyclopedia of Two-Phase Heat Transfer and Flow II: Special Topics and Applications* (eds John R. Thome & Jungho Kim) 85-131 (World Scientific, 2015).
138 Bhatia, B. *et al.* Nanoengineered Surfaces for Thermal Energy Conversion. *15th International Conference on Micro and Nanotechnology for Power Generation and Energy Conversion Applications (Powermems 2015)* **660**, doi:Artn 012036
10.1088/1742-6596/660/1/012036 (2015).
139 Preston, D. J. & Massachusetts Institute of Technology. Department of Mechanical Engineering. *Electrostatic charging of jumping droplets on superhydrophobic nanostructured surfaces : fundamental study and applications*.
140 Oh, J. *et al.* Jumping-droplet electronics hot-spot cooling. *Appl Phys Lett* **110**, doi:Artn 123107
10.1063/1.4979034 (2017).
141 Cho, H. J., Preston, D. J., Zhu, Y. & Wang, E. N. Nanoengineering materials for liquid–vapour phase-change heat transfer. *Nature Materials Reviews* **2** (2016).
142 Liu, T. Y. & Kim, C. J. Turning a surface superrepellent even to completely wetting liquids. *Science* **346**, 1096-1100, doi:10.1126/science.1254787 (2014).
143 Weisensee, P. B., Torrealba, E. J., Raleigh, M., Jacobi, A. M. & King, W. P. Hydrophobic and oleophobic re-entrant steel microstructures fabricated using micro electrical discharge machining. *J Micromech Microeng* **24**, doi:Artn 095020
10.1088/0960-1317/24/9/095020 (2014).
144 Varanasi, K. K., Hsu, M., Bhate, N., Yang, W. S. & Deng, T. Spatial Control in the Heterogeneous Nucleation of Water. *Appl Phys Lett* **95**, 094101-094101 - 094101-094103, doi:Artn 094101
Doi 10.1063/1.3200951 (2009).
145 Enright, R., Miljkovic, N., Al-Obeidi, A., Thompson, C. V. & Wang, E. N. Condensation on Superhydrophobic Surfaces: The Role of Local Energy Barriers and Structure Length Scale. *Langmuir* **28**, 14424-14432, doi:Doi 10.1021/La302599n (2012).
146 Kim, P., Kreder, M. J., Alvarenga, J. & Aizenberg, J. Hierarchical or Not? Effect of the Length Scale and Hierarchy of the Surface Roughness on Omniphobicity of Lubricant-Infused Substrates. *Nano Lett* **13**, 1793-1799, doi:Doi 10.1021/Nl4003969 (2013).
147 Wexler, J. S., Jacobi, I. & Stone, H. A. Shear-Driven Failure of Liquid-Infused Surfaces. *Phys Rev Lett* **114**, doi:Artn 168301
10.1103/Physrevlett.114.168301 (2015).

148 Irajizad, P., Hasnain, M., Farokhnia, N., Sajadi, S. M. & Ghasemi, H. Magnetic slippery extreme icephobic surfaces. *Nat Commun* **7**, doi:Artn 13395
10.1038/Ncomms13395 (2016).
149 Park, K. C. *et al.* Condensation on slippery asymmetric bumps. *Nature* **531**, 78-82, doi:10.1038/nature16956 (2016).
150 Epstein, A. K., Wong, T. S., Belisle, R. A., Boggs, E. M. & Aizenberg, J. Liquid-infused structured surfaces with exceptional anti-biofouling performance. *P Natl Acad Sci USA* **109**, 13182-13187, doi:DOI 10.1073/pnas.1201973109 (2012).
151 Boreyko, J. B., Polizos, G., Datskos, P. G., Sarles, S. A. & Collier, C. P. Air-stable droplet interface bilayers on oil-infused surfaces. *P Natl Acad Sci USA* **111**, 7588-7593, doi:10.1073/pnas.1400381111 (2014).
152 Epstein, A. K., Pokroy, B., Seminara, A. & Aizenberg, J. Bacterial biofilm shows persistent resistance to liquid wetting and gas penetration. *P Natl Acad Sci USA* **108**, 995-1000, doi:DOI 10.1073/pnas.1011033108 (2011).
153 Glavan, A. C. *et al.* Omniphobic "R-F Paper" Produced by Silanization of Paper with Fluoroalkyltrichlorosilanes. *Adv Funct Mater* **24**, 60-70, doi:10.1002/adfm.201300780 (2014).
154 Kim, P. *et al.* Liquid-Infused Nanostructured Surfaces with Extreme Anti-Ice and Anti-Frost Performance. *Acs Nano* **6**, 6569-6577, doi:Doi 10.1021/Nn302310q (2012).
155 Lee, C., Kim, H. & Nam, Y. Drop Impact Dynamics on Oil-Infused Nanostructured Surfaces. *Langmuir* **30**, 8400-8407, doi:10.1021/la501341x (2014).
156 Seo, D., Lee, J., Lee, C. & Nam, Y. The effects of surface wettability on the fog and dew moisture harvesting performance on tubular surfaces. *Sci Rep-Uk* **6**, doi:Artn 24276
10.1038/Srep24276 (2016).
157 Jung, S. M. *et al.* Porous Cu Nanowire Aerosponges from One-Step Assembly and their Applications in Heat Dissipation. *Adv Mater* **28**, 1413-1419, doi:10.1002/adma.201504774 (2016).
158 Vaaler, L. E. Impregnated porous condenser surfaces. (1959).
159 Verheijen, H. J. J. & Prins, M. W. J. Reversible electrowetting and trapping of charge: Model and experiments. *Langmuir* **15**, 6616-6620, doi:Doi 10.1021/La990548n (1999).
160 Quere, D. Non-sticking drops. *Rep Prog Phys* **68**, 2495-2532, doi:Doi 10.1088/0034-4885/68/11/R01 (2005).
161 Lafuma, A. & Quere, D. Slippery pre-suffused surfaces. *Epl-Europhys Lett* **96**, doi:Artn 56001
Doi 10.1209/0295-5075/96/56001 (2011).
162 Wong, T. S. *et al.* Bioinspired self-repairing slippery surfaces with pressure-stable omniphobicity. *Nature* **477**, 443-447, doi:Doi 10.1038/Nature10447 (2011).
163 Rykaczewski, K. *et al.* Dropwise Condensation of Low Surface Tension Fluids on Omniphobic Surfaces. *Sci Rep-Uk* **4**, doi:Artn 4158
10.1038/Srep04158 (2014).
164 Nam, Y. & Ju, Y. S. Comparative Study of Copper Oxidation Schemes and Their Effects on Surface Wettability. *Imece 2008: Heat Transfer, Fluid Flows, and Thermal Systems, Vol 10, Pts a-C*, 1833-1838 (2009).
165 Enright, R., Miljkovic, N., Dou, N., Nam, Y. & Wang, E. N. Condensation on Superhydrophobic Copper Oxide Nanostructures. *J Heat Trans-T Asme* **135**, doi:Artn 091304
Doi 10.1115/1.4024424 (2013).
166 Miljkovic, N., Preston, D. J., Enright, R. & Wang, E. N. Electric-Field-Enhanced Condensation on Superhydrophobic Nanostructured Surfaces. *Acs Nano* **7**, 11043-11054, doi:Doi 10.1021/Nn404707j (2013).
167 Preston, D. J., Miljkovic, N., Enright, R. & Wang, E. N. Jumping Droplet Electrostatic Charging and Effect on Vapor Drag. *Journal of Heat Transfer* (2014).
168 Miljkovic, N., Preston, D. J., Enright, R. & Wang, E. N. Jumping-droplet electrostatic energy harvesting. *Appl Phys Lett* **105**, doi:Artn 013111
Doi 10.1063/1.4886798 (2014).

169 Preston, D. J. *et al.* Electrowetting-on-Dielectric Actuation of a Vertical Translation and Angular Manipulation Stage. *Appl Phys Lett* **109**, 244102 (2016).
170 Preston, D. J. *et al.* in *2017 IEEE 30th International Conference on Micro Electro Mechanical Systems (MEMS)* 769-772 (IEEE, Las Vegas, 2017).
171 Nusselt, W. The surface condensation of steam. *Z Ver Dtsch Ing* **60**, 569-575 (1916).
172 Wilmhurst, R. *Heat transfer during dropwise condensation of steam, ethane 1, 2 diol, aniline and nitrobenzene* Doctoral thesis, Queen Mary University of London, (1979).
173 Miljkovic, N., Enright, R. & Wang, E. N. Modeling and Optimization of Condensation Heat Transfer on Micro and Nanostructured Superhydrophobic Surfaces. *Journal of Heat Transfer* **in press** (2012).
174 Ma, X. H., Zhou, X. D., Lan, Z., Li, Y. M. & Zhang, Y. Condensation Heat Transfer Enhancement in the Presence of Non-Condensable Gas Using the Interfacial Effect of Dropwise Condensation. *Int J Heat Mass Tran* **51**, 1728-1737, doi:DOI 10.1016/j.ijheatmasstransfer.2007.07.021 (2008).
175 Preston, D. J., Mafra, D. L., Miljkovic, N., Kong, J. & Wang, E. N. Scalable Graphene Coatings for Enhanced Condensation Heat Transfer. *Nano Lett* **15**, 2902-2909, doi:10.1021/nl504628s (2015).
176 Weisensee, P. B. *et al.* Condensate droplet size distribution on lubricant-infused surfaces. *Int J Heat Mass Tran* **109**, 187-199 (2017).
177 Anand, S., Rykaczewski, K., Subramanyam, S. B., Beysens, D. & Varanasi, K. K. How droplets nucleate and grow on liquids and liquid impregnated surfaces. *Soft Matter* **11**, 69-80, doi:10.1039/c4sm01424c (2015).
178 Smith, D. J. *et al.* Droplet mobility on lubricant-impregnated surfaces. *Soft Matter* **9**, 1772-1780 (2013).
179 Anand, S., Paxson, A. T., Dhiman, R., Smith, D. J. & Varanasi, K. K. Enhanced Condensation on Lubricant-Impregnated Nanotextured Surfaces *Acs Nano* **6**, 10122–10129 (2012).
180 Liu, Y., Wexler, J. S., Schonecker, C. & Stone, H. A. Effect of viscosity ratio on the shear-driven failure of liquid-infused surfaces. *Phys Rev Fluids* **1**, doi:Artn 074003
10.1103/Physrevfluids.1.074003 (2016).
181 Nishino, T., Meguro, M., Nakamae, K., Matsushita, M. & Ueda, Y. The lowest surface free energy based on -CF3 alignment. *Langmuir* **15**, 4321-4323, doi:Doi 10.1021/La981727s (1999).
182 Lundy, R. *et al.* Exploring the Role of Adsorption and Surface State on Hydrophobicity of Rare Earth Oxides. *ACS Appl Mater Interfaces* **9**, 13751−13760 (2017).
183 Fu, S. P. *et al.* On the wetting behavior of ceria thin films grown by pulsed laser deposition. *Appl Phys Lett* **110**, doi:Artn 081601
10.1063/1.4973997 (2017).
184 Kulah, E. *et al.* Surface chemistry of rare-earth oxide surfaces at ambient conditions: reactions with water and hydrocarbons. *Sci Rep-Uk* **7**, doi:Artn 43369
10.1038/Srep43369 (2017).
185 He, Q. H., Ma, C. C., Hu, X. Q. & Chen, H. W. Method for Fabrication of Paper-Based Microfluidic Devices by Alkylsilane Self-Assembling and UV/O-3-Patterning. *Anal Chem* **85**, 1327-1331, doi:10.1021/ac303138x (2013).
186 Asano, H. & Shiraishi, Y. Development of paper-based microfluidic analytical device for iron assay using photomask printed with 3D printer for fabrication of hydrophilic and hydrophobic zones on paper by photolithography. *Anal Chim Acta* **883**, 55-60, doi:10.1016/j.aca.2015.04.014 (2015).
187 Fowkes, F. M. Determination of Interfacial Tensions, Contact Angles, and Dispersion Forces in Surfaces by Assuming Additivity of Intermolecular Interactions in Surfaces. *J Phys Chem-Us* **66**, 382-&, doi:Doi 10.1021/J100808a524 (1962).
188 Owens, D. K. & Wendt, R. C. Estimation of Surface Free Energy of Polymers. *J Appl Polym Sci* **13**, 1741-&, doi:DOI 10.1002/app.1969.070130815 (1969).
189 Vanoss, C. J., Chaudhury, M. K. & Good, R. J. Interfacial Lifshitz-Vanderwaals and Polar Interactions in Macroscopic Systems. *Chem Rev* **88**, 927-941, doi:Doi 10.1021/Cr00088a006 (1988).

190 Vanoss, C. J. & Good, R. J. Prediction of the Solubility of Polar Polymers by Means of Interfacial-Tension Combining Rules. *Langmuir* **8**, 2877-2879, doi:Doi 10.1021/La00048a006 (1992).
191 Vanoss, C. J. & Good, R. J. On the Mechanism of Hydrophobic Interactions. *J Disper Sci Technol* **9**, 355-362, doi:Doi 10.1080/01932698808943994 (1988).
192 Aria, A. I. *et al.* Time Evolution of the Wettability of Supported Graphene under Ambient Air Exposure. *J Phys Chem C* **120**, 2215-2224, doi:10.1021/acs.jpcc.5b10492 (2016).
193 Kontogeorgis, G. M. & Kiil, S. *Introduction to applied colloid and surface chemistry*.
194 Janczuk, B., Wojcik, W. & Zdziennicka, A. Determination of the Components of the Surface-Tension of Some Liquids from Interfacial Liquid-Liquid Tension Measurements. *J Colloid Interf Sci* **157**, 384-393, doi:DOI 10.1006/jcis.1993.1200 (1993).
195 Della Volpe, C. & Siboni, S. Some reflections on acid-base solid surface free energy theories. *J Colloid Interf Sci* **195**, 121-136 (1997).
196 Della Volpe, C., Maniglio, D., Brugnara, M., Siboni, S. & Morra, M. The solid surface free energy calculation - I. In defense of the multicomponent approach. *J Colloid Interf Sci* **271**, 434-453, doi:10.1016/j.jcis.2003.09.049 (2004).
197 Della Volpe, C. & Siboni, S. Acid-base surface free energies of solids and the definition of scales in the Good-van Oss-Chaudhury theory. *Journal of Adhesion Science and Technology* **14**, 235-272, doi:Doi 10.1163/156856100742546 (2000).
198 Fernandez, V. & Khayet, M. Evaluation of the surface free energy of plant surfaces: toward standardizing the procedure. *Front Plant Sci* **6**, doi:Artn 510
10.3389/Fpls.2015.00510 (2015).
199 Dalal, E. N. Calculation of Solid-Surface Tensions. *Langmuir* **3**, 1009-1015, doi:Doi 10.1021/La00078a023 (1987).
200 Weng, M. & Shen, Q. Effect of liquid surface tension data on the validity and accuracy of solid surface tension components and parameters in the application of the van Oss-Chaudhury-Good approach. *Journal of Adhesion Science and Technology* **28**, 2248-2268, doi:10.1080/01694243.2014.958332 (2014).
201 Kwok, D. Y. The usefulness of the Lifshitz-van der Waals/acid-base approach for surface tension components and interfacial tensions. *Colloid Surface A* **156**, 191-200, doi:Doi 10.1016/S0927-7757(99)00070-9 (1999).
202 Lee, L. H. Relevance of film pressures to interfacial tension, miscibility of liquids, and Lewis acid-base approach. *J Colloid Interf Sci* **214**, 64-78, doi:DOI 10.1006/jcis.1999.6165 (1999).
203 Lee, L. H. The gap between the measured and calculated liquid-liquid interfacial tensions derived from contact angles. *Journal of Adhesion Science and Technology* **14**, 167-185, doi:Doi 10.1163/156856100742528 (2000).
204 Lee, L. H. The unified Lewis acid-base approach to adhesion and solvation at the liquid-polymer interface. *J Adhesion* **76**, 163-183, doi:Doi 10.1080/00218460108029623 (2001).
205 Restolho, J., Mata, J. L. & Saramago, B. On the interfacial behavior of ionic liquids: Surface tensions and contact angles. *J Colloid Interf Sci* **340**, 82-86, doi:10.1016/j.jcis.2009.08.013 (2009).
206 Law, G. & Watson, P. R. Surface tension measurements of N-alkylimidazolium ionic liquids. *Langmuir* **17**, 6138-6141, doi:10.1021/la010629v (2001).
207 Tariq, M. *et al.* Surface tension of ionic liquids and ionic liquid solutions. *Chem Soc Rev* **41**, 829-868, doi:10.1039/c1cs15146k (2012).
208 Clint, J. H. Adhesion and components of solid surface energies. *Curr Opin Colloid In* **6**, 28-33, doi:Doi 10.1016/S1359-0294(00)00084-4 (2001).
209 van Oss, C. J., Wu, W., Docoslis, A. & Giese, R. F. The interfacial tensions with water and the Lewis acid-base surface tension parameters of polar organic liquids derived from their aqueous solubilities. *Colloid Surface B* **20**, 87-91, doi:Doi 10.1016/S0927-7765(00)00169-7 (2001).
210 Boudenne, A., Ibos, L., Candau, Y. & Thomas, S. Handbook of Multiphase Polymer Systems, Vols 1-2. *Handbook of Multiphase Polymer Systems, Vols 1-2*, 1-1010, doi:10.1002/9781119972020 (2011).

211 Peterson, I. R. Towards a theory of adhesion with predictive power. *Surf Coat Int Pt B-C* **88**, 1-8, doi:Doi 10.1007/Bf02699701 (2005).
212 Chaudhury, M. K. Interfacial interaction between low-energy surfaces. *Mat Sci Eng R* **16**, 97-159, doi:Doi 10.1016/0927-796x(95)00185-9 (1996).
213 Xu, Z. H., Liu, Q. X. & Ling, J. H. An Evaluation of the Van Oss-Chaudhury-Good Equation and Neumanns Equation of State Approach with Mercury Substrate. *Langmuir* **11**, 1044-1046, doi:Doi 10.1021/La00003a058 (1995).
214 Gardner, D. J. Application of the Lifshitz-van der Waals acid-base approach to determine wood surface tension components. *Wood Fiber Sci* **28**, 422-428 (1996).
215 Aizenberg, J., Aizenberg, M. & Kim, P. Slips Surface Based on Metal-Containing Compound. United States patent (2015).
216 Daerr, A. & Mogne, A. Pendent_Drop: An ImageJ Plugin to Measure the Surface Tension from an Image of a Pendent Drop. *Journal of Open Research Software* **4**, e3, doi:http://doi.org/10.5334/jors.97 (2016).
217 Lundy, R. *et al.* Exploring the Role of Adsorption and Surface State on the Hydrophobicity of Rare Earth Oxides. *ACS Applied Materials & Interfaces* **9**, 13751-13760, doi:10.1021/acsami.7b01515 (2017).
218 Singh, H. & Dayal, B. Precise determination of the lattice parameters of holmium and erbium sesquioxides at elevated temperatures. *Journal of the Less Common Metals* **18**, 172 (1969).
219 Gupta, M. & Singh, S. Thermal Expansion of CeO2, Ho2O3, and Lu2O3 from 100° to 300°K by an X-Ray Method. *J Am Chem Soc* **53**, 663-665 (1970).
220 Erb, R. Dropwise condensation on gold. *Gold Bull* **6**, 2-6, doi:10.1007/bf03215172 (1973).
221 Rose, J. W. Dropwise Condensation Theory. *Int J Heat Mass Tran* **24**, 191-194, doi:Doi 10.1016/0017-9310(81)90026-0 (1981).
222 Zhu, Y. Y. *et al.* Prediction and Characterization of Dry-out Heat Flux in Micropillar Wick Structures. *Langmuir* **32**, 1920-1927, doi:10.1021/acs.langmuir.5b04502 (2016).
223 Zhu, Y. Y. *et al.* Surface Structure Enhanced Microchannel Flow Boiling. *J Heat Trans-T Asme* **138**, doi:Artn 091501
10.1115/1.4033497 (2016).
224 Touloukian, Y. S. Vol. 2 (IFI/Plenum, New York, 1970).
225 Fomarini, L., Conde, J. C., Alvani, C., Olevano, D. & Chiussi, S. Experimental determination of La2O3 thermal conductivity and its application to the thermal analysis of a-Ge/La2O3/c-Si laser annealing. *Thin Solid Films* **516**, 7400-7405, doi:DOI 10.1016/j.tsf.2008.02.032 (2008).
226 Mogensen, M., Sammes, N. M. & Tompsett, G. A. Physical, chemical and electrochemical properties of pure and doped ceria. *Solid State Ionics* **129**, 63-94, doi:Doi 10.1016/S0167-2738(99)00318-5 (2000).
227 Martin, J. J. & Dixon, G. S. Thermal Transport in Euo. *Phys Status Solidi B* **54**, 707-712, doi:DOI 10.1002/pssb.2220540235 (1972).
228 Gilchrist, K. E., Brown, R. G. & Preston, S. D. Physical-Properties of Europium Sesquioxide. *J Nucl Mater* **68**, 39-47, doi:Doi 10.1016/0022-3115(77)90214-8 (1977).
229 Celestini, F. & Kofman, R. Vibration of submillimeter-size supported droplets. *Phys Rev E* **73**, doi:Artn 041602
Doi 10.1103/Physreve.73.041602 (2006).
230 Kim, M. C., Yang, S. H., Boo, J. H. & Han, J. G. Surface treatment of metals using an atmospheric pressure plasma jet and their surface characteristics. *Surf Coat Tech* **174**, 839-844, doi:Doi 10.1016/S0257-8972(03)00560-7 (2003).
231 Trane. *Heat Exchanger Options*, <http://www.trane.com> (2006).
232 Gamza, J. *Optimizing Condenser Tube Life with Nondestructive Testing*, <http://www.concosystems.com> (
233 HTS. *Fluid Heat Transfer: RAE Coils - Condenser Coils*, <http://www.htseng.com/relinfostore/> (

234 Wei, Z. Y., Ni, Z. H., Bi, K. D., Chen, M. H. & Chen, Y. F. Interfacial thermal resistance in multilayer graphene structures. *Phys Lett A* **375**, 1195-1199, doi:DOI 10.1016/j.physleta.2011.01.025 (2011).
235 Delhaes, P. *Graphite and precursors*. (Gordon & Breach, 2001).
236 Shahil, K. M. F. & Balandin, A. A. Thermal properties of graphene and multilayer graphene: Applications in thermal interface materials. *Solid State Commun* **152**, 1331-1340, doi:DOI 10.1016/j.ssc.2012.04.034 (2012).
237 Incropera, F. P. *Introduction to heat transfer*. 5th edn, (Wiley, 2007).
238 Carey, V. P. *Liquid-vapor phase-change phenomena : an introduction to the thermophysics of vaporization and condensation processes in heat transfer equipment*. 2nd edn, (Taylor and Francis, 2008).
239 Enright, R., Dou, N., Miljkovic, N., Nam, Y. & Wang, E. N. Condensation on Superhydrophobic Copper Oxide Nanostructures. *Proceedings of the Asme Micro/Nanoscale Heat and Mass Transfer International Conference, 2012*, 419-425 (2012).
240 Liu, L. *et al.* Graphene oxidation: Thickness-dependent etching and strong chemical doping. *Nano Lett* **8**, 1965-1970, doi:Doi 10.1021/Nl0808684 (2008).
241 Chen, S. S. *et al.* Oxidation Resistance of Graphene-Coated Cu and Cu/Ni Alloy. *Acs Nano* **5**, 1321-1327, doi:Doi 10.1021/Nn103028d (2011).
242 Schriver, M. *et al.* Graphene as a Long-Term Metal Oxidation Barrier: Worse Than Nothing. *Acs Nano* **7**, 5763-5768, doi:Doi 10.1021/Nn4014356 (2013).
243 Gao, L. B. *et al.* Repeated growth and bubbling transfer of graphene with millimetre-size single-crystal grains using platinum. *Nat Commun* **3**, doi:Artn 699
Doi 10.1038/Ncomms1702 (2012).
244 Wang, Y. *et al.* Electrochemical Delamination of CVD-Grown Graphene Film: Toward the Recyclable Use of Copper Catalyst. *Acs Nano* **5**, 9927-9933, doi:Doi 10.1021/Nn203700w (2011).
245 Preston, D. J. & Woodbury, K. A. Cost-benefit analysis of retrofit of high-intensity discharge factory lighting with energy-saving alternatives. *Energ Effic* **6**, 255-269, doi:DOI 10.1007/s12053-012-9179-1 (2013).
246 Anders, A. *Learning a strategy for whole-arm grasping* SM thesis, Massachusetts Institute of Technology, (2014).

8. Supplementary Information

8.1 NOMENCLATURE

Symbols

d	Diameter (micro- or nanostructures)
D_{ID}	Tube inner diameter
D_{OD}	Tube outer diameter
f_{max}	Surface coverage of hydrocarbons
h	Height (micro- or nanostructures)
h_c	Condensation heat transfer coefficient
k	Thermal conductivity
k_p	Polymer thermal conductivity
L	Length (condenser tube)
l	Length (pitch between micro- or nanostructures)
P_{sat}	Saturation pressure
P_v	Vapor pressure
q”	Heat flux
R	Geometric factor for lubricant infused surface design
r	Roughness (ratio of actual to projected surface area)
S	Supersaturation
ΔT	Temperature difference or subcooling
T_{sat}	Saturation temperature
T_{wall}	Wall temperature
γ	Surface tension or surface energy
γ_i^+	Lewis acid component of surface energy, phase *i*
γ_i^-	Lewis base component of surface energy, phase *i*
γ_i^{LW}	Lifshitz-van Der Waals component of surface energy, phase *i*
δ	Coating thickness
δ_p	Polymer condenser coating thickness
$\theta_{1,A}$	Advancing contact angle of the underlying surface
$\theta_{2,A}$	Advancing contact angle of a hydrocarbon-covered surface
θ_A	Advancing contact angle

θ_R	Receding contact angle
φ	Solid fraction

Chemical Symbols

Al_2O_3	Aluminum(III) oxide
Ar	Argon (gas)
Au	Gold
CeO_2	Cerium(IV) oxide (ceria)
CH_4	Methane (gas)
Cu	Copper
Cu_2O	Copper(I) oxide
CuO	Copper(II) oxide
Fe_2O_3	Iron(III) oxide
H_2	Hydrogen (gas)
Ho_2O_3	Holmium(III) oxide (holmia)
$Na_3PO_4•12H_2O$	Sodium phosphate dodecahydrate
$NaClO_2$	Sodium chlorite
NaOH	Sodium hydroxide
OH^-	Hydroxyl group
Si	Silicon
SiO_2	Silicon dioxide (silica)
TiO_2	Titanium dioxide
ZrO_2	Zirconium dioxide

Acronyms

6F-IPA	Hexafluoroisopropanol
AFM	Atomic force microscopy
APCVD	Atmospheric pressure chemical vapor deposition
CVD	Chemical vapor deposition
DI	Deionized
DWC	Dropwise condensation
FWC	Filmwise condensation
GPL	General-purpose lubricant
iCVD	Initiated chemical vapor deposition

IPA	Isopropanol
LIS	Lubricant infused surface
LMTD	Log mean temperature difference
LPCVD	Low pressure chemical vapor deposition
LW	Lifshitz-van Der Waals
NCG	Noncondensable gas
OTS	Octadecyltrichlorosilane
OW	Owens and Wendt
PECVD	Plasma-enhanced chemical vapor deposition
PTFE	Polytetrafluoroethylene
REO	Rare earth oxide
SAM	Self-assembled monolayer
TFTS	Trichloro(1H,1H,2H,2H-perfluorooctyl)silane
vOCG	van Oss, Chaudhury, and Good
XPS	X-ray photoelectron spectroscopy

8.2 CH. 2 SUPPLEMENTARY INFORMATION

Characterization Methods

The field emission scanning electron microscope used to capture the images in this chapter was an Ultra Plus (Carl Zeiss AG). The in-lens detector was used to image the samples at a voltage of 2.00 kV. The samples were mounted to stubs with carbon tape and were not used for experimental results after imaging.

The AFM scans in this chapter were obtained with an Asylum MFP-3D using Bruker TESP probes. The scan rate was 5 μm/sec, and the scan area was 10 μm x 10 μm for the holmia sample and 20 μm x 20 μm for the ceria sample. The samples were not used for experimental results after the AFM scans were conducted.

The XPS spectra were obtained with a Thermo Scientific K-Alpha XPS. The measurements were performed with a 400 μm X-ray spot size at pressures less than $8x10^{-8}$ mBar. The spectra were post-processed with Advantage software (version 5.918) to determine the initial composition of the pristine samples and the surface atomic percent carbon at each time point from relative peak heights.

Contact angles were obtained with a Kyowa MCA-3 microgoniometer with a piezoelectric head to dispense picoliter-scale droplets at frequencies of 20 – 1000 Hz. The average advancing angle data was obtained by taking the mean of the advancing contact angles measured on at least 5 spots on each sample for each time point. The average receding contact angle was obtained by the same method, and was observed when the droplet contact line receded during evaporation of the droplet. See Figure S2 for the measured contact angle during the advancing and receding phases for a representative sample (holmia, 2448 hr after plasma cleaning process).

Advancing Contact Angle Model

The hydrocarbon adsorption phenomenon was modeled as hydrophobic defects on an initially hydrophilic surface to predict the advancing contact angle. Approximating the hydrocarbons as circular hydrophobic defects on the surface, the advancing angle is predicted by:

$$\boldsymbol{\cos(\theta_A) = f_{max}\cos(\theta_{1,A}) + (1 - f_{max})\cos(\theta_{2,A})}, \quad \text{(S1)}$$

where θ_A is the advancing contact angle as a function of the surface coverage of hydrocarbons, $\theta_{1,A}$ is the advancing contact angle of the hydrophilic surface with no adsorbed hydrocarbons ($\approx 0°$), and $\theta_{2,A}$ is the advancing contact angle on the surface once it has become saturated with hydrocarbons (approximated as the advancing angle at 2448 hours). The term f_{max} represents the surface area coverage of hydrophobic defects at the region where the energy barrier to advance is highest; in the case of uniform circular defects, this is the ratio of the diameter of a circular hydrophobic defect, D, to the side length of the square area surrounding each circular defect, L. Since the XPS spectra provide the surface atomic percent carbon and not the area coverage, the surface atomic percent carbon is converted to a ratio of hydrocarbon-covered surface area to total surface area, which is then used to determine $f_{max} = D/L$ and $\theta_A = \theta_A(f_{max})$.

To convert surface atomic percent carbon to percent hydrocarbon-covered surface area, the area ratio of the hydrocarbon molecules on the surface to the adsorbent surface molecules is required. This is approximated from the molar specific volumes as:

$$\boldsymbol{A_{HC}/A_M = (V_{HC}/V_M)^{2/3}}, \quad \text{(S2)}$$

where the subscript *HC* indicates hydrocarbons and the subscript *M* indicates the adsorbent surface molecules. The molar specific volume for methane was used in this analysis in order to assign one mole of hydrocarbon to every adsorbed carbon atom while maintaining a good estimate for hydrocarbon surface area. The fraction of hydrocarbon-covered surface area is then calculated as:

$$\boldsymbol{A_{HC}/A_{total} = (1 + (A_{HC}/A_M)(1 - C)/(C))^{-1}}, \quad \text{(S3)}$$

where C is the surface percent carbon by mole , which is obtained from the raw XPS surface atomic percent carbon by accounting for the number of atoms per molecule based on the unit molecules for which the molar specific volumes were obtained. Finally, f_{max} is calculated as:

$$\boldsymbol{f_{max} = \sqrt{(4/\pi)(A_{HC}/A_{total})}} \quad \text{(S4)}$$

The curve obtained from this model is shown to match well with the experimental data, indicating that hydrocarbon adsorption is a plausible mechanism for the observed increase in contact angle.

Rare Earth Oxide Thermal Conductivities

The thermal conductivities (k) for selected REOs are shown in Table S1. The calculated values were determined from known values for the density (ρ), heat capacity (C_p), and thermal diffusivity (α) of the REOs ($k = \alpha\rho C_p$). The experimentally measured values were obtained from literature.

Table S1. Thermal conductivities of selected REOs.

Element	Atomic #	Oxidation State	Thermal Cond., k_{calc} [W/m·K]	Thermal Cond., k_{exp} [W/m·K]
Yttrium	39	Y_2O_3	12.77	13.3[224]
Lanthanum	57	La_2O_3	5.88	6.0[225]
Cerium	58	CeO_2	-	11.7[224,226]
Samarium	62	Sm_2O_3	15.42	9.7[224]
Europium	63	EuO	-	7.0[227]
Europium	63	Eu_2O_3	2.33	2.4[228]
Gadolinium	64	Gd_2O_3	12.21	10.3[224]
Lutetium	71	Lu2O3	12.42	-

Comparison of Coating Thicknesses

To maintain the same thermal resistance for the coating, comparing REOs (taking a conservative thermal conductivity value of $k_{REO} \approx 5$ W/m·K) to polymer coatings (thermal conductivity $k_p \approx 0.2$ W/m·K) and using the relationship $\delta_{REO} \sim (k_{REO}/k_p)\bullet\delta_p$, we find that the REO coating can be ~25x thicker with comparable thermal resistance, where δ_{REO} is the thickness of the REO coating and δ_p is the thickness of a polymer coating which would result in an equivalent thermal resistance.

Microgoniometer Piezoelectric Head Droplet Injection

The piezoelectric head is capable of dispensing picoliter-scale droplets at frequencies of 20 – 1000 Hz during microgoniometric measurement. The potential to introduce vibrations in the droplet being observed during advancing of the contact angle by dispensing droplets for the piezoelectric head, which may cause the contact line to oscillate, is considered here. First, the Ohnesorge number for a water droplet of the size observed during contact angle measurement (diameter $D \approx 50$ μm) is:

$$\boldsymbol{Oh = \frac{\mu}{\sqrt{\rho \sigma D}} \approx 0.01} \tag{S5}$$

where μ is water viscosity, ρ is water density, and σ is water surface tension at room temperature. Therefore, viscous effects are neglected and a balance between inertial and surface tension forces is considered. Determining the droplet natural frequency for the first resonant mode in this case[68,70]:

$$\boldsymbol{f = \frac{1}{2\pi}\sqrt{\frac{6\sigma h(\theta)}{\rho(1-cos\theta)(2+cos\theta)}}R^{-3/2} \approx 6{,}000\ Hz} \tag{S6}$$

where θ is the droplet contact angle on the surface a (90° was used as a representative value) and $h(\theta)$ is a factor which includes the dependence on geometry.[229] The experimental data points were obtained with droplet dispensing frequencies of 20 – 40 Hz << 6,000 Hz (1,000 Hz droplet dispensing was used to align the camera, not for measurement); therefore, the resonant vibration modes of the droplet under observation were not activated and the contact line did not oscillate due to addition of picoliter-scale droplets, allowing for accurate measurement of the advancing contact angle during droplet dispensing.

This conclusion is supported by comparison between measurements and previous literature for the reference surfaces of silica and gold, for which the advancing contact angle reached 66° and 44°, respectively, in good agreement with well-documented values.[43,78]

Role of Advancing and Receding Contact Angle in Dropwise Condensation Performance

The contact angle hysteresis plays a large role in dropwise condensation, where the advancing and receding contact angles determine the force needed to hold a droplet stationary on an inclined condensing surface against the force of gravity. A typical scaling of maximum droplet size on a vertical condenser surface is obtained by balancing the droplet weight with the contact angle hysteresis force acting on the droplet, as shown in Equation S6, where it is observed that the advancing and receding contact angles provide valuable information about the expected droplet departure size while the equilibrium contact angle is unable to provide this information. The maximum droplet departure size directly affects the condensation heat transfer due to the thermal resistance through the droplet itself.[21,74,75]

$$\boldsymbol{R_{drop}} \sim \left(\frac{\boldsymbol{3\sigma(\cos(\theta_R) - \cos(\theta_A))}}{\boldsymbol{2\pi\rho g}}\right)^{\boldsymbol{1/2}} \tag{S7}$$

This is particularly important for rare earth oxide (REO) surfaces, where the contact angle hysteresis is up to 50–60° and can significantly hinder the shedding of droplets, thus degrading the heat transfer performance.

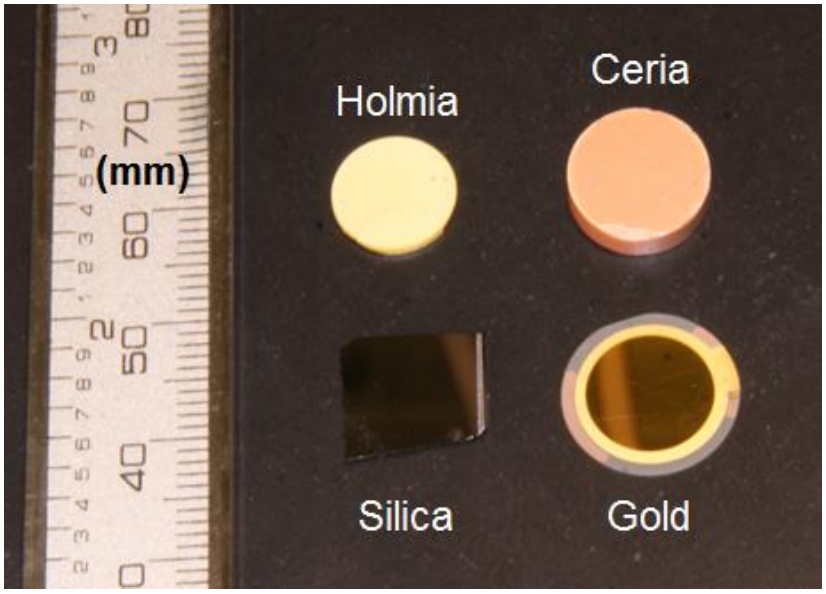

Figure S1. Image of the samples used for contact angle and XPS measurements. The silica sample is a 100 nm thick silicon dioxide layer on a silicon wafer. The gold sample is a sensor for a quartz crystal microbalance with 100 nm gold deposited on a glass substrate.

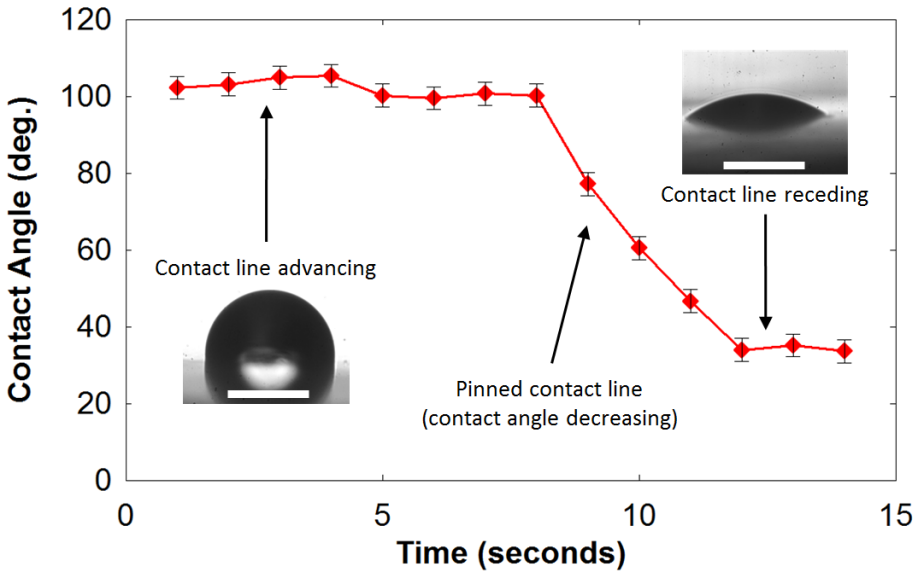

Figure S2. Representative data for measured contact angle on the holmia sample after exposure to laboratory air (temperature ≈ 25 °C, relative humidity ≈ 35%) for 2448 hr after plasma cleaning the sample. Initially, water was added to the droplet *via* the piezoelectric head on the microgoniometer at a greater rate than the evaporation rate of water from the droplet, and the droplet increased in volume by increasing the perimeter of the contact line at the advancing contact angle. At t = 8 seconds, water addition to the droplet was halted and it immediately began to decrease in volume as evaporation occurred. At first, the decrease in volume manifested as a decrease in the contact angle with a pinned contact line. When the contact angle reached the receding contact angle, the contact angle stopped decreasing and the contact line perimeter decreased, shown here for $t \geq 12$ seconds. Scale bars are 50 µm.

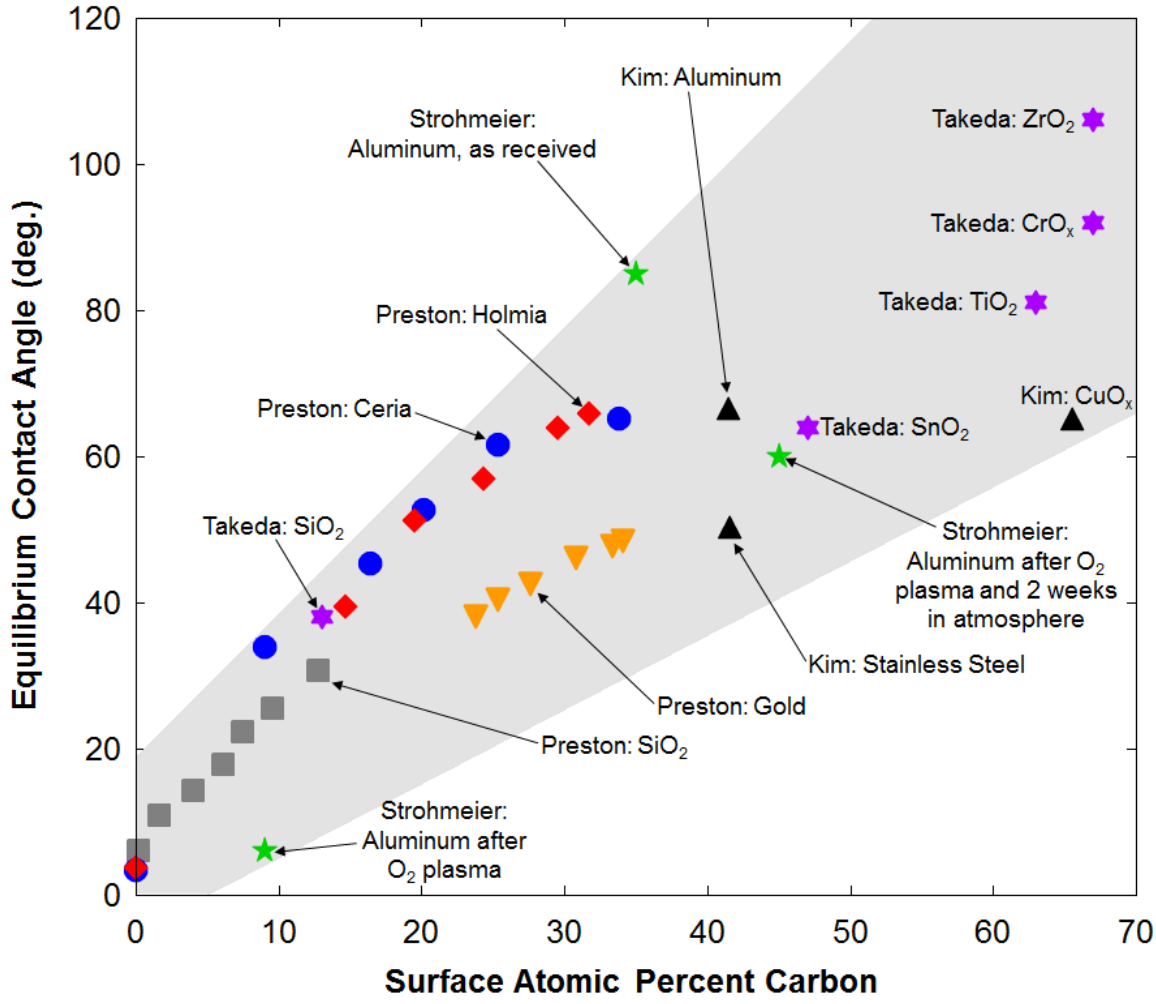

Figure S3. Comparison of experimental data from the present work (Preston) to previously published results for equilibrium contact angle as a function of surface atomic percent carbon. The previous studies provided only equilibrium contact angles, so the advancing and receding contact angles for the materials studied in the present work were arithmetically averaged to estimate the equilibrium contact angle, which is plotted here for fair comparison. Takeda deposited 40-nm-thick metal oxide films onto a silica substrate by reactive magnetron sputtering and exposed the samples to atmosphere with controlled relative humidity and temperature.[59] Kim provided contact angle and XPS measurements for bare metals which had been exposed to atmosphere for long times.[230] Strohmeier cleaned cold-rolled aluminum foil with oxygen plasma and subsequently exposed the foil to ambient atmosphere (experimental data for as-received bare aluminum was also included).[60] The shaded region highlights the positive correlation between contact angle and surface carbon contamination, which applies to rare earth

oxides as well as metals, metal oxides, and silica. The data spread is attributed to differences in hydrocarbon alignment when adsorbed on different materials, preferential adsorption of certain species of hydrocarbons for each material, and the use of surface atomic percent carbon as opposed to surface area fraction of hydrocarbons, which would account for the relative sizes of hydrocarbons versus surface molecules.

8.3 CH. 3 SUPPLEMENTARY INFORMATION

ESEM Characterization

The nucleation and initial growth of water droplets on graphene CVD surfaces were studied with an environmental scanning electron microscope (ESEM, Carl Zeiss EVO 50). A bare copper sample which had been annealed at 1000 °C under hydrogen in the CVD chamber but then removed without graphene growth was also examined as a control. The contact angles determined for the graphene CVD surfaces with microgoniometric characterization were confirmed with the ESEM, as shown in Figure S4.

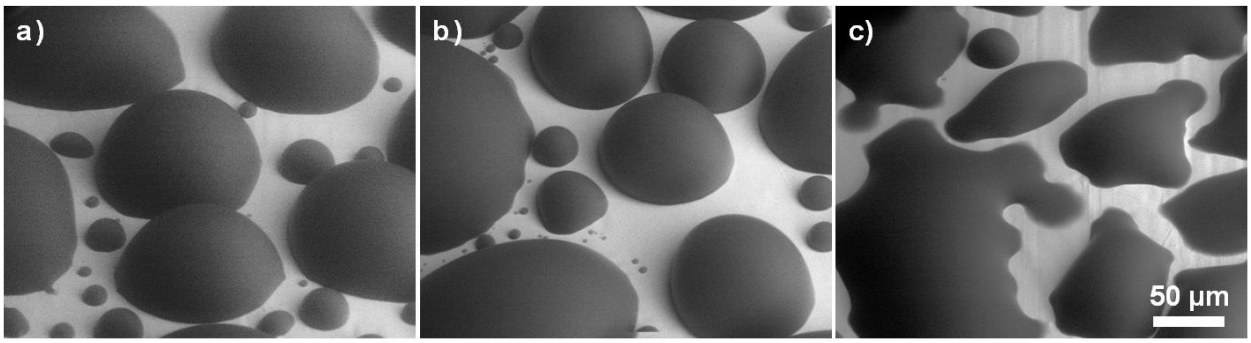

Figure S4. ESEM images of condensation on (a) LPCVD graphene on copper, (b) APCVD graphene on copper, and (c) bare copper after annealing in hydrogen. The advancing contact angles of droplets on the graphene-coated copper were approximately 90 degrees, while the advancing contact angle on the bare copper was much lower, resulting in a film as condensation continued.

Thermal Resistance of Graphene Compared to Substrate

The thermal resistance of a graphene coating is negligible compared to the resistance of the metal surface used to separate the condenser section from the chiller water in a heat exchanger.

The thickness for a copper condenser tube wall used in practice is on the order of $t_{Cu} \approx 0.5$ mm,[231-233] and copper has a thermal conductivity of $k_{Cu} \approx 400$ W/m-K. Meanwhile, the thickness for a single-layer graphene coating is approximately $t_{Gr} \approx 0.5$ nm, and graphene has a thermal conductivity in the transverse direction of $k_{Gr} \approx 0.1$ W/m-K.[104,234,235] Finally, the expected graphene contact resistance for graphene is on the order of $R_{c,Gr} \approx 10^{-8}$ m^2-K/W.[236] Taking the ratio of thermal resistance through the copper tube to resistance through the graphene sheet yields:

$$\frac{R_{Cu}}{R_{Gr}} = \frac{t_{Cu}/k_{Cu}}{t_{Gr}/k_{Gr} + R_{c,Gr}} \approx 80 \gg unity \quad \text{(S8)}$$

This indicates that the thermal resistance of the metal is much greater than that of the graphene CVD coating, even when considering the thinnest condenser walls widely commercially available and the highest reported values for graphene thermal resistance and contact resistance. For the present study, thicker condenser walls were used which resulted in a thermal resistance ratio of $R_{Cu}/R_{Gr} > 100$.

Condensation Chamber Setup

The custom environmental chamber used for this work (Kurt J. Lesker) consists of a stainless steel frame with a door (sealed with a rubber gasket), two viewing windows, and apertures for various components. Resistive heater lines were wrapped around the exterior of the chamber walls to prevent condensation at the inside walls and then insulated on the exterior walls. The output power of the resistive heater lines was controlled by a voltage regulator (Variac). Two insulated stainless steel water flow lines (Swagelok) were fed into the chamber *via* a KF flange port (Kurt J. Lesker) to supply cooling water to the chamber from a large capacity chiller (System III, Neslab).

A secondary stainless steel tube line was fed into the chamber *via* a KF adapter port that served as the flow line for the incoming water vapor supplied from a heated steel water reservoir. The vapor line was wrapped with a rope heater (60 W, Omega) and controlled by a power supply (Agilent). The vapor reservoir was wrapped with another independently-controlled rope heater (120 W, Omega) and insulated to limit heat losses to the environment. The access tubes were welded to the vapor reservoir, each with independently-controlled valves. The first valve (Diaphragm Type, Swagelok), connecting the bottom of the reservoir to the ambient, was used to fill the reservoir with water. The second valve (BK-60, Swagelok), connecting the top of the reservoir to the inside of the chamber, provided a path for vapor inflow. K-type thermocouples were located along the length of the water vapor reservoir to monitor temperature.

A bellows valve (Kurt J. Lesker) was attached to the chamber to serve as a leak port between the ambient and inside of the chamber. In order to monitor temperatures within the chamber, K-type thermocouple bundles were connected through the chamber apertures *via* a thermocouple feed through (Kurt J. Lesker). To provide electrical connections inside the chamber for LED lighting and electric field generation, insulated copper electrical wires were connected through the chamber apertures *via* an electrical feed through (Kurt J. Lesker). A pressure transducer (925 Micro Pirani, MKS) was attached to monitor

pressure within the chamber. The thermocouple bundles and the pressure transducer were both electrically connected to an analog input source (RAQ DAQ, National Instruments), which was interfaced to a computer for data recording. A second bellows valve (Kurt J. Lesker) was integrated onto the chamber for the vacuum pump, which brought down the chamber to vacuum conditions prior to vapor filling. A liquid nitrogen cold trap was incorporated along the line from the chamber to the vacuum which served to remove any moisture from the pump-down process and ultimately assist in yielding higher quality vacuum conditions. A tertiary bellows valve (Kurt J. Lesker) was integrated on a T fitting between the vacuum pump and liquid nitrogen reservoir to connect the vacuum line to the ambient to release the vacuum line to ambient conditions once pump down was achieved. In order to visually capture data, a digital SLR camera (Canon EOS 50D) was placed in line with the 5" viewing windows on the chamber. The schematic of the exterior of the environmental setup is depicted in Figure S5a. Images of the front and rear of the experimental setup are shown in Figures S5b and c, respectively.

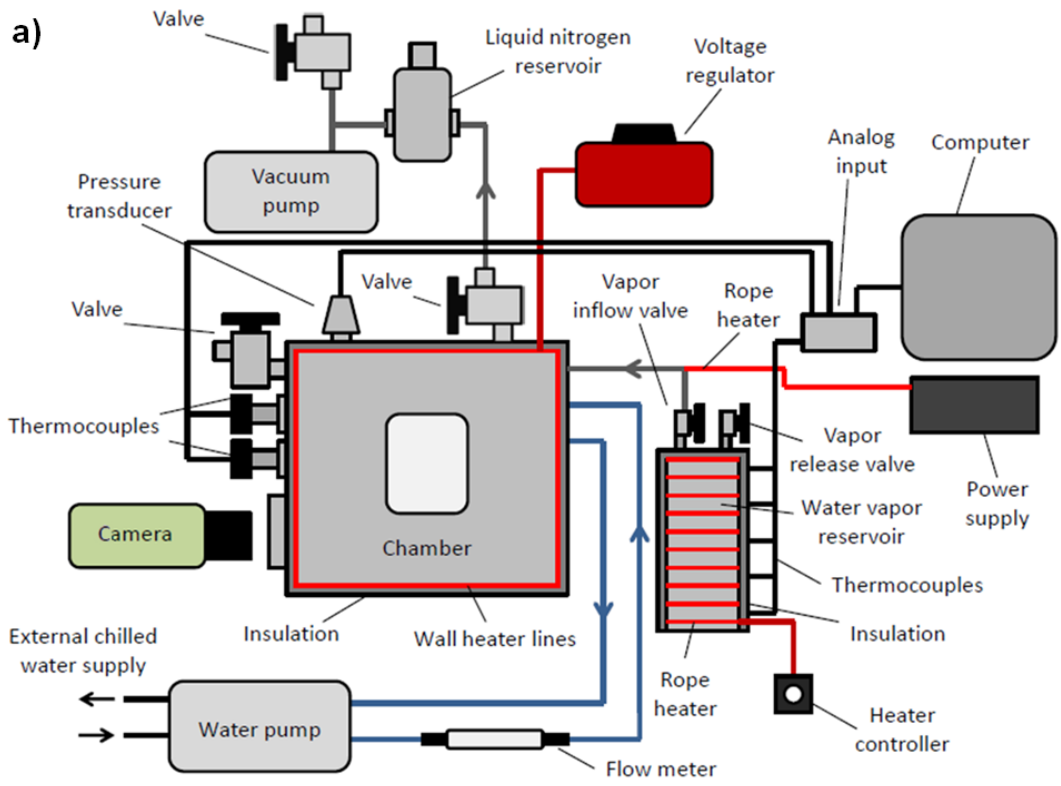

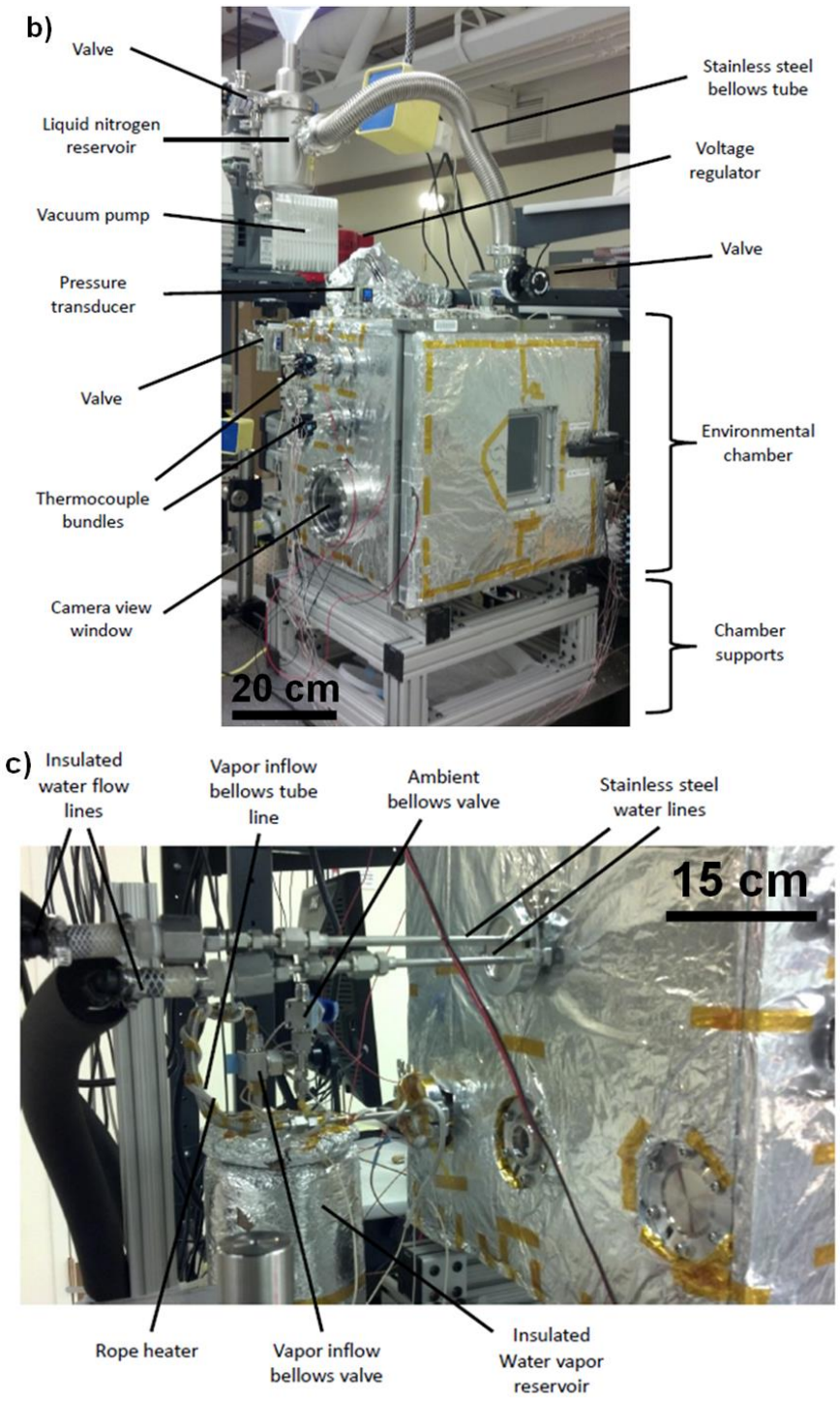

Figure S5. (a) Schematic of experimental setup (not to scale). (b) Image of the experimental setup shown from the front (high speed camera and data acquisition system not shown). (c) Image of the experimental setup from the rear of the chamber showing the cooling water inlet and outlet and water vapor reservoir. Reprinted with permission from Reference 4. Copyright 2012 American Chemical Society.[135]

The setup used to run experiments inside the chamber is shown in Figure S6. Stainless steel bellows tube lines (1/4", Swagelok) were connected to the external water flow lines (Figure S6c). T-connection adapters (Swagelok) with bore through Ultra-Torr fittings (Swagelok) were used to adapt K-type thermocouple probes (Omega) at the water inlet and outlet.

The graphene-coated copper tube test sample consisted of a 6.35 mm diameter tube, which was connected *via* a Swagelok compression fitting onto the T-connection. Chilled water flows through the inlet bellows tube, along the inside of the tube sample and through the outlet. Two supports were used to hold the sample and the entire configuration in place. Two separate pieces of insulation were embedded with K-type thermocouple leads and used for wet bulb temperature measurement during experimental runs. A third thermocouple was placed beside the sample to measure the reference temperature inside the chamber.

Condensation Procedure

For each experimental trial, a set of strict procedures was followed to ensure consistency throughout the experiments. The first step of the process was to turn on the voltage regulator to heat up the environmental chamber walls, which prevented condensation on the chamber walls. Simultaneously, the water vapor reservoir was filled with approximately 3.5 liters of DI water (99% full) using a syringe through the vapor release valve. After opening the vapor inflow valve and closing the vapor release valve, the rope heater around the water vapor reservoir was turned on with the heater controller set to maximum output (120 W). Then the rope heater connected to the vapor inflow valve was turned on. The temperature of the water reservoir was monitored with the installed thermocouples; the temperature at the top of the reservoir was higher than that of the middle/bottom of the reservoir due to the water thermal-mass present at the middle/bottom section. Hence, we ensured that the regions of the water reservoir of higher thermal capacity were brought to a sufficiently high temperature for boiling. During the boiling process, aluminum foil was placed on the bottom surface of the inner chamber to collect any of the water leaving the vapor inflow line. Once boiling was achieved and all thermocouples on the reservoir were > 95˚C for at least 10 minutes, the vapor inflow valve was closed. The excess water that spilled inside the chamber during de-gassing of the reservoir was removed.

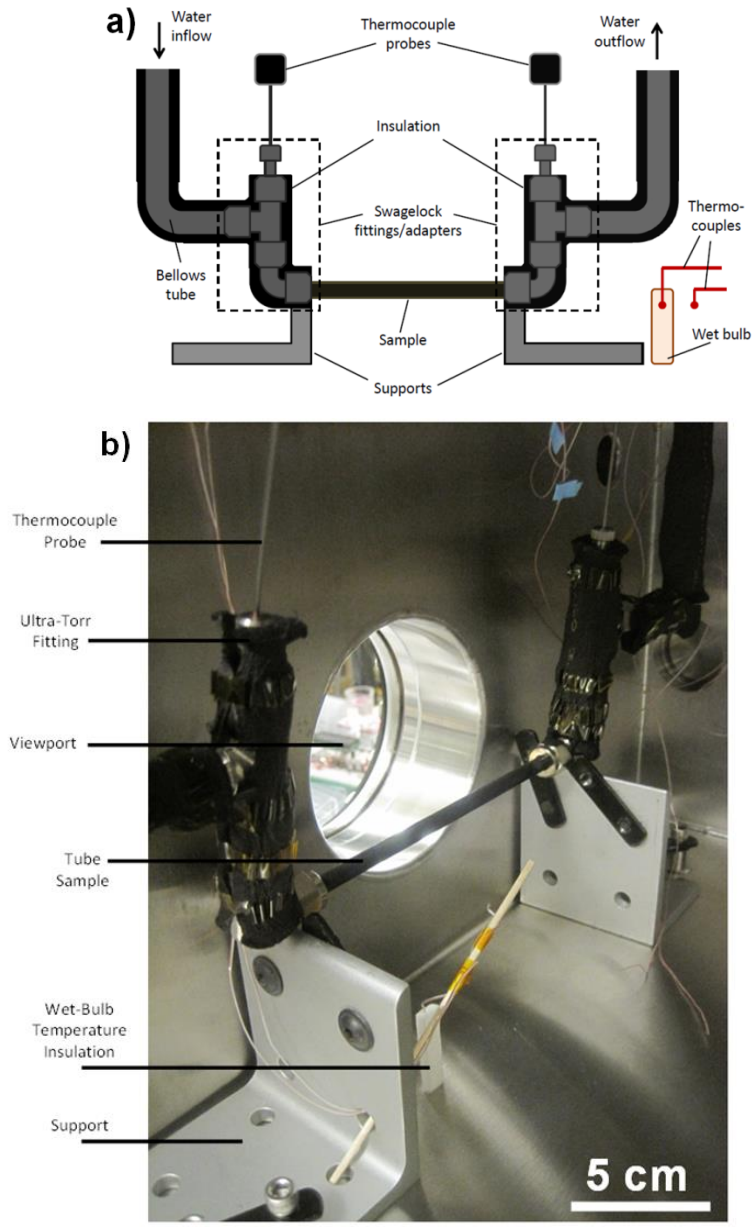

Figure S6. (a) Schematic of experimental setup inside the chamber (not to scale). (b) Image of the experimental setup inside the chamber showing a tube in place for testing. Reprinted with permission from Reference 4. Copyright 2012 American Chemical Society.[135]

In order to install the samples onto the rig (Figure S6), the Swagelok female adapters at the ends of the tube samples were connected to the 90 degree male elbow connecters on the rig. Before installing the entire sample setup in the chamber, all adapters/connecters were tightened to ensure that there were no

leaks that could affect vacuum performance. The setup was then placed on top of the steel supports and the bellows tubes (for the water inflow/outflow) were connected to the water lines. Then the insulating wet bulb wick was placed near the sample and in contact with the bottom surface of the chamber.

The next step was to begin the vacuum pump-down procedure. Initially, the liquid nitrogen cold trap was filled to about half capacity. The ambient exposed valves connecting the chamber and the vacuum pump were both closed and the valve connected to the liquid nitrogen cold trap was opened. The vacuum pump was then turned on, initiating the pump-down process. The pressure inside the chamber was monitored during the pump-down process. This process took approximately one hour in order to achieve the target vacuum conditions (0.5 Pa < P < 1 Pa). The experimental operating pressure of non-condensable was set to be a maximum of 0.25% of the operating pressure. Non-condensable gas content of above 0.5% (pressure) was shown to significantly degrade performance during dropwise condensation.[21,174] In our experiments, extreme care was taken to properly de-gas the vacuum chamber and water vapor reservoir prior to experimental testing. In addition, the chamber leak rate was characterized prior to each run in order to estimate the maximum time available for acquiring high fidelity data with non-condensable content of less than 0.25%.

The setup of the water flow-loop is described as follows: the Neslab water pump reservoir was filled and turned on to a flow rate of 5 L/min (0 < ΔT_{LMTD} < 15 K). The flow rate was monitored with the flow meter integrated in the inflow water line. In order to bring the chilled water into the flow loop and to the tube sample, the external chilled water lines were opened.

Prior to beginning experiments, the camera was turned on for visual imaging of the sample during condensation. Afterwards, the rope heater around the water reservoir was turned off and the vapor inflow valve was slowly turned open until the operating pressure was reached. Steady state conditions were typically reached after 2 minutes of full operation.

Heat Transfer Coefficient and Error Propagation

An energy balance was applied to the tube sample to determine the overall condensation heat transfer by calculating the change in enthalpy of the chiller water flowing inside the tube:

$$\boldsymbol{Q = \dot{m} c_p (T_{out} - T_{in})} \tag{S9}$$

where Q is the overall condensation heat transfer rate, $\dot{m}$ is the chiller water mass flow rate, c_p is the chiller water specific heat, and T_{in} and T_{out} are the tube inlet and outlet temperatures, respectively. The temperature difference between the chiller water and vapor far from the tube sample was also determined, represented here as the log mean temperature difference (LMTD) to account for the change in temperature of the chiller water along the tube length:

$$\boldsymbol{\Delta T_{LMTD} = \frac{(T_v - T_{in}) - (T_v - T_{out})}{\ln\left(\frac{T_v - T_{in}}{T_v - T_{out}}\right)}} \tag{S10}$$

where T_v is the temperature of the surrounding vapor far from the tube sample ($T_v = T_{sat}(P_v)$). From the overall condensation heat transfer and the log mean temperature difference, the overall heat transfer coefficient, $\overline{U}$, was determined:

$$\boldsymbol{\overline{U} = \frac{Q}{A \Delta T_{LMTD}} = \frac{\dot{m} c_p (T_{out} - T_{in})}{A \Delta T_{LMTD}}} \tag{S11}$$

where A is the surface area of the outer tube surface ($A = 2\pi rL$, where r = 3.175 mm, L = 8.71 cm). Note that the overall heat transfer coefficient is a function of only the product of experimentally measured parameters raised to powers. Therefore, the error associated with $\overline{U}$ is calculated as follows:

$$\boldsymbol{E_{\overline{U}} = \overline{U} \sqrt{\left(\frac{E_{\dot{m}}}{\dot{m}}\right)^2 + \left(\frac{E_{(T_{out} - T_{in})}}{(T_{out} - T_{in})}\right)^2 + \left(\frac{-E_A}{A}\right)^2 + \left(\frac{-E_{\Delta T_{LMTD}}}{\Delta T_{LMTD}}\right)^2}} \tag{S12}$$

The condensation heat transfer coefficient can be extracted from $\overline{U}$ by considering a series of thermal resistances that sum to $\overline{U}$ and isolating the resistance associated with condensation:

$$\frac{\mathbf{1}}{\bar{\boldsymbol{U}}\boldsymbol{A}} = \frac{\mathbf{1}}{\boldsymbol{h_i A_i}} + \boldsymbol{R_t} + \frac{\mathbf{1}}{\boldsymbol{h_c A}} \tag{S13}$$

Rearranging to evolve explicitly for h_c:

$$\boldsymbol{h_c} = \left(\frac{\mathbf{1}}{\bar{\boldsymbol{U}}} - \frac{\boldsymbol{A}}{\boldsymbol{h_i A_i}} - \boldsymbol{R_t A}\right)^{\mathbf{-1}} \tag{S14}$$

where A_i is the surface area on the inner surface of the tube ($A_i = 2\pi r_i L$), R_t is the thermal resistance of the tube ($R_t = \ln(r/r_i)/(2\pi k_t)$, k_t is the tube material thermal conductivity), and the internal heat transfer coefficient, h_i, is determined from the Gnielinski correlation for pipe flow:

$$\boldsymbol{h_i} = \left(\frac{\boldsymbol{k_i}}{\mathbf{2}\boldsymbol{r_i}}\right)\frac{(\boldsymbol{f}/\mathbf{8})(\boldsymbol{Re} - \mathbf{1000})\boldsymbol{Pr}}{\mathbf{1} + \mathbf{12.7}(\boldsymbol{f}/\mathbf{8})^{\mathbf{1/2}}(\boldsymbol{Pr}^{\mathbf{2/3}} - \mathbf{1})} \tag{S15}$$

$$\boldsymbol{f} = (\mathbf{0.790}\ln \boldsymbol{Re} - \mathbf{1.64})^{\mathbf{-2}} \tag{S16}$$

$$\boldsymbol{Re} = \frac{\boldsymbol{\rho v}(\mathbf{2}\boldsymbol{r_i})}{\boldsymbol{\mu}} \tag{S17}$$

where f is the friction factor, Re is the Reynolds number, Pr is the Prandtl number, ρ is the chiller water density, k_i is the chiller water thermal conductivity, and μ is the chiller water dynamic viscosity. Solving for h_i and substituting into the above Equation S7 allows for determination of h_c. As h_c is not a simple function of a product of powers, the error is determined as a function of the first partial derivatives of h_c with respect to its components.

$$\boldsymbol{E_{h_c}} = \boldsymbol{h_c}\sqrt{\left(\frac{\boldsymbol{\partial h_c}}{\boldsymbol{\partial h_i}}\boldsymbol{E_{h,i}}\right)^{\mathbf{2}} + \left(\frac{\boldsymbol{\partial h_c}}{\boldsymbol{\partial \bar{U}}}\frac{\boldsymbol{E_{\bar{U}}}}{\bar{\boldsymbol{U}}}\right)^{\mathbf{2}}} \tag{S18}$$

$$\frac{\boldsymbol{\partial h_c}}{\boldsymbol{\partial h_i}} = \frac{-(\boldsymbol{A}/\boldsymbol{A_i})\bar{\boldsymbol{U}}^{\mathbf{2}}}{(\boldsymbol{h_i} - (\boldsymbol{A}/\boldsymbol{A_i})\bar{\boldsymbol{U}} - \boldsymbol{R_t A}\bar{\boldsymbol{U}}\boldsymbol{h_i})^{\mathbf{2}}} \tag{S19}$$

$$\frac{\boldsymbol{\partial h_c}}{\boldsymbol{\partial \bar{U}}} = \frac{\boldsymbol{h_i}^{\mathbf{2}}}{(\boldsymbol{h_i} - (\boldsymbol{A}/\boldsymbol{A_i})\bar{\boldsymbol{U}} - \boldsymbol{R_t A}\bar{\boldsymbol{U}}\boldsymbol{h_i})^{\mathbf{2}}} \tag{S20}$$

The error in $\bar{U}$ was determined and the error in h_i was estimated as 10% associated with the Gnielinski correlation.[237] Table S2 below summarizes the uncertainty associated with each experimental measurement.

Table S2. Uncertainties corresponding to experimental measurements.

Experimental Measurement	Uncertainty
Chiller water temperature difference ($\boldsymbol{T_{out} - T_{in}}$)	0.05K
Saturated vapor pressure (P_v)	1%
Saturated vapor temperature (T_v)	$T_{sat}(1.01(P_v))$-$T_{sat}(P_v)$
Chiller water mass flow rate ($\dot{\boldsymbol{m}}$)	2%
Sample surface area ($\boldsymbol{A}$)	2%
Gnielinski correlation heat transfer coefficient ($\boldsymbol{h_i}$)	10%

Modeling of Heat Transfer Coefficient

To model dropwise condensation, $h_{c,d}$ was obtained by incorporating the individual droplet heat transfer with droplet size distribution:[122]

$$\boldsymbol{h_{c,d} = \frac{q''}{\Delta T} = \frac{1}{\Delta T}\left(\int_{R^*}^{R_e} q(R)n(R)dR + \int_{R_e}^{\hat{R}} q(R)N(R)dR\right)} \quad \text{(S21)}$$

$$\boldsymbol{q(R) = \frac{\pi R^2\left(\Delta T - \frac{2T_{sat}\sigma}{Rh_{fg}\rho_w}\right)}{\frac{1}{2h_{int}(1-\cos\theta)} + \frac{R\theta}{4k_w\sin\theta} + \frac{1}{k_{HC}\sin^2\theta}\left(\frac{k_P\varphi}{\delta_{HC}k_P + hk_{HC}} + \frac{k_W(1-\varphi)}{\delta_{HC}k_w + hk_{HC}}\right)^{-1}}} \quad \text{(S22)}$$

where q'' is the steady state dropwise condensation heat transfer rate per unit area of the condensing surface, ΔT is the temperature difference between the saturated vapor and sample outer surface ($\Delta T = (T_{sat}(P) - T_s)$), R^* is the critical radius for heterogeneous nucleation ($R^* = r_c$),[14] R_c is the droplet coalescence radius, $q(R)$ is the individual droplet heat transfer (Equation S15), $n(R)$ is the non-interacting droplet size distribution,[122] $N(R)$ is the coalescence dominated droplet size distribution,[122,123] R is the droplet radius, σ is the condensate surface tension, h_{fg} is the latent heat of phase change, ρ_w is the condensate density (liquid water), θ is the droplet contact angle, h_{int} is the interfacial heat transfer coefficient,[238] k_w is the condensate thermal conductivity, k_{HC} is the hydrophobic coating thermal conductivity, φ is the structured surface solid fraction (equal to one for the flat surfaces considered here),

h is the structured surface height (equal to zero for flat surfaces), and δ_{HC} is the hydrophobic coating thickness (≈1 nm).[14] The first integral in Equation S14 represents the heat flux component from droplets smaller than the coalescence length scale ($R < R_e$), where direct growth by vapor accommodation at the liquid-vapor interface dominates and neighboring droplet coalescence is absent. The second integral represents the component of the heat flux from droplets growing mainly by coalescence with other droplets ($R > R_e$). These two components contribute to the total surface heat transfer per unit area (q''). For the graphene-coated surfaces, the model results were obtained using experimentally determined droplet departure radii $\hat{R}$ ($\hat{R}_{LPCVD}$ = 2.4 mm, $\hat{R}_{APCVD}$ = 2.8 mm) and contact angles, and assuming an effective nucleation density N from previous ESEM studies of condensation.[239]

To model filmwise condensation on the smooth Cu tubes, the Nusselt model was used:[237,238]

$$\boldsymbol{h_{c,f} = 0.729\left(\frac{g\rho_w(\rho_w - \rho_v)k_w{}^3 h'_{fg}}{\mu_w(2r)\Delta T}\right)^{1/4}} \quad \text{(S23)}$$

$$\boldsymbol{h'_{fg} = h_{fg} + 0.68c_{p,l}\Delta T} \quad \text{(S24)}$$

where g is the gravitational acceleration (g = 9.81 m/s^2), ρ_v is the water vapor density, μ_w is the condensate dynamic viscosity, h'_{fg} is the modified latent heat of vaporization accounting for the change in specific heat of the condensate, and $c_{p,l}$ is the condensate specific heat.[237,238]

An example of the dropwise and filmwise heat transfer coefficients as a function of condenser subcooling yielded from the above models is plotted in Figure S7 under typical experimental conditions. The dropwise condensation heat transfer coefficient decreases at low subcooling because the interfacial heat transfer coefficient becomes a major resistance to heat transfer.[21,47,130] Meanwhile, the filmwise condensation heat transfer coefficient increases at low subcooling as the film becomes thinner at low heat fluxes[15] (note that, although the heat transfer coefficient is increasing, the heat flux is decreasing). Furthermore, the Nusselt theory used for filmwise condensation does not consider the interfacial heat transfer coefficient, which would decrease the heat transfer coefficient at low subcooling in competition with the increase due to the thinner film. This results in the dropwise and filmwise heat transfer coefficients approaching each other as subcooling decreases.

In the present study, the condenser subcooling ranged from ≈1.5-6 K, with the experimentally measured heat transfer coefficients shown in this chapter obtained at condenser subcooling ranging from 3.5-5 K

while varying vapor pressure (the horizontal axis) and maintaining the supersaturation, $S = P_{vapor}/P_{sat}(T_{wall})$, constant over the range of data. The experimentally determined heat transfer coefficient enhancement of 4x for dropwise condensation on graphene-coated tubes compared to filmwise condensation is in excellent agreement with the model shown in Figure S7 in the 3.5-5 K subcooling range where the experimental measurements were taken. Note that, at higher subcooling over ≈10 K, the typically reported 5-7x heat transfer coefficient enhancement[21] for dropwise compared to filmwise condensation would be realized.

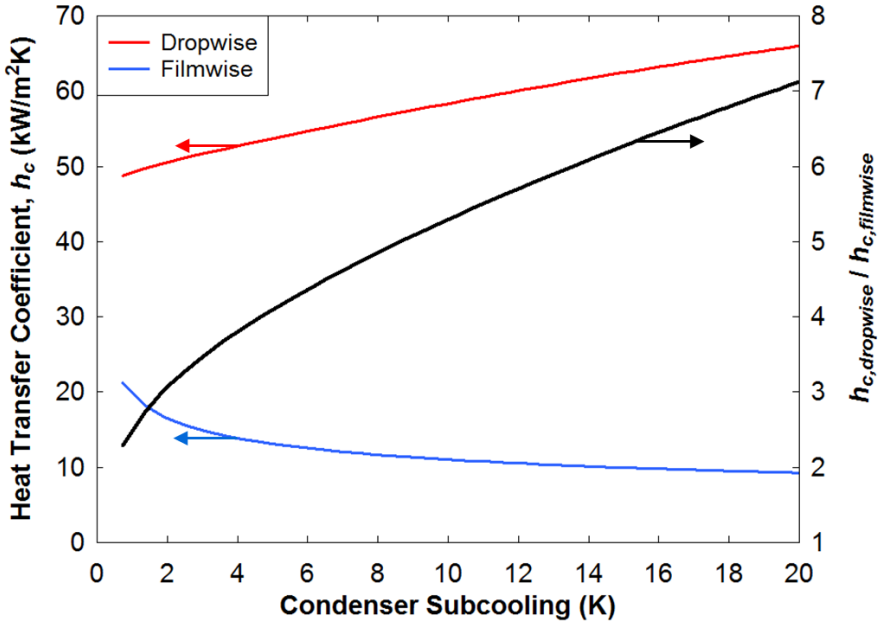

Figure S7. Plot of model results for filmwise and dropwise condensation heat transfer coefficient as a function of condenser subcooling, keeping the condenser temperature constant at 15.5℃ (P_{sat} = 1780 Pa) and varying the surrounding saturated water vapor temperature from 16 to 35.5℃ (P_{sat} = 1840 to 5860 Pa). The secondary (right) vertical axis is the ratio of dropwise to filmwise condensation heat transfer coefficients.

Robustness Characterization Setup and Operation

The robustness of the graphene coatings was characterized in a controlled positive-pressure continuous condensation chamber, shown in Figure S8. The robustness characterization setup is a thermosiphon with the samples located at the condenser section, where they are observed periodically to monitor degradation. A 1/4" thick borosilicate window was fit on a stainless steel chamber, and the 3/4"x3/4" square copper samples being tested are secured to the interior surface of the back wall of the chamber. The exterior of the back wall was in thermal contact with a Peltier cold stage with 100W cooling capacity.

A separate reservoir filled with degassed, deionized water was located 0.5 m below the chamber. Heaters on the exterior of the reservoir raised the water temperature to above 100 °C, and the resulting vapor then traveled through a supply line up to the chamber, where it condensed on the chamber walls and also escaped through a check valve rated for 0.1 psig due to the overpressure from boiling in the reservoir. The condensed vapor transported to the bottom of the chamber, where it collected until it flowed under the influence of gravity back to the reservoir.

To eliminate noncondensable gases (NCGs) from the system before operation, the water in the reservoir was boiled vigorously while the chamber was heated by the Peltier stage and also externally by a hot air gun to prevent condensation on the chamber walls and the subsequent trapping on NCGs in a diffusion boundary layer. This purge step was carried out until the system contains nearly pure saturated water/vapor. After the purge process, the system was constantly maintained at positive pressure to prevent NCGs from reentering. The system was overpressurized by boiling slightly more water than is condensed, resulting in water leaving the check valve and signifying that the system is at > 0.1 psig. Once the system had reached this steady operating condition, the Peltier stage was switched to cooling mode, where in the present study the samples were cooled to a surface temperature of 95±1 °C and exposed to a continuous supply of 100 °C steam, as determined by thermocouples mounted in the system. The durability of the graphene-coated samples is shown to be comparable to the highest-quality polymer CVD coatings.[48]

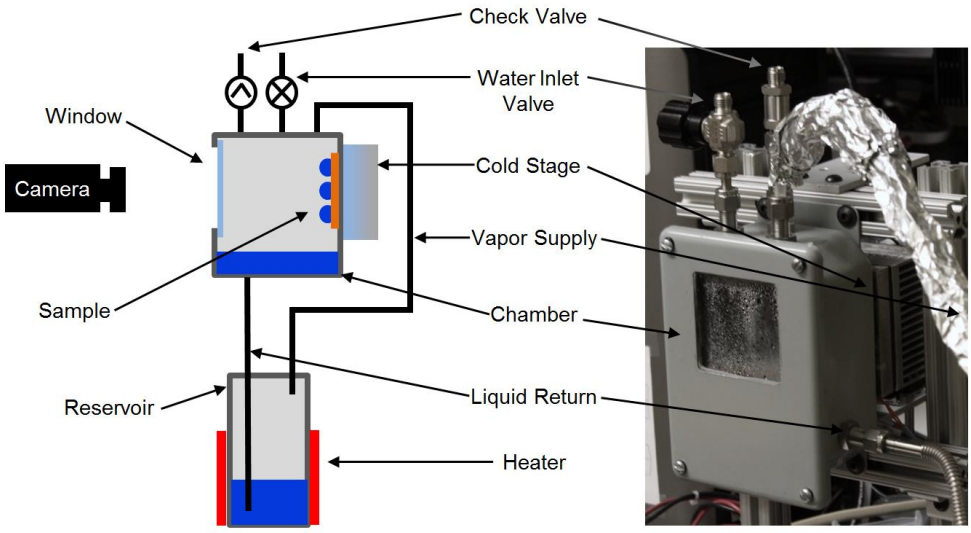

Figure S8. Schematic of experimental robustness characterization setup, which is comprised of a thermosiphon operating between a hot reservoir and a cold condenser section where the samples were imaged periodically to monitor degradation.

Comparison with Previous Work on Graphene Robustness

The LPCVD and APCVD graphene coated samples both sustained dropwise condensation for over two weeks with no signs of degradation when the experiments were discontinued. This result agrees with past work that demonstrates experimentally that destruction of a graphene coating does not occur by oxidation below 400℃[240] and that graphene prevents oxidation of copper surfaces and is an excellent passivation layer.[241] However, subsequent literature states that this passivation is only valid for short times (hours), after which the coatings can fail due to oxidation of copper at graphene grain boundaries.[242] These experiments were conducted at 185-250℃, above our condenser surface temperature of ≈95℃; accordingly, a thermally activated oxidation process would be expected to take longer for our lower-temperature test. Regardless, over two weeks, we did not observe oxidation or degradation in our experiments, which agrees with the studies which show that oxidation is mitigated.

Graphene Transfer to Transparent Substrate

The graphene was transferred to a transparent substrate by the electrochemical delamination transfer process.[243,244] This process removes the need for Cu etchant to detach the graphene from the Cu, which consequently avoids the large quantity of etchant waste from the relatively thick Cu sample on which the graphene was grown. After the graphene growth, poly(methyl methacrylate) (PMMA) (950 PMMA A9, Micro Chem, mixed with anisole (99%, Alfa Aesar) 1:1 by volume) was spun on one side of the graphene/copper substrate. After baking at ~75 ℃ for 5 minutes, the substrate was cathodically polarized at –5 V, and an aqueous solution of NaOH (10 mM) was employed as an electrolyte in the electrochemical process. Hydrogen bubbles emerged at the graphene/Cu interfaces due to the reduction of water and detached the graphene film from the Cu foil. The graphene/PMMA was then placed on top of the transparent substrate. The PMMA layer was removed by annealing the substrate at 500 ℃ in a hydrogen (700 sccm) and argon (400 sccm) mixture for two hours.

Graphene Coating Cost Estimate

The cost of the graphene coatings is estimated here for the lab-scale production procedure. The costs used are conservative; moving to industrial scale fabrication, process optimization, and using less conservative cost estimates is expected to reduce the price by several orders of magnitude. The gas prices at the lab scale are (for 300 ft^3 per cylinder, prices obtained from airgas.com on 12 February 2015):

Gas	Cylinder Price ($)	Volumetric Gas Price ($/$m^3$)
Argon (Ultra High Purity)	81.08	9.55
Hydrogen (Ultra High Purity)	140.24	16.52
Methane(Ultra High Purity)	323.11	38.06

Prescribing the gas consumption according to the CVD process detailed in the manuscript, and assuming that 10 tube condenser samples of the geometry used in the present study are being coated simultaneously for a total external surface area of 0.0174 m^2, the overall prices for gases for the CVD process are summarized as:

LPCVD			**APCVD**		
Flow phase 1 H_2	10	sccm	Flow phase 1 Ar	500	sccm
Time phase 1	30	min	Time phase 1	30	min
Flow phase 2 H_2	70	sccm	Flow phase 2 Ar	500	sccm
Flow phase 2 CH_4	4	sccm	Flow phase 2 CH_4	3	sccm
Time phase 2	30	min	Time phase 2	30	min
Flow phase 3 H_2	10	sccm	Flow phase 3 Ar	500	sccm
Time phase 3	120	min	Time phase 3	120	min
H2 total consumed	3600	cm^3	H2 total consumed	90000	cm^3
CH4 total consumed	120	cm^3	CH4 total consumed	90	cm^3
H2 total consumed	0.0036	m^3	H2 total consumed	0.09	m^3
CH4 total consumed	0.00012	m^3	CH4 total consumed	0.00009	m^3
Gas total price	0.064	$	Gas total price	0.863	$
Gas price per area	3.69	$/$m^2$	Gas price per area	49.66	$/$m^2$

Taking the power required to heat the furnace as the maximum furnace power of 800W for the 1-inch diameter tube furnace (Thermo Scientific Lindberg/Blue M Tube Furnace C2) over the operating period of 1.5hr including a 0.5-hour ramp period yields the cost of electricity:

Furnace power	0.8	kW
Heating time	1.5	hr
Energy consumed	1.2	kWh
Price of electrical energy	0.12	$/kWh
Total price of electricity	0.144	$
Electricity price per area	8.29	$/m^2

Therefore, summing the price per area of electricity and gas consumption, the lab-scale non-optimized costs for CVD graphene coatings are \$11.98/m^2 for LPCVD and \$57.95/m^2 for APCVD. This estimate is useful for performing a cost-benefit analysis based on capital cost and efficiency improvement.[245]

8.4 CH. 4 SUPPLEMENTARY INFORMATION

Results from Xiao et al. Compared to Filmwise Condensation from Nusselt's Model

Xiao et al. reported that *"the overall heat transfer coefficients on [dropwise condensation] surfaces in this work (h < 2–7 kW/m^{2}K) are much lower compared to pure vapor conditions [in previous work by Miljkovic et al.] (h<12–13 kW/m^{2}K)[135] due to the presence of NCGs acting as a diffusion barrier to the transport of water vapor towards the condensing surface."*[24] Therefore, the fact that the noncondensables (NCGs) would degrade heat transfer performance was recognized. Unfortunately, the data reported is the overall heat transfer coefficient including the tube wall and the chiller water flow, as opposed to the isolated condensation heat transfer coefficient. We can approximate the condensation heat transfer coefficient (including NCG effects) by assuming that the effective heat transfer coefficient of the non-condensing sections of the resistance network, h_{fixed}, namely, the tube wall and the chiller water flow, remains fixed between experiments (see the figure in the chapter for a schematic of the resistance network):

$$\boldsymbol{h_{fixed} = \left(\frac{1}{h_{overall}} - \frac{1}{h_{cond}}\right)^{-1} = \left(\frac{1}{12\ \mathrm{kW/m^2K}} - \frac{1}{60\ \mathrm{kW/m^2K}}\right)^{-1} = 15\ \mathrm{W/m^2K}} \quad \text{(S25)}$$

where $h_{overall}$ is taken from the earlier work by Miljkovic et al. using the same experimental setup to characterize dropwise condensation and h_{cond} is the heat transfer coefficient of dropwise condensation reported in that work.[135] Now we compare h_{fixed} with the range of overall heat transfer coefficients reported by Xiao et al., 2–7 kW/m^{2}K, and we see that the thermal resistance of the condensation with NCGs is the dominant resistance in the network in this scenario:

$$\boldsymbol{\frac{R_{cond}}{R_{overall}} = \frac{h_{overall}}{h_{cond}} = \frac{h_{overall}}{\left(\frac{1}{h_{overall}} - \frac{1}{h_{fixed}}\right)^{-1}} = 53\%\ to\ 87\%} \quad \text{(S26)}$$

Rearranging this equation, we can determine the h_{cond} including the effect of NCG for any given $h_{overall}$ reported in Figure 4 of Xiao et al. using Equation S27 here:

$$h_{cond} = \left(\frac{1}{h_{overall}} - \frac{1}{h_{fixed}} \right)^{-1} \tag{S27}$$

Next, assuming a constant wall temperature, T_w, across all experiments of 17 °C, determined from the supersaturation of 1.6 at the maximum vapor pressure plotted in Xiao et al.'s Figure 4, we can also determine the vapor temperature, T_v, at each vapor pressure for a saturated mixture, and from these two temperatures we know the subcooling. The subcooling and the condensation heat transfer coefficient can be combined to find the heat flux for each data point. Finally, plotting the heat flux versus the subcooling for each data point yields the result shown in Figure S9 below, where the heat transfer is comparable to that which would be expected from filmwise condensation.

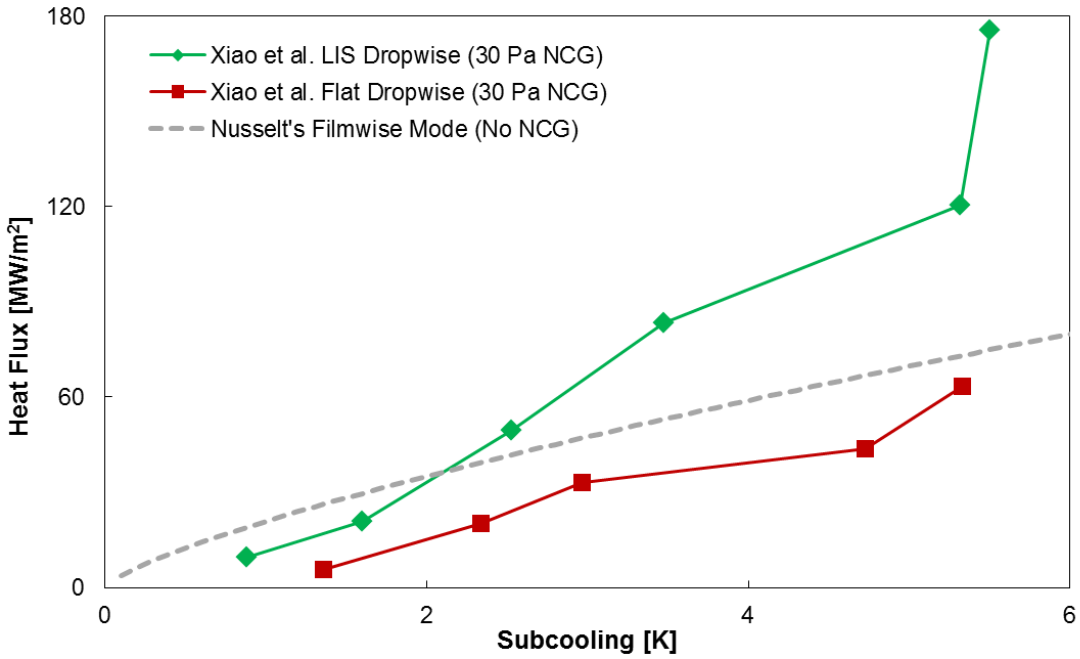

Figure S9. Adjusted and replotted data from Xiao et al. shows heat flux vs. condenser subcooling. The 30 Pa NCG in the system degrades the heat transfer performance of the dropwise condensation to approximately that of the expectation for filmwise condensation.

Droplet Departure Size Characterization

The average droplet departure size was calculated using imaging analysis performed on videos of condensation on the different surfaces with at least 20 departure events observed for each sample. The results are shown in Table S3.

Table S3. Average droplet departure diameters.

	Average Diameter (mm)	Standard Deviation (mm)
Water on Flat Hydrophobic Surface	2.92	0.42
Water on LIS	1.23	0.34
Toluene on LIS	2.12	0.23

Condensation Chamber Setup

The custom environmental chamber used for this work consists of a stainless steel frame with a door (sealed with a rubber gasket), two viewing windows, and apertures for various components. Resistive heater lines were wrapped around the exterior of the chamber walls to prevent condensation at the inside walls and then insulated on the exterior walls. The output power of the resistive heater lines was controlled by a voltage regulator. Two insulated stainless steel water flow lines (Swagelok) were fed into the chamber to supply cooling water to the chamber from a large capacity chiller.

A secondary stainless steel tube line was fed into the chamber that served as the flow line for the incoming water vapor supplied from a heated steel water reservoir. The vapor line was wrapped with a rope heater (60 W, Omega) and controlled by a power supply. The vapor reservoir was wrapped with another independently-controlled heater (120 W, Omega) and insulated to limit heat losses to the environment. The access tubes were welded to the vapor reservoir, each with independently-controlled valves. The first valve (Diaphragm Type, Swagelok), connecting the bottom of the reservoir to the ambient, was used to fill the reservoir with water. The second valve (BK-60, Swagelok), connecting the top of the reservoir to the inside of the chamber,

provided a path for vapor inflow. K-type thermocouples were located along the length of the water vapor reservoir to monitor temperature.

A bellows valve (Kurt J. Lesker) was attached to the chamber to serve as a leak port between the ambient and inside of the chamber. In order to monitor temperatures within the chamber, K-type thermocouple bundles were connected through the chamber apertures *via* a thermocouple feed through (Kurt J. Lesker). To provide electrical connections inside the chamber for LED lighting and electric field generation, insulated copper electrical wires were connected through the chamber apertures *via* an electrical feed through (Kurt J. Lesker). A pressure transducer (925 Micro Pirani, MKS) was attached to monitor pressure within the chamber. The thermocouple bundles and the pressure transducer were both electrically connected to an analog input source (RAQ DAQ, National Instruments), which was interfaced to a computer for data recording. A second bellows valve (Kurt J. Lesker) was integrated onto the chamber for the vacuum pump, which brought down the chamber to vacuum conditions prior to vapor filling. A liquid nitrogen cold trap was incorporated along the line from the chamber to the vacuum which served to remove any moisture from the pump-down process and ultimately assist in yielding higher quality vacuum conditions. A tertiary bellows valve (Kurt J. Lesker) was integrated on a T fitting between the vacuum pump and liquid nitrogen reservoir to connect the vacuum line to the ambient to release the vacuum line to ambient conditions once pump down was achieved. In order to visually capture data, a digital SLR camera (Canon EOS 50D) was placed in line with the 5” viewing windows on the chamber.

The setup used to run experiments inside the chamber is shown above. Stainless steel bellows tube lines (1/4”, Swagelok) were connected to the external water flow lines. T-connection adapters (Swagelok) with bore through Ultra-Torr fittings (Swagelok) were used to adapt K-type thermocouple probes (Omega) at the water inlet and outlet.

Condensation Procedure

For each experimental trial, a set of strict procedures was followed to ensure consistency throughout the experiments. The first step of the process was to turn on the voltage regulator to heat up the environmental chamber walls, which prevented condensation on the chamber walls.

Simultaneously, the vapor reservoir was filled with approximately 2 liters of either DI water or toluene. After opening the vapor inflow valve and closing the vapor release valve, the rope heater around the vapor reservoir was turned on with the heater controller set to maximum output (120 W). Then the rope heater connected to the vapor inflow valve was turned on. The temperature of the reservoir was monitored with the installed thermocouples; the temperature at the top of the reservoir was higher than that of the middle/bottom of the reservoir due to the water thermal-mass present at the middle/bottom section. Hence, we ensured that the regions of the reservoir of higher thermal capacity were brought to a sufficiently high temperature for boiling. During the boiling process, aluminum foil was placed on the bottom surface of the inner chamber to collect any of the water leaving the vapor inflow line. Once boiling was achieved and the internal thermocouple on the reservoir was 5˚C above the boiling point for at least 10 minutes, the vapor inflow valve was closed. The excess fluid that spilled inside the chamber during de-gassing of the reservoir was removed.

In order to install the samples onto the rig, the Swagelok female adapters at the ends of the tube samples were connected to the 90 degree male elbow connecters on the rig. Before installing the entire sample setup in the chamber, all adapters/connecters were tightened to ensure that there were no leaks that could affect vacuum performance. The setup was then placed on top of the steel supports and the bellows tubes (for the water inflow/outflow) were connected to the water lines.

The next step was to begin the vacuum pump-down procedure. Initially, the liquid nitrogen cold trap was filled to about half capacity. The ambient exposed valves connecting the chamber and the vacuum pump were both closed and the valve connected to the liquid nitrogen cold trap was opened. The vacuum pump was then turned on, initiating the pump-down process. The pressure inside the chamber was monitored during the pump-down process. This process took approximately one hour in order to achieve the target vacuum conditions ($0.5\ \text{Pa} < P < 1\ \text{Pa}$). The experimental operating pressure of non-condensable was set to be a maximum of 0.25% of the operating pressure. Non-condensable gas content of above 0.5% (pressure) has been shown to significantly degrade performance during dropwise condensation.[21,174] In our experiments, extreme care was taken to properly de-gas the vacuum chamber and water vapor reservoir prior

to experimental testing. In addition, the chamber leak rate was characterized prior to each run in order to estimate the maximum time available for acquiring high fidelity data with non-condensable content of less than 0.25%.

The setup of the water flow-loop is described as follows: the water pump reservoir was filled and turned on to a flow rate of 5 L/min. The flow rate was monitored with the flow meter integrated in the inflow water line. In order to bring the chilled water into the flow loop and to the tube sample, the external chilled water lines were opened.

Prior to beginning experiments, the camera was turned on for visual imaging of the sample during condensation. Afterwards, the rope heater around the water reservoir was turned off and the vapor inflow valve was slowly turned open until the operating pressure was reached. Steady state conditions were typically reached after 2 minutes of full operation.

Heat Transfer Coefficient and Error Propagation

See error analysis for Chapter 3.

Modeling of Heat Transfer Coefficient

To model dropwise condensation, $h_{c,d}$ was obtained by incorporating the individual droplet heat transfer with droplet size distribution:[122]

$$\boldsymbol{h_{c,d} = \frac{q''}{\Delta T} = \frac{1}{\Delta T}\left(\int_{R^*}^{R_e} q(R)n(R)dR + \int_{R_e}^{\hat{R}} q(R)N(R)dR\right)} \tag{S28}$$

$$\boldsymbol{q(R) = \frac{\pi R^2\left(\Delta T - \frac{2T_{sat}\sigma}{Rh_{fg}\rho_w}\right)}{\frac{1}{2h_{int}(1-\cos\theta)} + \frac{R\theta}{4k_w\sin\theta} + \frac{1}{k_{HC}\sin^2\theta}\left(\frac{k_P\varphi}{\delta_{HC}k_P + hk_{HC}} + \frac{k_W(1-\varphi)}{\delta_{HC}k_w + hk_{HC}}\right)^{-1}}} \tag{S29}$$

where *q"* is the steady state dropwise condensation heat transfer rate per unit area of the condensing surface, ΔT is the temperature difference between the saturated vapor and sample

outer surface ($\Delta T = (T_{sat}(P) - T_s)$), R^* is the critical radius for heterogeneous nucleation ($R^* = r_c$),[14] R_c is the droplet coalescence radius, $q(R)$ is the individual droplet heat transfer (Equation S17), $n(R)$ is the non-interacting droplet size distribution,[122] $N(R)$ is the coalescence dominated droplet size distribution,[122,123] R is the droplet radius, σ is the condensate surface tension, h_{fg} is the latent heat of phase change, ρ_w is the condensate density (liquid water), θ is the droplet contact angle, h_{int} is the interfacial heat transfer coefficient,[238] k_w is the condensate thermal conductivity, k_{HC} is the hydrophobic coating thermal conductivity, φ is the structured surface solid fraction (equal to one for the flat surfaces considered here), h is the structured surface height (equal to zero for flat surfaces), and δ_{HC} is the hydrophobic coating thickness (≈1 nm).[14] The first integral in Equation S14 represents the heat flux component from droplets smaller than the coalescence length scale ($R < R_e$), where direct growth by vapor accommodation at the liquid-vapor interface dominates and neighboring droplet coalescence is absent. The second integral represents the component of the heat flux from droplets growing mainly by coalescence with other droplets ($R > R_e$). These two components contribute to the total surface heat transfer per unit area (q''). The model results were obtained using experimentally determined droplet departure radii $\hat{R}$ (see Table S1, above) and contact angles.

Note that the equation above is modified on the lubricant infused surface because lubricant is between the structures on the surface. The appropriate equation for the LIS is:

$$\boldsymbol{q(R) = \frac{\pi R^2 \left(\Delta T - \frac{2T_{sat}\sigma}{Rh_{fg}\rho_w}\right)}{\frac{1}{2h_{int}(1-\cos\theta)} + \frac{R\theta}{4k_w \sin\theta} + \frac{1}{k_{HC}\sin^2\theta}\left(\frac{k_P\varphi}{\delta_{HC}k_P + hk_{HC}} + \frac{k_W(1-\varphi)}{\delta_{HC}k_l + hk_{HC}}\right)^{-1}}} \quad \text{(S30)}$$

where the k_w has been changed to k_l in the right-most section of the denominator. Another important modification to the model for LIS is the alteration of the droplet size distribution for large drops, N(R). In previous work on dropwise condensation on flat surfaces, and for the model in the present work used for dropwise condensation on a flat surface, the droplet size distribution has been taken as:

$$N(R) = \frac{1}{3\pi R^2 \widehat{R}} \left(\frac{R}{\widehat{R}}\right)^{-2/3} \quad \text{(S31)}$$

However, recent work by Weisensee et al.[176] has suggested that LIS follow a large droplet size distribution of:

$$N(R) = \frac{1}{3\pi R^3} \quad \text{(S32)}$$

based on experimental observation. Therefore, N(R) presented in Equation S20 above is used when modeling LIS. Finally, the droplet radius at which coalescence-based growth begins to dominate was found to vary between samples. Values of 1 μm, 4 μm, and 8 μm were used for water condensation on the flat hydrophobic surface, water condensation on the LIS, and toluene condensation on the LIS, respectively; all of these values lie in the range of typically observed droplet radii for coalescence dominated growth of 0.5–10 μm[176] and may have implications in the nucleation behaviour of droplets on LIS.

To model filmwise condensation on the smooth Cu tubes, the Nusselt model was used:[237,238]

$$h_{c,f} = 0.729 \left(\frac{g\rho_w(\rho_w - \rho_v){k_w}^3 {h'}_{fg}}{\mu_w(2r)\Delta T}\right)^{1/4} \quad \text{(S33)}$$

$$h'_{fg} = h_{fg} + 0.68 c_{p,l}\Delta T \quad \text{(S34)}$$

where g is the gravitational acceleration (g = 9.81 m/s^2), ρ_v is the water vapor density, μ_w is the condensate dynamic viscosity, h'_{fg} is the modified latent heat of vaporization accounting for the change in specific heat of the condensate, and $c_{p,l}$ is the condensate specific heat.[237,238]

An example of the dropwise and filmwise heat transfer coefficients as a function of condenser subcooling yielded from the above models is plotted in Figure S7 under typical experimental

conditions for condensation of water. The dropwise condensation heat transfer coefficient decreases at low subcooling because the interfacial heat transfer coefficient becomes a major resistance to heat transfer.[21,47,130] Meanwhile, the filmwise condensation heat transfer coefficient increases at low subcooling as the film becomes thinner at low heat fluxes[15] (note that, although the heat transfer coefficient is increasing, the heat flux is decreasing). Furthermore, the Nusselt theory used for filmwise condensation does not consider the interfacial heat transfer coefficient, which would decrease the heat transfer coefficient at low subcooling in competition with the increase due to the thinner film. This results in the dropwise and filmwise heat transfer coefficients approaching each other as subcooling decreases.

In the present study, the condenser subcooling during dropwise condensation of water ranged from ≈1.5-6 K. The experimentally determined heat transfer coefficient enhancement of 3-4x for dropwise condensation of water on flat hydrophobic and LIS-coated tubes compared to filmwise condensation is in excellent agreement with the model shown in Figure S7 in the Chapter 3 supplementary information in the 2-5 K subcooling range where the experimental measurements were taken. Note that, at higher subcooling over ≈10 K, the typically reported heat transfer coefficient enhancement of up to one order of magnitude[21] for dropwise compared to filmwise condensation would be realized.

8.5 CH. 5 SUPPLEMENTARY INFORMATION

Compilation of some vOCG surface energy components from literature:

Fluid	γ (mN/m)	γ^{LW} (mN/m)	γ^{AB} (mN/m)	γ^{+} (mN/m)	γ^{-} (mN/m)
Benzene	28.9	28.9	0	0	0.96
Chlorobenzene	33.6	32.1	1.5	0.9	0.61
Chloroform (Trichloromethane)	27.2	27.2	0	1.5	0
Cyclohexane	25.24	25.24	0	0	0
cis-Decahydrohaphthalene	32.2	32.2	0	0	0
Decane	23.83	23.83	0	0	0
Diethyl Ether (ethoxyethane)	17	17	0	-	-
Diiodomethane	50.8	50.8	0	0	0
Diiodomethane	50.8	49	1.8	0.01	0
Diiodomethane	50.8	44.1	6.7	0.01	0
Diiodomethane	50.8	48.5	2.3	0.01	
Dimethylsulfoxide	44	36	8	0.5	32
Dodecane	25.35	25.35	0	0	0
Eicosane	28.87	28.87	0	0	0
Ethanol	22.4	18.8	2.6	0.019	68
Ethyl acetate (ethyl ethanoate)	23.9	23.9	0	0	6.2
Ethylene Glycol	48	29	19	1.92	47
Ethylene Glycol	48	29	19	3	30.1
Ethylene Glycol	48.8	32.8	16	3	30.1
Formamide	58	39	19	0.5	32
Formamide	58	39	19	2.28	39.6
Formamide	58.2	36	22.2	2.29	39.6
Formamide	57.9	34.3	23.5	2.28	39.6
Formamide	58.2	39.5	18.7	2.28	39.6
Glycerol	64	34	30	3.92	57.4
Glycerol	63.4	40.6	22.8	3.92	57.4
Glycerol	63.4	37	26.4	3.92	57.4
Heptane	20.14	20.14	0	0	0
Hexadecane	27.47	27.47	0	0	0
Hexane	18.4	18.4	0	0	0
Methanol	22.5	18.2	4.3	0.06	77
Methyl-ethyl-ketone	24.6	24.6	0	0	24
Nitrobenzene	43.9	41.3	2.6	0.26	6.6
Nonadecane	28.59	28.59	0	0	0

Nonane	22.85	22.85	0	0	0
Octane	21.62	21.62	0	0	0
Perfluoroheptane	12.8	12.8	0	0	0
Pentadecane	27.07	27.07	0	0	0
Pentane	16.05	16.05	0	0	0
Silicone Oil	18.8	18.8	0	0	0
Tetradecane	26.56	26.56	0	0	0
Tetrahydrofuran	27.4	27.4	0	0	15
Tricresyl phosphate	40.9	39.8	1.1		
Tricresyl phosphate	40.9	39.7	1.2		
Tricresyl phosphate	40.9	39.2	1.7		
Tridecane	25.99	25.99	0	0	0
Toluene	28.5	28.5	0	0	0.72
Undecane	24.66	24.66	0	0	0
Water	72.8	21.8	51	25.5	25.5
Water	72.8	22.6	50.2	25.5	25.5
Water	72.8	22.1	50.7	25.5	25.5
o-Xylene	30.1	30.1	0	0	0.58
α-Bromonaphthalene	44.4	44.4	0	0	0
2-Ethoxyethanol	28.6	23.6	5		
Polyethylene oxide, PEO 6000	43	43	0	0	64
Dextran 10000	61.2	47.4	13.8	1	47.4
Fluorocarbon polymer, FC 721	9.41	9.15	0.24	0.16	0.76
Polydimethylsiloxane, PDMS	23.1	22.9	0.12	0	3.05
Poly(methyl methacrylate), PMMA	39-43	39-43	0	0	9.5-22.4
Poly(methyl methacrylate), PMMA	48.9	46.5	2.4	0.08	18.1
Poly(methyl methacrylate), PMMA	46.4	44.4	1.92	0.03	27.9
Polyvinyl acetate, PVAc	44.5	42.6	1.9	0.041	22.3
Polyvinyl chloride, PVC	43.7	43	0.7	0.04	3.5
Polyvinyl chloride, PVC	43.1	40.2	2.9	0.42	5.1
Polystyrene, PS	42	42	0	0	1.1
PS (based on advancing CA)	44.9	44.9	0	0	1.33
PS (based on receding CA)	49.9	49.9	0	0	5.14
Polyethylene, PE (based on advancing CA)	33	33	0	0	0.1
PE (based on receding CA)	57.9-62.5	42	15.9-20.5	2.1	30-50
Polyethylene glycol, PEG-silane-modified	47.9	45.3	2.59	0.04	39.92
Polyamide-imide, PAI	52.6	42.8	9.8	1.04	23.15
Polyhydroxyethylmethacrylate	50.6	40.2	10.4	2.07	13.1

P(HEMA80/EMA20)	48.2	40.7	7.5	0.63	22.7
P(HEMA40/EMA60)	39.8	39.4	0.4	0.02	16.4
Polypyrrole, PPyTS	47	41	6	0.81	10.9
PPyCl	43.5	36.6	6.9	0.43	28.3
PPyDS	41.7	34.8	6.9	1.35	8.85
poly(3-octylthiophene), POT undoped		22.5			0.5
POT-AuCl-4		23.4-25			0.7-4.7
Polystyrene, PS	41.9	41.9	0.22	0.08	0.15
PS latices (Anionic) (advancing)	41.4	41.4	0	0	13.13
PS latices (Anionic) (receding)	57.6	50.8	6.8	1.19	9.73
PS latices (Cationic) (using water/ethylene glycol)		39.4-41.9		0-0.4	0.3-7
PS latices (Cationic) (using water/formamide)		39.4-41.9		0-0.1	1.8-8.2
Polypropylene, PP	32.2	30.1	2.1	0.3	3.8
PP	25.7	25.7	0	0	0
PP	29.7	29.7	0	0	1.4
PP-O2 plasma	43.1	36.7	6.4	0.5	22
PP-N2 plasma	53.3	41.9	11.4	1	30.9
PP-NH3 plasma	42.6	34.9	7.7	0.7	21.4
Fluorinated ethylene-propylene (FEP)	15.71	15.42	0.34	0.01	0.72
FEP	18.3	18.3	0	0	0
Poly(tetrafluoroethylene), PTFE	19.6	19.6	0	0	0
Polyisobutylene, PIS	25	25	0	0	0
Polyaurinlactam, PA 12	41.9	37.5	4.4	1	4.9
nylon (PA) 66	42.8	38.6	4.2	0.4	11.3
nylon 66	37.7	36.4	1.3	0.02	21.6
Polyvinyl pyrrolidone, PVPY	43.4	43.4	0	0	29.9
Polyvinyl fluoride, PVF	43.6	40.4	3.2	0.16	12.9
Polypropylene/EPDM, flame treated	43.7	25.9	17.8	2.6	30.3
Polyoxytretramethylene glycol), MW 2000	44	41.4	2.6	0.06	27.6
Polyoxyethylene, POE, PEG-6000	43	43	0	0	64
Polyethylene terephthalate	43.84	43.48	0.36	0.003	7.17
ethylene glycol-*co*-propylene glycol, MW 2000	47.5	42	5.5	0.13	58.8
ethylene glycol-*co*-propylene glycol, MW 1000	47.9	40.9	7	0.22	55.6
Oriented polypropylene, OPP (advancing)	32.6	32.6	0	0	0
OPP (receding)	39.2	37	2.2	1.3	0.9

OPP-air Corona-treated (advancing)	55.8	42	13.9	1.9	25.2
OPP-air Corona-treated (receding)	64.7	46.2	18.5	2	25.2
Trimethoxy(octadecyl)silane, OTS-silane-modified	23.5	23.3	0.19	0.01	1.1
Zoltek carbon fibers, Unsized	41.3	41.3	0	0	32.4
Zoltek carbon fibers, Ultem sized	40.2	38.6	1.6	0.03	20.5
Zoltek carbon fibers, PU sized	35.8	33.2	2.6	0.11	15.3
Chromium	59.6	45.8	13.8	0.86	55.5
Aluminum	57.4	46.7	10.7	0.5	57.5
Silicon wafer	61.9	38.6	23.3	4	33.98
Glass	59.3	42.03	17.8	1.97	40.22
Glass, H2SO4/HNO3	64.5	42.03	22.47	2.82	44.76
Glass, C18	26.8	25.7	1.12	0.24	1.32
Glass, APS-treated	45	39.2	5.76	0.084	98.62
HAS, dry, pH4.8	45	44	0.1	0.03	76
HAS, dry, pH7	41.4	41	0.4	0.002	20
HAS, hydrated, pH7	62.5	26.8	35.7	6.3	50.6
HIg-G, hydrated, pH7	51.3	34	17.3	1.5	49.6
HIg-A, hydrated, pH7	26.8	26.8	0	0	93
Bovine fibrinogen, dry	40.3	40.3	0	0	53.2
Human fibrinogen, dry	40.6	40.6	0	0	54.9
HLDLP, dry	41.1	35.5	5.66	0.26	30.8
Candida abicans (yeast) cultured at 30C	42.5	38.1	4.4	2.9	1.7
Candida abicans (yeast) cultured at 37C	47.7	37.3	10.4	0.6	43.7
Streptococcus gordonii (bacteria) cultured at 37C	38.9	35.8	3.1	4.2	0.6
Streptococcus oralis 34	57	35	22	2.7	45
Streptococcus oralis J22	48.7	38	10.68	0.5	57
Actinomyces naeslundii 5951	44	38	6	0.5	18
Actinomyces naeslundii 5519	40	37	2.97	0.1	22
Pressure-sensitive adhesive, PSA	16.7	12.6	4.1	0.42	9.9
Cellulose acetate	40.2	35	5.2	0.3	22.7
Cellulose nitrate	45	45	0	0	16
Agarose	44.1	41	3.1	0.1	24
Gelatin	38	38	0	0	19
Paraffin	25.5	25.5	0	0	0

Experimental Determination of vOCG Surface Energy Components

The vOCG surface energy components for undocumented fluids are determined by plane fitting experimental data points determined from at least three different test fluids. Equation S1 shows the form of the plane, where the left-hand-side is the z-value and the right hand side contains two slope terms and the intercept. The subscript "u" indicates the fluid with unknown vOCG components which must be solved for, and the subscript "i" represents the i-th test fluid for which the vOCG terms are known, and the quantities γ_u and γ_{ui} are measured experimentally.

$$\frac{(\boldsymbol{\gamma_u} + \boldsymbol{\gamma_i}) - \boldsymbol{\gamma_{ui}}}{\sqrt{\boldsymbol{\gamma_i^{LW}}}} = \sqrt{\boldsymbol{\gamma_u^+}}\sqrt{\frac{\boldsymbol{\gamma_i^-}}{\boldsymbol{\gamma_i^{LW}}}} + \sqrt{\boldsymbol{\gamma_u^-}}\sqrt{\frac{\boldsymbol{\gamma_i^+}}{\boldsymbol{\gamma_i^{LW}}}} + \mathbf{2}\sqrt{\boldsymbol{\gamma_u^{LW}}} \tag{S35}$$

Quotes from literature about LIS which show "state-of-the-art" design guidelines

With regard to the choice of solids or coatings applied to solids, Anand et al. assert that "[LIS] consist of nano/micro textured **low surface energy surfaces** impregnated with a liquid … immiscible with the liquid … to be repelled."[177]

With regard to choosing a solid surface for a condenser surface, Rykaczewski et al. state that "The most basic condenser surface must have a **critical surface energy appreciably lower than that of the condensate** to result in a finite wetting angle."[163]

With regard to the choice of a suitable solid and lubricant to promote wetting of the solid by the lubricant, the Aizenberg group states in a patent application that a "[LIS] can be designed based on the surface energy matching between a lubricating fluid and a solid."[215]

Impact of Surface Geometry

The surface geometric factor R is determined by the roughness, r, which represents the actual solid surface area divided by the projected area, and the solid fraction, φ, which represents the fraction of the solid which contacts the base of the droplet. A higher value of R amplifies the interaction between the solid and either the liquid phases compared to the liquid phases with

each other or with the surrounding vapor. For instance, increasing *R* can satisfy criterion (III) for a given lubricant which does not spontaneously spread over a flat solid surface.

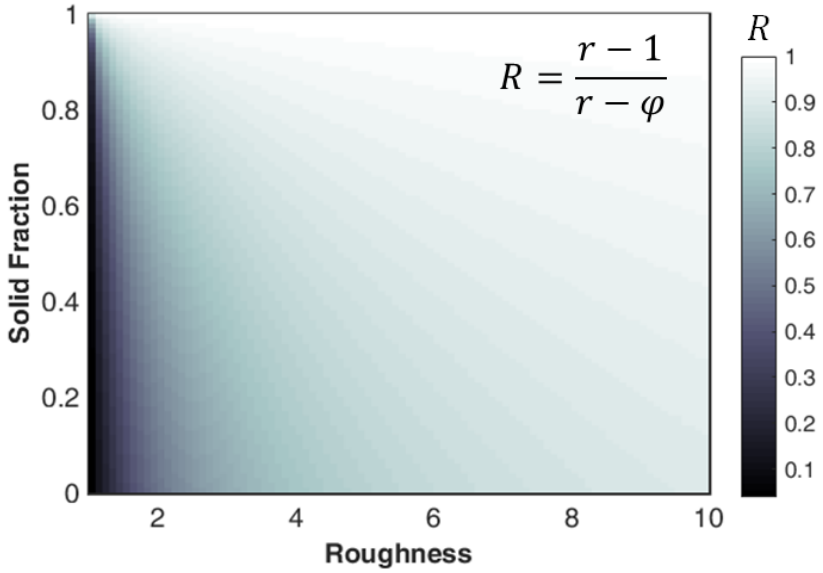

Figure S10. Plot of the geometric factor *R*. Values for *R* range from 0, corresponding to a flat surface, to 1, corresponding to a very rough surface.

Effect of Tightening the Miscibility Constraint

The miscibility criterion (V) in the manuscript can be more generally written as:

$$\boldsymbol{\gamma_{co} > \gamma_m} \tag{S36}$$

where γ_m is a miscibility cutoff value. All predictions in this manuscript use a cutoff value of γ_m = 0 mN/m unless otherwise indicated. The effect of altering the miscibility cutoff is explored here, with the result displayed in Figure S11.

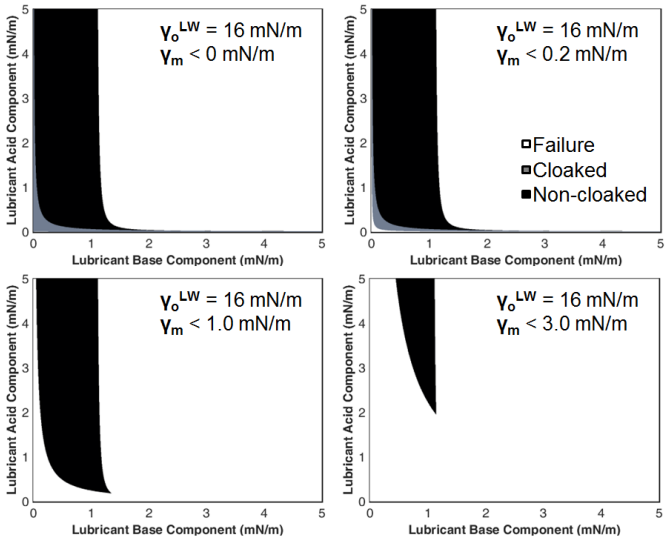

Figure S11. Result of changing the miscibility cutoff, γ_m. A higher miscibility cutoff results in a more conservative solution (i.e., more stringent requirement to be consider immiscible) which makes the solution domain smaller. Conversely, setting γ_m to $-\infty$ is equivalent to removing criterion (V) from the model.

The optimal miscibility cutoff was calculated from a dataset comprised of 120 fluid-fluid interactions with known miscibility (binary values: either miscible or immiscible). Since only 20% of the cases in the dataset were between immiscible fluids, a successful prediction in these cases was weighted 4x higher than a successful prediction for two miscible fluids. The vOCG miscibility prediction was then performed for all if the fluid pairs in the dataset and the prediction accuracy was scored, bounded by 50% accuracy at a cutoff of $-\infty$ when every prediction is immiscible and 50% accuracy at a cutoff of $+\infty$ when every prediction is miscible. The scores between these bounds are plotted in Figure S12. The optimal cutoff for miscibility to be used in criterion (V) was found to be 3.5 mN/m based on this scoring, as it resulted in the highest likelihood of predicting either miscibility or immiscibility correctly. This cutoff will give a more conservative prediction of whether a proposed LIS will succeed or fail. More detailed machine learning techniques may be useful in future work.[246]

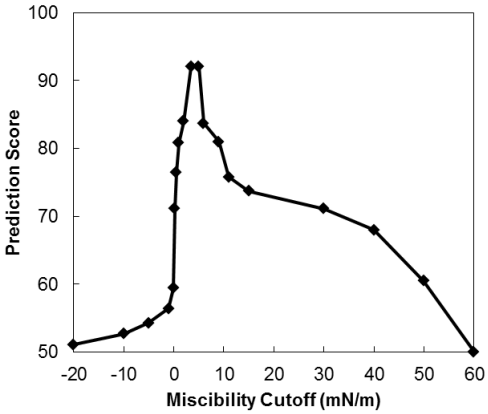

Figure S12. Weighted miscibility prediction score versus miscibility cutoff value. The optimal value for accurate miscibility prediction is 3.5 mN/m, which could be used in criterion (V) instead of 0 mN/m for a more conservative prediction of whether a LIS surface will succeed.

Choice of Solid Material for Polar Impinging Fluids

The parametric sweep in the manuscript demonstrated the suitability of polar surfaces with significant Lewis acid-base components of vOCG surface energy to repulsion of nonpolar impinging fluids. However, if the impinging fluid is polar, a nonpolar solid surface will likely generate a larger solution domain as shown in Figure S13 with water as the impinging fluid.

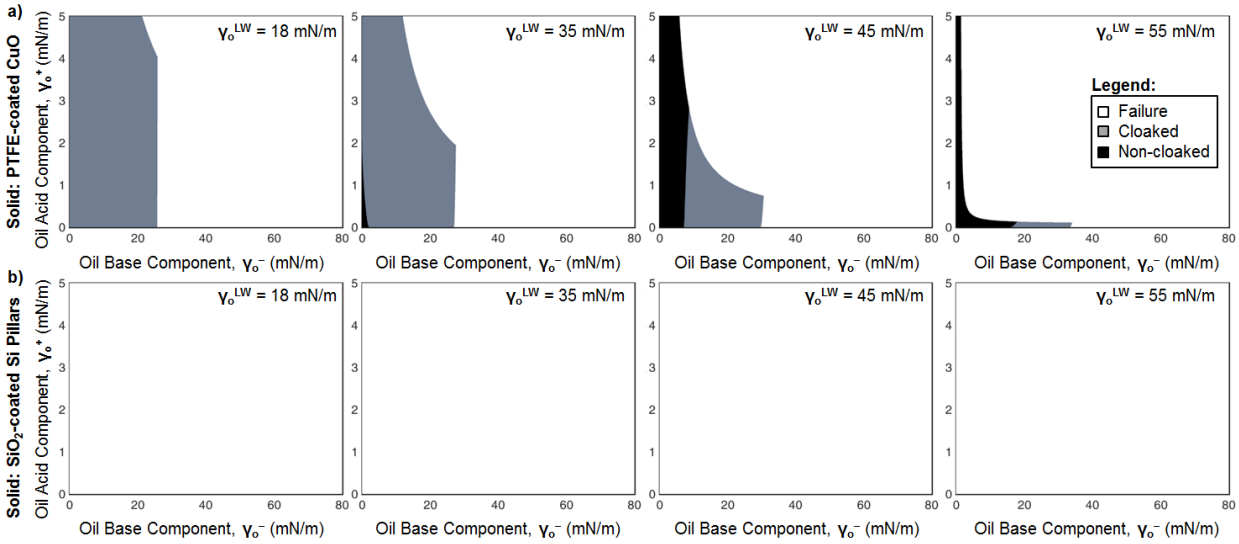

Figure S13. Design of LIS to repel a polar fluid – in this case, water. The PTFE-coated solid surface allows a reasonable solution domain of fluid choices. The polar SiO2 pillar array surface does not result in any solutions for practical lubricating fluids (solutions only exist for $\gamma^+ > 20$ mN/m, which is outside of the realm of available choices as shown in Table S1).

Results from Condensation Experiments

Images of several successful condensation tests performed with various fluids on a LIS are shown in Figure S14. These results were used in Table 1 for the model validation.

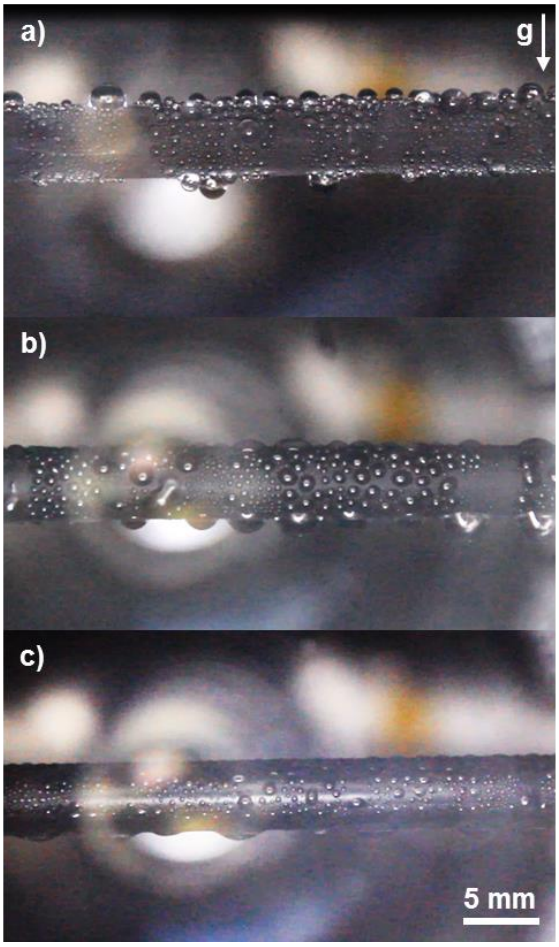

Figure S14. Results from condensation of impinging fluid on LIS. Three different impinging fluids, (a) water, (b) toluene, and (c) pentane, were condensed onto a LIS comprised of Krytox GPL 101 infused into TFTS-coated CuO nanoblades. In all three cases, formation of discrete droplets of condensate was observed.